COMPUTATIONAL MODELING OF SELF-ASSEMBLY IN DEFORMABLE BODIES

A THESIS SUBMITTED TO
THE GRADUATE SCHOOL OF NATURAL AND APPLIED SCIENCES
OF
MIDDLE EAST TECHNICAL UNIVERSITY

BY

BİLGİN KOÇAK

IN PARTIAL FULFILLMENT OF THE REQUIREMENTS
FOR
THE DEGREE OF MASTER OF SCIENCE
IN
CIVIL ENGINEERING

SEPTEMBER 2021

Approval of the thesis:

COMPUTATIONAL MODELING OF SELF-ASSEMBLY IN DEFORMABLE BODIES

submitted by **BİLGİN KOÇAK** in partial fulfillment of the requirements for the degree of **Master of Science in Civil Engineering Department, Middle East Technical University** by,

Prof. Dr. Halil Kalıpçılar
Dean, Graduate School of **Natural and Applied Sciences** _____

Prof. Dr. Ahmet Türer
Head of Department, **Civil Engineering** _____

Assoc. Prof. Dr. Serdar Göktepe
Supervisor, **Civil Engineering** _____

Examining Committee Members:

Prof. Dr. Kağan Tuncay
Civil Engineering, METU _____

Assoc. Prof. Dr. Serdar Göktepe
Civil Engineering, METU _____

Prof. Dr. Afşin Sarıtaş
Civil Engineering, METU _____

Prof. Dr. Hakan Argeşo
Aerospace Engineering, Atılım University _____

Assoc. Prof. Dr. Ercan Gürses
Aerospace Engineering, METU _____

Date: 09.09.2021

I hereby declare that all information in this document has been obtained and presented in accordance with academic rules and ethical conduct. I also declare that, as required by these rules and conduct, I have fully cited and referenced all material and results that are not original to this work.

Name, Surname: Bilgin Koçak

Signature :

ABSTRACT

COMPUTATIONAL MODELING OF SELF-ASSEMBLY IN DEFORMABLE BODIES

Koçak, Bilgin
M.S., Department of Civil Engineering
Supervisor: Assoc. Prof. Dr. Serdar Göktepe

September 2021, 113 pages

Self-assembly is a process in which an irregular system transforms into a regular pattern or an organized structure through local interactions between the components of the material without any external influence. Therefore, self-assembly has great potential in the synthesis and manufacture of new materials. Although the main focus in the literature is mostly on self-assembly at the molecular level, there are many exciting applications of the self-assembling processes at larger scales. Space and time-varying patterns are described by various classes of spatio-temporal partial differential equations. The reaction-transport problems constitute one of these classes that employs the Cahn-Hilliard-type equation, also originally a fourth-order transport equation, for patterning. This study is concerned with the effect of mechanical stresses on the generated pattern in a self-assembling process. For mechanics, both finite elasticity and viscoelasticity are considered. To this end, the Cahn-Hilliard equations are solved together with the conservation equation of the linear momentum. The finite element method is used to solve the coupled partial differential equations. It is anticipated that the coupling with mechanics will open up possibilities for the design of new materials and lead to novel experiments for various kinds of self-assembly. Numerous

representative numerical examples are presented to illustrate the characteristics and physics of the coupled and decoupled phase separation and self-assembly problems.

Keywords: Self-assembly, Cahn-Hilliard equation, (Visco-)elasticity, Finite element method, Phase separation

ÖZ

ŞEKİL DEĞİŞTİREBİLEN CİSİMLERDE KENDİLİĞİNDEN YAPILANMANIN HESAPLAMALI MODELLENMESİ

Koçak, Bilgin
Yüksek Lisans, İnşaat Mühendisliği Bölümü
Tez Yöneticisi: Doç. Dr. Serdar Göktepe

Eylül 2021 , 113 sayfa

Kendiliğinden yapılanma, düzensiz bir sistemin, herhangi bir dış etki olmaksızın, malzemenin bileşenleri arasındaki yerel etkileşimler yoluyla düzenli bir örüntü veya organize bir yapıya dönüştüğü bir süreçtir. Bu nedenle kendiliğinden yapılanma, yeni malzemelerin sentezinde ve üretiminde büyük bir potansiyele sahiptir. Literatürdeki çalışmaların çoğu moleküler düzeydeki kendiliğinden yapılanma üzerine odaklansa da, kendiliğinden yapılanma işlemlerinin daha büyük ölçeklerde birçok heyecan verici uygulaması vardır. Konum ve zamanla değişen örüntüler, çeşitli uzay-zaman kısmi türevsel denklem sınıfları tarafından açıklanmaktadır. Tepkime-taşıma problemleri modelleme için, asıl olarak dördüncü dereceden bir taşıma denklemi olan ve Cahn-Hilliard türü denklemi kullanan bu sınıflardan birini oluşturur. Bu çalışma, kendiliğinden yapılanma sürecinde mekanik gerilmelerin oluşturulan örüntü üzerindeki etkisini konu almaktadır. Mekanik davranışta hem elastisite hem de viskoelastisite dikkate alınmaktadır. Bu amaçla Cahn-Hilliard denklemleri doğrusal momentumun korunum denklemi ile birlikte çözülmüştür. Birleştirilmiş kısmi türevsel denklemleri çözmek için sonlu elemanlar yöntemi kullanılmaktadır. Mekanikle bağlaşık çeşitli kendili-

ğinden yapılanma problemlerinin yeni malzemelerin tasarımına olanaklar yaratacağı ve yeni deneylere yol açacağı ön görülmektedir. Bağlaşık ya da ayrık faz ayrımı ve kendiliğinden yapılanma problemlerinin özelliklerini ve fiziğini göstermek için çok sayıda temsili sayısal örnek sunulmaktadır.

Anahtar Kelimeler: Kendiliğinden yapılanma, Cahn-Hilliard denklemi, (Visco-)elastisite, Sonlu elemanlar yöntemi, Faz ayrılması

To all my loved ones

ACKNOWLEDGMENTS

First of all, I would like to express my appreciation and gratitude to my thesis advisor, Dr. Serdar Göktepe, for his guidance and support. Our meetings helped to solve the problems where I had difficulties. I am grateful to him for sharing his experience and knowledge with me.

I want to thank the members of my thesis examining committee members; Dr. Kağan Tuncay, Dr. Afşin Sarıtaş, Dr. Hakan Argeşo, and Dr. Ercan Gürses, for their interest in my thesis topic and contributions to this study.

In addition, I would like to thank my friends and my colleagues Koray Kaya, Berkay Akçören, Sinan Fırat Dal, Baki Aykut Bilginer, Özgür Paşaoğlu, Mehran Ghasabeh and Sepehr Seyedian Choubi for their support and advice during my thesis.

Also, I would like to thank my family for their continuous support and encouragement throughout my life.

TABLE OF CONTENTS

LIST OF TABLES

TABLES

LIST OF FIGURES

FIGURES

LIST OF ABBREVIATIONS

tol	Tolerance
FEM	Finite Element Method
PDE	Partial Differential Equation
FEniCS	Finite Element Analysis Program
Firedrake	Finite Element Analysis Program
CH	Cahn-Hilliard
1-D	One-Dimensional
2-D	Two-Dimensional
3-D	Three-Dimensional

CHAPTER 1

INTRODUCTION

1.1 Motivation and Problem Definition

From the invention of the wheel to cannonballs to aircraft design, the shape and geometry of a product have great importance. If we look at the situation from the material side, the shapes of the molecules can give the material different properties [2]. The unique and complex nanostructure of the materials will give those materials very interesting properties such as optical tunability [3, 4]. It is exciting to design new material structures and produce new materials by considering the concepts of geometry and shape [5]. Moreover, shape is important in self-assembly since it helps to recognize particle [6], it assists in determining the structure and density of the particle packings [7, 8, 9, 10, 11], and it can ease the bindings from ligand molecules [12, 13].

The self-assembly is generally defined as the natural formation of a certain three-dimensional geometry by molecules under a certain condition [14]. Therefore, self-assembly represents a thermodynamic process. The organized structure is obtained by the transition of the system towards its minimum free energy state [15]. The formation of micelles fits the self-assembly scheme, and it is maybe one of the most studied systems in the self-assembly topic. Also, this may be the first studied topic in the context of self-assembly. To give a thermodynamic explanation for this system, it starts from the equilibrium between surfactant micelles and surfactant molecules [14]. The formation of micelles is often called surfactant self-assembly. Surfactant self-assembly is the self-assembly of surfactant molecules in a solvent. Thus, it can form different types of aggregate structures. Some of these aggregate structures are spherical micelle, cylindrical micelle, bilayer, bicontinuous bilayer, reverse cylindri-

cal micelle, and reverse spherical micelle. General schema [1] is depicted in Figure 1.1. Generally, surfactant molecules have two separate parts. Those are hydrophilic and hydrophobic. The hydrophilic part has an affinity towards the water, and the hydrophobic part stays away from water. The surfactant self-assembly is well formulated in the 1970s [16].

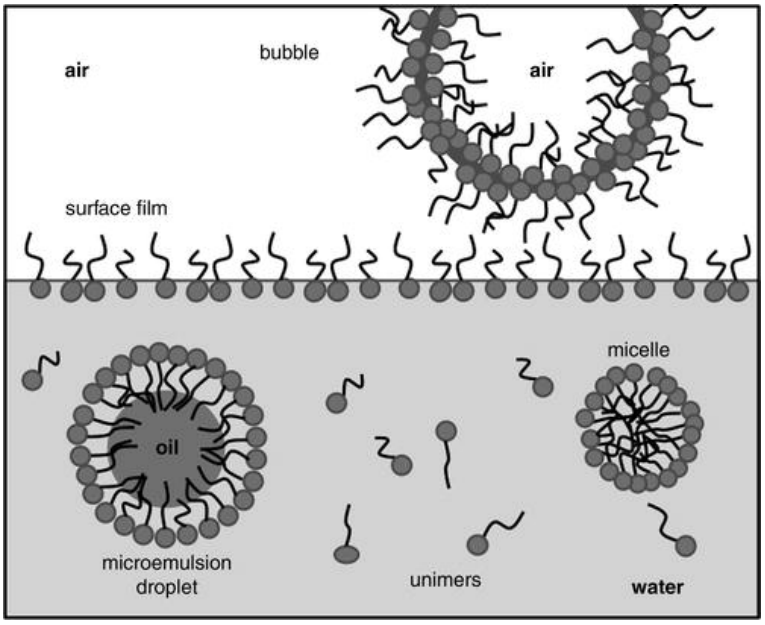

Figure 1.1: General schema for surfactant self assembly [1]

The surfactant self-assembly formulation is successfully applied to the self-assembly of amphiphilic polymers, which is similar to the surfactant self-assembly [17]. One example of amphiphilic polymers is block copolymers. The self-assembly formulations are useful to predict the characteristic behavior such as micelle size and aggregation number.

There are many examples of the self-assembly phenomena in nature, and those examples are not limited to surfactant self-assembly. The self-assembly of dendritic polymers [18], the formation of metal and semiconductor that is due to the self-assembly of atoms [19], protein folding [20], producing virus [21], and fabricating a nanostructure [22] are examples of self-assembly which have an association unit different than surfactant molecule. Therefore, self-assembly covers a wide range of association units.

According to the size of association units, self-assembly is mainly classified as atomic, molecular, and colloidal self-assembly. Polymeric self-assembly is considered as molecular self-assembly. In addition to these, the self-assembly process can occur in a biological system or interface. Biological systems are intriguing because many self-assembly processes occur. Therefore, self-assembly is classified according to the system where it occurs. Biological and interfacial self-assembly is an example for this classification. These classifications are illustrated in Figure 1.2.

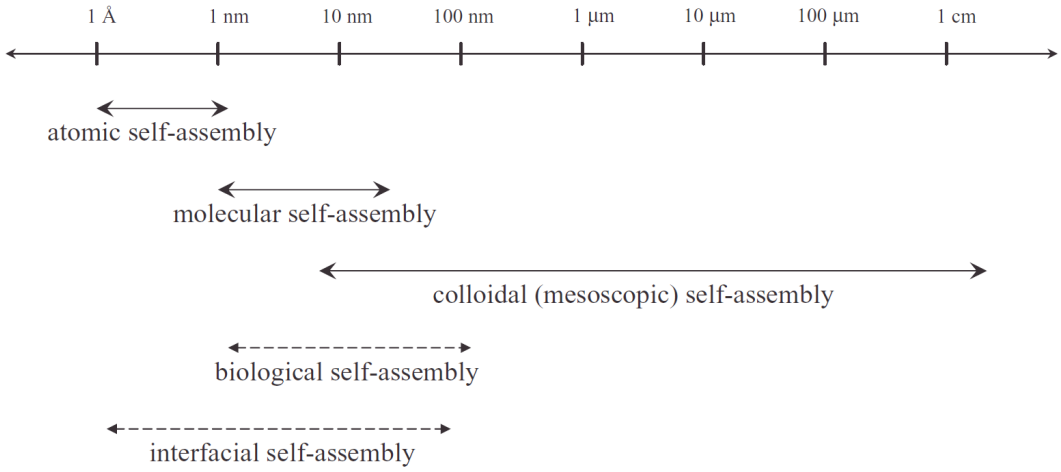

Figure 1.2: Classification of the self-assembly phenomenon

Materials science has greatly improved thanks to two different material design concepts. These concepts are self-assembly [23, 24] and responsive matter [25, 26].

The responsive materials assist in the transport of ions and molecules and can change their adhesion properties with environmental stimuli [27]. Furthermore, it can transform chemical signals into electrical, thermal, optical, and mechanical signals. It can also do the opposite of these signal conversions. The responsive matters can be used in areas such as drug delivery [28, 29, 30], diagnostics, tissue engineering [31], biosensors and bio-applications [32, 33].

In this thesis, we mainly focus on the self-assembly process, specifically the self-assembly of block copolymers. That is an important research area since it offers a variety of morphologies such as spheres, cylinders, bicontinuous structures, vesicles, and lamellae [3]. These morphologies have many practical applications in many

fields such as biomedicine, biomaterials, microelectronics, photoelectric materials, catalysts [34, 35, 36, 37]. In literature, modeling of self-assembly is done mostly at the molecular level. However, in literature, there are some studies to model the self-assembly of block copolymer using the Cahn-Hilliard equations at the large scales [38, 39]. In addition to this, [40] and [41] couple the Cahn-Hilliard equation with mechanics. In this thesis, we combined these studies. Then, we investigate the effects of mechanics on the self-assembly process.

1.2 Scope of Thesis

In this study, we deal with modeling the self-assembly of block copolymer using the Cahn-Hilliard equations and couple these equations with the conservation of the linear momentum equation. The detail of the models is in the following chapters. The aim of the thesis is to add the contribution of modeling of self-assembly considering the mechanical stresses at the continuum scale to the literature.

Unless otherwise stated, FEniCS is used in order to solve all problems in this thesis. FEniCS is a open-source computing platform for solving partial differential equations (PDEs) using finite element method [42]. These solutions are mostly obtained using the Google Colab. Google Colab provides the ability to run python codes in the cloud [43]. Moreover, the Backward-Euler method is used for the time discretization for all problems. For visualizations of the solutions in this thesis, Paraview is used [44].

1.3 Contributions and Novelties

Our contributions are as follows:

- We add an extra interface stretch coupling term, which is different from volumetric swelling in the coupling of the Cahn-Hilliard equation and finite elasticity. The details of the term are in Chapter 3.
- We contribute to the literature by adding the coupling of the Cahn-Hilliard equation and finite viscoelasticity.

- We consider the self-assembly with the effect of finite viscoelasticity at the continuum scale.

1.4 Outline of Thesis

In Chapter 2, the Cahn-Hilliard equation is derived through the Ginzburg-Landau free energy functional. Furthermore, different types of the Cahn-Hilliard equations are presented, such as the Cahn-Hilliard-Oono equation, the Cahn-Hilliard equation with the proliferation term and the fidelity term. Numerous numerical examples are also presented to illustrate the behavior of the Cahn-Hilliard equation.

In Chapter 3, the Cahn-Hilliard equation is solved together with the conservation equation of linear momentum. Volumetric deformation is selected as a coupling parameter.

Chapter 4 is devoted to the modeling of self-assembly via two coupled Cahn-Hilliard equations.

In Chapter 5 we combined the self-assembly process with the mechanics. For mechanics, we have examined the case considering finite viscoelasticity.

In Chapter 6, concluding remarks regarding the obtained results and the future works are provided.

CHAPTER 2

CAHN-HILLIARD EQUATION

2.1 Cahn-Hilliard Equation

The Cahn–Hilliard (CH) equation was proposed by Cahn and Hilliard in order to model phase separation process in binary solution [45, 46, 47, 48]. The fourth-order Cahn-Hilliard equation is expressed as

$$\frac{\partial c}{\partial t} = \operatorname{div}\left(\mathbf{M}\nabla_{\boldsymbol{x}}\left(f'(c) - \epsilon\nabla_{\boldsymbol{x}}^2 c\right)\right) \tag{2.1}$$

where c is the concentration/order parameter, $\mathbf{M}$ is the mobility tensor, $f(c)$ denotes local free energy per unit volume, ϵ is the surface parameter and t is time.

Moreover, div and $\nabla_{\boldsymbol{x}}$ denote the divergence and gradient operators through the spatial position x. Note that $f'(c) := \frac{df(c)}{dc}$

2.1.1 Derivation of Cahn-Hilliard Equation

Before we outline the derivation of the Cahn-Hilliard equation, let us derive the mass transport equation.

2.1.1.1 Derivation of Mass Transport Equation

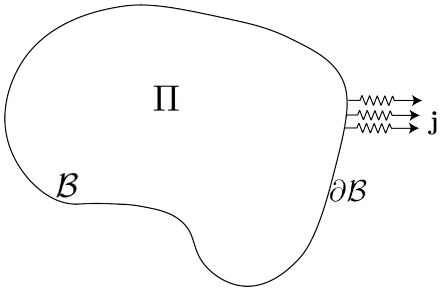

Figure 2.1: The mass conservation over the domain $\mathcal{B}$

Π is a source term that represents the number of particles created per unit volume per unit time due to a chemical reaction. $\mathbf{j}$ is the flux vector that represents number of particle leaving per unit surface area per unit time. The mass conservation equation is expressed as

$$\begin{aligned} &\text{summation of mass } \big|_{\text{in}} - \text{ summation of mass } \big|_{\text{out}} \\ &+ \left\{ \begin{array}{c} \text{generation} \\ \text{or depletion} \\ \text{by chemical reaction} \end{array} \right\} = \text{ rate of mass [49]} \end{aligned} \tag{2.2}$$

The concentration field, $c(\boldsymbol{x}, t)$ is defined as the number of particles per unit volume; that is,

$$c := \lim_{\Delta V \to 0} \frac{\Delta N}{\Delta V}$$

where N is the number of particles and V is the volume. The mathematical form of Equation (2.2) can then be written as follows

$$\frac{d}{dt} \int_{\mathcal{B}} c dV = \int_{\mathcal{B}} \Pi dV - \int_{\partial\mathcal{B}} \mathbf{j} \cdot \mathbf{n} dA \tag{2.3}$$

where $\mathbf{n}$ is the unit normal vector of the surface of body.

By using the Gauss Divergence theorem, (2.3) can be written as follows.

$$\int_{\mathcal{B}} \frac{\partial c}{\partial t} dV = \int_{\mathcal{B}} \Pi dV - \int_{\mathcal{B}} \operatorname{div} \mathbf{j} dV \tag{2.4}$$

$$\int_{\mathcal{B}} \left(\frac{\partial c}{\partial t} - \Pi + \operatorname{div} \mathbf{j} \right) dV = 0 \tag{2.5}$$

Through localization, we obtain the local mass balance equation.

$$\frac{\partial c}{\partial t} - \Pi + \operatorname{div} \mathbf{j} = 0 \text{ in } \mathcal{B} \times (0, T] \tag{2.6}$$

where $\mathcal{B}$ and $(0, T]$ represent the spatial and time domain respectively.

The Cahn-Hilliard equation can then be derived as follows. Consider the following free energy functional, which is called Ginzburg–Landau free energy:

$$\Psi_{\mathcal{B}}(c, \nabla_{\boldsymbol{x}} c) = \int_{\mathcal{B}} \hat{\psi}_{\mathcal{B}}(c, \nabla_{\boldsymbol{x}} c) dV = \int_{\mathcal{B}} \left(\frac{\epsilon}{2} |\nabla_{\boldsymbol{x}} c|^2 + f(c) \right) dV \tag{2.7}$$

where $|.|$ denotes the Euclidean norm and $\mathcal{B} \subset \mathbf{R}^n$ with n =1,2, or 3, is the spatial domain. Then, the chemical potential μ is defined as the variational derivative of $\hat{\psi}_{\mathcal{B}}(c, \nabla_{\boldsymbol{x}} c)$.

$$\mu := \frac{\delta \hat{\psi}_{\mathcal{B}}}{\delta c} = -\epsilon \nabla_{\boldsymbol{x}}^2 c + f'(c) \tag{2.8}$$

Note that the variational derivative defined as

$$\frac{\delta f(y, \nabla_{\boldsymbol{x}} y)}{\delta y} := \partial_y f(y, \nabla_{\boldsymbol{x}} y) - \operatorname{div} \left[\partial_{\nabla_{\boldsymbol{x}} y} f(y, \nabla_{\boldsymbol{x}} y) \right] \tag{2.9}$$

and $\nabla_{\boldsymbol{x}}^2 (\bullet) := \operatorname{div} (\nabla_{\boldsymbol{x}} (\bullet))$. The mass balance equation without source term is

$$\frac{\partial c}{\partial t} = -\operatorname{div} \mathbf{h} \tag{2.10}$$

where $\mathbf{h}$ is the mass flux vector [50] which is related to the chemical potential μ by the following constitutive equation. $\mathbf{h} = \mathbf{j}$

$$\mathbf{h} = -\mathbf{M}\nabla_{\boldsymbol{x}}\mu \tag{2.11}$$

When Equation (2.8) is inserted in Equation (2.11) and Equation (2.11) is inserted into Equation (2.10), we obtain the Cahn-Hilliard equation.

$$\frac{\partial c}{\partial t} = \operatorname{div}\left(\mathbf{M}\nabla_{\boldsymbol{x}}(f'(c) - \epsilon\nabla^2_{\boldsymbol{x}}c)\right) \tag{2.12}$$

2.1.2 Cahn-Hilliard Problem

In order to solve the Cahn-Hilliard equation, we need to specify boundary conditions, an initial condition, and a local free energy function. We can write Cahn-Hilliard problems as follows.

$$\frac{\partial c}{\partial t} - \operatorname{div}\mathbf{M}\left(\nabla_{\boldsymbol{x}}\left(f'(c) - \epsilon\nabla^2_{\boldsymbol{x}}c\right)\right) = 0 \qquad \text{in } \mathcal{B} \tag{2.13a}$$

$$\mathbf{M}\left(\nabla_{\boldsymbol{x}}\left(f'(c) - \epsilon\nabla^2_{\boldsymbol{x}}c\right)\right)\cdot\mathbf{n} = 0 \qquad \text{on } \partial\mathcal{B}, \tag{2.13b}$$

$$\epsilon\mathbf{M}\nabla_{\boldsymbol{x}}c\cdot\mathbf{n} = 0 \qquad \text{on } \partial\mathcal{B}. \tag{2.13c}$$

$$c = c_0 \qquad \text{in } \mathcal{B} \text{ at } t = 0 \tag{2.13d}$$

Equations (2.13b) and (2.13c) show the flux free boundary condition for chemical potential and concentration, respectively.

2.1.3 Solution of Cahn-Hilliard Problem by using C_0 elements

First, we need to split the Cahn-Hilliard equation into two second-order partial differential equations. Because this is a fourth-order partial differential equation and casting it in a weak form would result in the presence of second-order spatial derivatives. Therefore, we can not solve it by standard Lagrangian finite element basis since it consists of C_0 elements. The problem must be rephrased by two coupled second-order partial differential equations.

Substituting Equation (2.8) to Equation (2.12), we obtain the Cahn-Hilliard equation as splited two second-order coupled partial differential equations [51]:

$$\begin{aligned} \frac{\partial c}{\partial t} &= \operatorname{div}(\mathbf{M}\nabla_{\boldsymbol{x}}\mu) \\ \mu &= f'(c) - \epsilon\nabla_{\boldsymbol{x}}^2 c \end{aligned} \tag{2.14}$$

Generally the Cahn-Hilliard Problem has fully homogeneous Neumann boundary conditions. Using Equation (2.8), we get boundary conditions as following form

$$\begin{aligned} (\mathbf{M}\nabla_{\boldsymbol{x}}\mu)\cdot\mathbf{n} &= 0 \quad \text{on } \partial\mathcal{B}, \\ \epsilon\mathbf{M}\nabla_{\boldsymbol{x}} c\cdot\mathbf{n} &= 0 \quad \text{on } \partial\mathcal{B}. \end{aligned} \tag{2.15}$$

Simplify Equation (2.15) to obtain

$$\begin{aligned} \nabla_{\boldsymbol{x}}\mu\cdot\mathbf{n} &= 0 \quad \text{on } \partial\mathcal{B}, \\ \nabla_{\boldsymbol{x}} c\cdot\mathbf{n} &= 0 \quad \text{on } \partial\mathcal{B}. \end{aligned} \tag{2.16}$$

Then the strong form of problem becomes:

$$\frac{\partial c}{\partial t} - \operatorname{div}(\mathbf{M}\nabla_{\boldsymbol{x}}\mu) = 0 \qquad \text{in } \mathcal{B} \tag{2.17a}$$

$$\mu - f'(c) + \epsilon\nabla_{\boldsymbol{x}}^2 c = 0 \qquad \text{in } \mathcal{B} \tag{2.17b}$$

$$\nabla_{\boldsymbol{x}}\mu\cdot\mathbf{n} = 0 \qquad \text{on } \partial\mathcal{B}, \tag{2.17c}$$

$$\nabla_{\boldsymbol{x}} c\cdot\mathbf{n} = 0 \qquad \text{on } \partial\mathcal{B}. \tag{2.17d}$$

$$c = c_0 \qquad \text{in } \mathcal{B} \text{ at } t = 0 \tag{2.17e}$$

To solve this problem with the finite element method, it is needed to obtain the weak form of partial differential equations.

Multiply Equation (2.17a) with the test function v

$$\frac{\partial c}{\partial t} v - \operatorname{div}(\mathbf{M}\nabla_{\boldsymbol{x}}\mu) v = 0 \tag{2.18}$$

with

$$v \in V_0 \tag{2.19}$$

V and V_0 are the function spaces and defined as below.

$$V = \left\{ v : \|v\|_{L^2(\mathcal{B})} + \|\nabla_{\boldsymbol{x}} v\|_{L^2(\mathcal{B})} < \infty \right\} \tag{2.20}$$

$$V_0 = \{ v \in V : v|_{\partial\mathcal{B}} = 0 \} \tag{2.21}$$

Integrate Equation (2.18) over the domain $\mathcal{B}$,

$$\int_{\mathcal{B}} \frac{\partial c}{\partial t} v dV - \int_{\mathcal{B}} \operatorname{div}(\mathbf{M}\nabla_{\boldsymbol{x}}\mu) v dV = 0 \tag{2.22}$$

By using integration by parts, we can write the second term of Equation (2.22),

$$\int_{\mathcal{B}} \operatorname{div}(\mathbf{M}\nabla_{\boldsymbol{x}}\mu) v dV = \int_{\mathcal{B}} \operatorname{div}(\mathbf{M}\nabla_{\boldsymbol{x}}\mu v) dV - \int_{\mathcal{B}} (\mathbf{M}\nabla_{\boldsymbol{x}}\mu) \cdot \nabla_{\boldsymbol{x}} v dV \tag{2.23}$$

According to the divergence theorem, the first-term on the right side of Equation (2.23) becomes:

$$\int_{\mathcal{B}} \operatorname{div}(\mathbf{M}\nabla_{\boldsymbol{x}}\mu v) dV = \int_{\partial\mathcal{B}} v \mathbf{M}\nabla_{\boldsymbol{x}}\mu \cdot \mathbf{n} dA \tag{2.24}$$

This term vanishes due to the Neumann boundary condition in Equation (2.17c).

$$\nabla_{\boldsymbol{x}}\mu \cdot \mathbf{n} = 0 \text{ on } \partial\mathcal{B} \tag{2.25}$$

$$\int_{\mathcal{B}} \operatorname{div}(\mathbf{M}\nabla_{\boldsymbol{x}}\mu v) dV = 0 \tag{2.26}$$

Therefore, Equation (2.24) becomes

$$\int_{\mathcal{B}} \operatorname{div}(\mathbf{M}\nabla_{\boldsymbol{x}}\mu) v dV = -\int_{\mathcal{B}} (\mathbf{M}\nabla_{\boldsymbol{x}}\mu) \cdot \nabla_{\boldsymbol{x}} v dV \tag{2.27}$$

Substituting the result in Equation (2.27) into Equation (2.22), we get the weak form of Equation (2.17a)

$$\int_{\mathcal{B}} \frac{\partial c}{\partial t} v dV + \int_{\mathcal{B}} (\mathbf{M} \nabla_{\boldsymbol{x}} \mu) \cdot \nabla_{\boldsymbol{x}} v dV = 0 \quad \forall v \in V_0 \tag{2.28}$$

Also, we need the weak form of Equation (2.17b). To obtain that, multiply Equation (2.17b) by the test function q.

$$q \in V_0 \tag{2.29}$$

$$\mu q - f'(c) q + \epsilon \nabla_{\boldsymbol{x}}^2 c q = 0 \tag{2.30}$$

Integrate Equation (2.30) over the domain $\mathcal{B}$,

$$\int_{\mathcal{B}} \mu q dV - \int_{\mathcal{B}} f'(c) q dV + \int_{\mathcal{B}} \epsilon \nabla_{\boldsymbol{x}}^2 c q dV = 0 \tag{2.31}$$

By using integration by parts, we can write last term of Equation (2.31),

$$\int_{\mathcal{B}} \epsilon \nabla_{\boldsymbol{x}}^2 c q dV = \int_{\mathcal{B}} \epsilon \operatorname{div}(\nabla_{\boldsymbol{x}} c q) dV - \int_{\mathcal{B}} \epsilon \nabla_{\boldsymbol{x}} c \cdot \nabla_{\boldsymbol{x}} q dV \tag{2.32}$$

Similarly, by the divergence theorem, the first term on the left side of Equation (2.32) becomes:

$$\int_{\mathcal{B}} \epsilon \operatorname{div}(\nabla_{\boldsymbol{x}} c q) dV = \int_{\partial \mathcal{B}} \epsilon \nabla_{\boldsymbol{x}} c \cdot \mathbf{n} q dA = 0 \tag{2.33}$$

Since $\nabla_{\boldsymbol{x}} c \cdot \mathbf{n} = 0$ on $\partial \mathcal{B}$

$$\int_{\mathcal{B}} \epsilon \nabla_{\boldsymbol{x}}^2 c q dV = - \int_{\mathcal{B}} \epsilon \nabla_{\boldsymbol{x}} c \cdot \nabla_{\boldsymbol{x}} q dV \tag{2.34}$$

Then weak form of Equation (2.17b) becomes

$$\int_{\mathcal{B}} \mu q dV - \int_{\mathcal{B}} f'(c) q dV - \int_{\mathcal{B}} \epsilon \nabla_{\boldsymbol{x}} c \cdot \nabla_{\boldsymbol{x}} q dV = 0 \quad \forall q \in V_0 \tag{2.35}$$

The weak form of the Cahn-Hilliard problem is then given by

Find $c \in V$ and $\mu \in V$ such that

$$\int_{\mathcal{B}} \frac{\partial c}{\partial t} v dV + \int_{\mathcal{B}} (\mathbf{M} \nabla_{\boldsymbol{x}} \mu) \cdot \nabla_{\boldsymbol{x}} v dV = 0 \quad \forall v \in V_0 \tag{2.36a}$$

$$\int_{\mathcal{B}} \mu q dV - \int_{\mathcal{B}} f'(c) q dV - \int_{\mathcal{B}} \epsilon \nabla_{\boldsymbol{x}} c \cdot \nabla_{\boldsymbol{x}} q dV = 0 \quad \forall q \in V_0 \tag{2.36b}$$

$$c = c_0 \text{ in } \mathcal{B} \text{ at } t = 0 \tag{2.36c}$$

This system of equations is nonlinear since $f'(c)$ in (2.36b) has nonlinear terms of c. To solve it, we need to linearize the problem [52]. There are many methods to linearize the Cahn-Hilliard problem, such as the Eyre's method (EY) [53], the Optimal dissipation method (OD2) [54], the Wu-Van Zwieten-Van der Zee's method (WVV) [55], and the Linear splitting method (LS) [38]. However, we will use Newton's Method to linearize the problem. Before linearization, we need to create a mixed-function space to obtain a monolithic solution.

Define $u = (c \times \mu)$, $u \in (V \times V)$ and $w = (v \times q)$, $w \in (V_0 \times V_0)$. In other words, u is a function of the mixed function space and w is the test function of the mixed function space.

$$\begin{aligned} \mathcal{F}(u, w) = & \int_{\mathcal{B}} \frac{\partial c}{\partial t} v dV + \int_{\mathcal{B}} (\mathbf{M} \nabla_{\boldsymbol{x}} \mu) \cdot \nabla_{\boldsymbol{x}} v dV \\ & + \int_{\mathcal{B}} \mu q dV - \int_{\mathcal{B}} f'(c) q dV - \int_{\mathcal{B}} \epsilon \nabla_{\boldsymbol{x}} c \cdot \nabla_{\boldsymbol{x}} q dV \\ & \forall (v \times q) \in (V_0 \times V_0) \end{aligned} \tag{2.37}$$

Find $u = (c \times \mu) \in (V \times V)$ such that

$$\mathcal{F}(u, w) = 0 \quad \forall (v \times q) \in (V_0 \times V_0) \tag{2.38a}$$

$$c = c_0 \text{ in } \mathcal{B} \text{ at } t = 0 \tag{2.38b}$$

2.1.3.1 Linearization of Weak Form of Cahn-Hilliard Equations

Let us assume the solution of the problem (2.38) is $u = u^0 + \delta u$. Through the Taylor series expansion of $\mathcal{F}(u, w) = \mathcal{F}(u^0 + \delta u, w)$ around u^0 we have

$$\mathcal{F}\left(u^0 + \delta u\right) = \mathcal{F}\left(u^0\right) + \frac{\delta \mathcal{F}}{\delta u}\left(u^0\right)\delta u + O\left(\delta u^2\right) \tag{2.39}$$

Neglecting all terms quadratic in δu, we end up with a linear equation.

Find $\delta u \in (V \times V)$ *such that*

$$\mathcal{F}\left(u^0 + \delta u\right) \approx \mathcal{F}\left(u^0\right) + \frac{\delta \mathcal{F}}{\delta u}\left(u^0\right)\delta u = 0 \tag{2.40}$$

Solving Equation (2.40), for δu we obtain

$$\delta u = -\mathcal{J}^{-1}\mathcal{F}\left(u^0\right) \tag{2.41}$$

where

$$\mathcal{J} := \frac{\delta \mathcal{F}}{\delta u}\left(u^0\right) \tag{2.42}$$

Once we have solved Equation (2.41) for δu, we then iterate with the Newton-Galerkin method for new solution guess.

2.1.3.2 Finite Element Approximation

Let $\mathcal{K}$ be a triangulation of $\mathcal{B}$ and V_h be the space of continuous piece-wise linear basis functions on $\mathcal{K}$. Replacing V with V_h, we obtain the finite element approximation.

$$V_{h,0} = \{v \in V_h : v|_{\partial\mathcal{B}} = 0\} \tag{2.43}$$

$$\begin{aligned}\mathcal{F}(u_h, w) = &\int_{\mathcal{B}} \frac{\partial c_h}{\partial t} v dV + \int_{\mathcal{B}} M \nabla_{\boldsymbol{x}} \mu_h \cdot \nabla_{\boldsymbol{x}} v dV \\ &+ \int_{\mathcal{B}} \mu_h q dV - \int_{\mathcal{B}} f'(c_h) q dV - \int_{\mathcal{B}} \epsilon \nabla_{\boldsymbol{x}} c_h \cdot \nabla_{\boldsymbol{x}} q dV \\ &\forall (v \times q) \in (V_{h,0} \times V_{h,0})\end{aligned} \tag{2.44}$$

Therefore, the discretized problem becomes

Find $u_h = (c_h \times \mu_h) \in (V_h \times V_h)$ *such that*

$$\mathcal{F}(u_h, w) = 0 \quad \forall (v \times q) \in (V_{h,0} \times V_{h,0}) \tag{2.45a}$$

$$c_h = c_0 \text{ in } \mathcal{B} \text{ at } t = 0 \tag{2.45b}$$

After linearization of the discretized form,

Find $\delta u_h \in (V_h \times V_h)$ *such that*

$$\mathcal{F}\left(u_h^0 + \delta u_h, w\right) \approx \mathcal{F}\left(u_h^0, w\right) + \frac{\delta \mathcal{F}}{\delta u_h}\left(u_h^0, w\right) \delta u_h = 0 \tag{2.46}$$

where

$$\mathcal{J}\left(\delta u_h, w\right) = \frac{\delta \mathcal{F}}{\delta u_h}\left(u_h^0\right)\left(\delta u_h, w\right) \tag{2.47}$$

The discretized and linearized residual is

$$r\left(w\right) = \mathcal{F}(u_h^0, w) \tag{2.48}$$

The solution of the linear equation is expressed as

$$\delta u_h = -\mathcal{J}\left(\delta u_h, w\right)^{-1} r\left(w\right) \tag{2.49}$$

Both spaces V_h and $V_{h,0}$ have the same basis functions. Since $\delta u_h \in V_h$ and $w_h \in V_{h,0}$, we can write them as the linear combination of the basis functions of the space V_h.

$$\delta u_h = \sum_{j=1}^{n_i} d_j \varphi_j \tag{2.50a}$$

$$w_h = \sum_{i=1}^{n_i} \varphi_i \tag{2.50b}$$

where d_j, $j = 1, 2..., n_i$ are n_i unknown components to be determined, n_i represent the number of unknown components. φ_j, $j = 1, 2..., n_i$ are the basis functions spanning the space V_h

Inserting equations (2.50) into (2.47), we get

$$J_{ij} = \mathcal{A}\left\{\mathcal{J}\left(\sum_{j=1}^{n_i} d_j \varphi_j, \sum_{i=1}^{n_i} \varphi_i\right)\right\} \tag{2.51}$$

where J_{ij} are the entries of $\mathbf{J}$ that is the $n_i \times n_i$ Jacobian matrix. Furthermore, note that $\mathcal{A}$ denotes assembly operator.

$$r_i = \mathcal{A}\left\{r\left(\sum_{i=1}^{n_i} \varphi_i\right)\right\} \tag{2.52}$$

where $\mathbf{r}$ is the $n_i \times 1$ so-called residual vector. In matrix form we write

$$\mathbf{J}\mathbf{d} = -\mathbf{r} \tag{2.53}$$

The algorithm of the Newton-Galerkin Method for the Cahn-Hilliard equation is presented in Algorithm 1.

Algorithm 1 NEWTON-GALERKIN METHOD FOR THE CAHN-HILLIARD EQUATION FOR ONE TIME-STEP

1: Choose a starting guess $u_h^{(0)} \in (V_h \text{ x } V_h)$ and desired tolerance tol.

2: **for** k= 0,1,2... **do**

3: Assemble the Jacobian matrix $J^{(k)}$ and the residual vector $r^{(k)}$ with entries

$$J_{ij}^{(k)} = \mathcal{A}\left\{\mathcal{J}\left(\sum_{j=1}^{n_i} d_j\varphi_j, \sum_{i=1}^{n_i}\varphi_i\right)\right\}$$

$$r_i^{(k)} = \mathcal{A}\left\{r\left(\sum_{i=1}^{n_i}\varphi_i\right)\right\}$$

4: Solve the linear system.

$$\mathbf{J}\mathbf{d} = -\mathbf{r}$$

5: Set $u_h^{(k+1)} = u_h^{(k)} + \delta u_h^{(k)}$, where $\delta u_h^{(k)} = \sum_{j=1}^{n_i} d_j\varphi_j$

6: **if** $\left\|\delta u_h^{(k)}\right\| < tol$ **then**

BREAK

endif

7: **endfor**

2.1.4 Solution of Cahn-Hilliard Problem by using C_1 elements

Recall the Cahn-Hilliard problem:

$$\frac{\partial c}{\partial t} - \operatorname{div}\left[\mathbf{M}\left(\nabla_{\boldsymbol{x}}\left(f'(c) - \epsilon\nabla^2_{\boldsymbol{x}}c\right)\right)\right] = 0 \qquad \text{in } \mathcal{B} \tag{2.54a}$$

$$\mathbf{M}\left(\nabla_{\boldsymbol{x}}\left(f'(c) - \epsilon\nabla^2_{\boldsymbol{x}}c\right)\right) = 0 \qquad \text{on } \partial\mathcal{B}, \tag{2.54b}$$

$$\epsilon(\mathbf{M}\nabla_{\boldsymbol{x}}c)\cdot\mathbf{n} = 0 \qquad \text{on } \partial\mathcal{B}. \tag{2.54c}$$

Multiply (2.54a) by the test function $\phi \in \mathcal{H}^2$ to obtain the weak form of the fourth-order Cahn-Hilliard equation. $\mathcal{H}^2$ is the Hilbert space of functions with square-integrable second derivatives. Note that, the Hilbert space is a vector space that has norm definition by the inner product [56].

$$\left(\frac{\partial c}{\partial t}, \phi\right) = \left(\operatorname{div}\mathbf{M}\nabla_{\boldsymbol{x}}(f'(c) - \epsilon\nabla^2_{\boldsymbol{x}}c), \phi\right) \tag{2.55}$$

For simplicity, the interior and boundary inner products are used instead of integral form. We define the interior and boundary inner products as:

$$(\mathbf{A}, \mathbf{B}) := \int_{\mathcal{B}} \mathbf{A} : \mathbf{B}dV \tag{2.56a}$$

$$\langle \mathbf{A}, \mathbf{B}\rangle := \int_{\partial\mathcal{B}} \mathbf{A} : \mathbf{B}dA, \tag{2.56b}$$

Integrate by parts,

$$\begin{aligned}\left(\operatorname{div}\mathbf{M}[\nabla_{\boldsymbol{x}}(f'(c) - \epsilon\nabla^2_{\boldsymbol{x}}c)], \phi\right) = &\left(\operatorname{div}\left(\mathbf{M}\nabla_{\boldsymbol{x}}(f'(c) - \epsilon\nabla^2_{\boldsymbol{x}}c)\phi\right), 1\right) \\ &- \left(\left(\mathbf{M}\nabla_{\boldsymbol{x}}(f'(c) - \epsilon\nabla^2_{\boldsymbol{x}}c)\right), \nabla_{\boldsymbol{x}}\phi\right)\end{aligned} \tag{2.57}$$

Using the divergence theorem, the first term in (2.57) can be written as

$$\begin{aligned}\left(\operatorname{div}\left(\mathbf{M}\nabla_{\boldsymbol{x}}(f'(c) - \epsilon\nabla^2_{\boldsymbol{x}}c)\phi\right), 1\right) &= \left\langle \mathbf{M}\nabla_{\boldsymbol{x}}(f'(c) - \epsilon\nabla^2_{\boldsymbol{x}}c)\cdot\mathbf{n}, \phi\right\rangle \\ &= 0\end{aligned} \tag{2.58}$$

Due to boundary condition in (2.54b), Equation (2.58) vanishes. When we insert (2.58), (2.57) into (2.55), we arrive at

$$\begin{aligned}\left(\frac{\partial c}{\partial t}, \phi\right) &= -\left(\left(\mathbf{M}\nabla_{\boldsymbol{x}}(f'(c) - \epsilon\nabla^2_{\boldsymbol{x}}c)\right), \nabla_{\boldsymbol{x}}\phi\right) \\ &= -\left(\left(\nabla_{\boldsymbol{x}}(f'(c) - \epsilon\nabla^2_{\boldsymbol{x}}c)\right), \mathbf{M}^T\nabla_{\boldsymbol{x}}\phi\right)\end{aligned} \tag{2.59}$$

since M is space-invariant. We can integrate the last term in (2.59) by parts once more.

$$\begin{aligned}\left(\left(\nabla_{\boldsymbol{x}}(f'(c) - \epsilon\nabla^2_{\boldsymbol{x}}c)\right), \mathbf{M}^T\nabla_{\boldsymbol{x}}\phi\right) &= \left(\mathrm{div}((f'(c) - \epsilon\nabla^2_{\boldsymbol{x}}c)\mathbf{M}^T\nabla_{\boldsymbol{x}}\phi), 1\right) \\ &\quad - \left((f'(c) - \epsilon\nabla^2_{\boldsymbol{x}}c), \mathrm{div}\left(\mathbf{M}^T\nabla_{\boldsymbol{x}}\phi\right)\right)\end{aligned} \tag{2.60}$$

The second term in (2.60), can be decomposed into the following two terms

$$\begin{aligned}\left(\mathrm{div}((f'(c) - \epsilon\nabla^2_{\boldsymbol{x}}c)\mathbf{M}^T\nabla_{\boldsymbol{x}}\phi), 1\right) &= \left(\mathrm{div}((f'(c))\mathbf{M}^T\nabla_{\boldsymbol{x}}\phi), 1\right) \\ &\quad - \left(\mathrm{div}((\epsilon\nabla^2_{\boldsymbol{x}}c)\mathbf{M}^T\nabla_{\boldsymbol{x}}\phi), 1\right)\end{aligned} \tag{2.61}$$

By using the product rule, the second term in (2.61) becomes

$$\left(\mathrm{div}((f'(c))\mathbf{M}^T\nabla_{\boldsymbol{x}}\phi), 1\right) = \left((\nabla_{\boldsymbol{x}}(f'(c))), \mathbf{M}^T\nabla_{\boldsymbol{x}}\phi\right) + \left(f'(c), \mathrm{div}\,\mathbf{M}^T\nabla_{\boldsymbol{x}}\phi\right) \tag{2.62}$$

Using the divergence theorem, the last term in (2.61) can be written as

$$\left(\mathrm{div}((\epsilon\nabla^2_{\boldsymbol{x}}c)\mathbf{M}^T\nabla_{\boldsymbol{x}}\phi), 1\right) = \left\langle\epsilon\nabla^2_{\boldsymbol{x}}c, (\mathbf{M}^T\nabla_{\boldsymbol{x}}\phi)\cdot\mathbf{n}\right\rangle \tag{2.63}$$

Inserting the result in (2.62) and (2.63) into (2.61), we obtain

$$\begin{aligned}\left(\mathrm{div}((f'(c) - \epsilon\nabla^2_{\boldsymbol{x}}c)\mathbf{M}^T\nabla_{\boldsymbol{x}}\phi), 1\right) &= \left((\nabla_{\boldsymbol{x}}(f'(c))), \mathbf{M}^T\nabla_{\boldsymbol{x}}\phi\right) + \left(f'(c), \mathrm{div}\,\mathbf{M}^T\nabla_{\boldsymbol{x}}\phi\right) \\ &\quad - \left\langle\epsilon\nabla^2_{\boldsymbol{x}}c, (\mathbf{M}^T\nabla_{\boldsymbol{x}}\phi)\cdot\mathbf{n}\right\rangle\end{aligned} \tag{2.64}$$

Substituting Equation (2.64) into (2.60), we get

$$\begin{aligned}\left(\left(\nabla_{\boldsymbol{x}}(f'(c)-\epsilon\nabla^2_{\boldsymbol{x}}c)\right),\mathbf{M}^T\nabla_{\boldsymbol{x}}\phi\right) &= \left((\nabla_{\boldsymbol{x}}(f'(c))),\mathbf{M}^T\nabla_{\boldsymbol{x}}\phi\right)+\left(f'(c),\operatorname{div}\mathbf{M}^T\nabla_{\boldsymbol{x}}\phi\right)\\ &\quad-\left\langle\epsilon\nabla^2_{\boldsymbol{x}}c,(\mathbf{M}^T\nabla_{\boldsymbol{x}}\phi)\cdot\mathbf{n}\right\rangle\\ &\quad-\left((f'(c)-\epsilon\nabla^2_{\boldsymbol{x}}c),\operatorname{div}\mathbf{M}^T\nabla_{\boldsymbol{x}}\phi\right)\end{aligned} \tag{2.65}$$

If we simplify Equation (2.65)

$$\begin{aligned}\left(\left(\nabla_{\boldsymbol{x}}(f'(c)-\epsilon\nabla^2_{\boldsymbol{x}}c)\right),\mathbf{M}^T\nabla_{\boldsymbol{x}}\phi\right) &= \left(\nabla_{\boldsymbol{x}}(f'(c)),\mathbf{M}^T\nabla_{\boldsymbol{x}}\phi\right)+\left(\epsilon\nabla^2_{\boldsymbol{x}}c,\operatorname{div}\mathbf{M}^T\nabla_{\boldsymbol{x}}\phi\right)\\ &\quad-\left\langle\epsilon\nabla^2_{\boldsymbol{x}}c,(\mathbf{M}^T\nabla_{\boldsymbol{x}}\phi)\cdot\mathbf{n}\right\rangle\end{aligned} \tag{2.66}$$

As we insert Equation (2.66) into (2.59), we obtain the weak form of the Cahn-Hilliard equation

$$\begin{aligned}\left(\frac{\partial c}{\partial t},\phi\right) &= -\left(\nabla_{\boldsymbol{x}}(f'(c)),\mathbf{M}^T\nabla_{\boldsymbol{x}}\phi\right)-\left(\epsilon\nabla^2_{\boldsymbol{x}}c,\operatorname{div}\mathbf{M}^T\nabla_{\boldsymbol{x}}\phi\right)\\ &\quad+\left\langle\epsilon\nabla^2_{\boldsymbol{x}}c,(\mathbf{M}^T\nabla_{\boldsymbol{x}}\phi)\cdot\mathbf{n}\right\rangle\end{aligned} \tag{2.67}$$

Therefore, the integral form of the Equation (2.67) becomes

$$\begin{aligned}\int_{\mathcal{B}}\frac{\partial c}{\partial t}\phi dV &= -\int_{\mathcal{B}}\nabla_{\boldsymbol{x}}f'(c)\cdot\mathbf{M}^T\nabla_{\boldsymbol{x}}\phi dV-\int_{\mathcal{B}}\epsilon\nabla^2_{\boldsymbol{x}}c\operatorname{div}\mathbf{M}^T\nabla_{\boldsymbol{x}}\phi dV\\ &\quad+\int_{\partial\mathcal{B}}\epsilon\nabla^2_{\boldsymbol{x}}c(\mathbf{M}^T\nabla_{\boldsymbol{x}}\phi)\cdot\mathbf{n}dA\end{aligned} \tag{2.68}$$

Note that this weak form can also be used for higher continuity elements than $\mathbf{C}_1$ such as $\mathbf{C}_2$ elements.

2.1.5 Other Models For Phase Separation

In this part, other models that can be used to model the phase separation phenomenon are presented.

2.1.5.1 Allen-Cahn Equation

The moving interface problem is a special type of the initial boundary-value problem. Two-phase problems in fluid dynamics, the interaction between crystals in solids, and the phase transition problems for alloys in materials science are examples of the moving interface problem. Phase-field methods are used in solving the moving interface problem.

This equation has been extensively used to study various physical problems, such as image segmentation, crystal growth, and mean curvature flows [57].

$$\begin{aligned} c_t - \nabla_{\boldsymbol{x}}^2 c + \frac{1}{\epsilon^2} f(c) = 0, \quad (x,t) \in \mathcal{B} \times (0,T] \\ \nabla_{\boldsymbol{x}} c \cdot \mathbf{n} = 0 \\ c(\boldsymbol{x}, 0) = c_0 \end{aligned} \tag{2.69}$$

Weak Form

$$\int_{\mathcal{B}} c_t v dV + \int_{\mathcal{B}} \nabla_{\boldsymbol{x}} c \cdot \nabla_{\boldsymbol{x}} v dV + \int_{\mathcal{B}} \frac{1}{\epsilon^2} f(c) v dV = 0, \quad v \in V \tag{2.70}$$

where $f(c)$ generally has the following form

$$f(c) = c^3 - c \tag{2.71}$$

2.1.5.2 Cahn-Hilliard-Oono Equation

The initial and boundary value problem in (2.72) known as the Cahn–Hilliard–Oono equation [58].

$$\frac{\partial c}{\partial t} + \beta c = \Delta\mu,\ \beta \geq 0 \tag{2.72a}$$

$$\mu = -\nabla_{\boldsymbol{x}}^2 c + f'(c) \tag{2.72b}$$

$$\nabla_{\boldsymbol{x}} c \cdot \mathbf{n} = \nabla_{\boldsymbol{x}} \mu \cdot \mathbf{n} = 0,\ \text{on } \partial\mathcal{B} \tag{2.72c}$$

$$c(\boldsymbol{x}, 0) = c_0 \text{ in } \mathcal{B} \tag{2.72d}$$

The Cahn-Hilliard-Oono equation is an extended version of the Cahn-Hilliard equation since it has an extra term. When $\beta = 0$, we simply get the Cahn-Hilliard equation.

2.1.5.3 Generalized Cahn-Hilliard Equation

The initial and boundary value problem of the generalized Cahn-Hilliard equation is shown below. We have an extra term $g(x, c)$.

$$\begin{gathered} \frac{\partial c}{\partial t} + \Delta^2 c - \Delta f(c) + g(\boldsymbol{x}, c) = 0 \\ \nabla_{\boldsymbol{x}} c \cdot \mathbf{n} = \nabla_{\boldsymbol{x}} (\Delta u - f(c)) \cdot \mathbf{n} = 0,\ \text{on } \partial\mathcal{B} \\ c(\boldsymbol{x}, 0) = c_0 \text{ in } \mathcal{B} \end{gathered} \tag{2.73}$$

- Cahn-Hilliard-Oono equation.

  $$g(\boldsymbol{x}, c) = g(c) = \beta c, \quad \beta \geq 0$$

  This function was proposed to account for long ranged interaction.

- Cahn-Hilliard equation with proliferation term.

  $$g(\boldsymbol{x}, c) = g(c) = \beta c(c-1), \quad \beta \geq 0$$

  This function was proposed to model biological phenomenon such as wound healing and tumor growth.

- Cahn-Hilliard equation with fidelity term.

  $$g(\boldsymbol{x}, c) = \lambda_0 \Xi_{\mathcal{B}\setminus D}(\boldsymbol{x})(c - \varphi(\boldsymbol{x})), \quad \lambda_0 > 0, D \subset \mathcal{B}, \varphi \in L^2(\mathcal{B})$$

Where Ξ denotes the indicator function. This function was proposed for image inpainting.

2.1.5.4 6th-Order Generalized Cahn-Hilliard Equation

Using the anisotropic surface energy makes the Cahn-Hilliard equation challenging to solve. For the sufficiently large degree of anisotropic Cahn-Hilliard equation, we encounter ill-posedness. Willmore or biharmonic regularization makes the problem well-posed [59]. In addition to these, to overcome the ill-posedness of the anisotropic Cahn-Hilliard model, a higher-order derivative term should be added to the surface energy [60]. Therefore, we will obtain a sixth-order Cahn-Hilliard system.

$$\begin{aligned} c_t &= \operatorname{div}(\mathbf{M}\nabla_{\boldsymbol{x}}\mu) - g(\boldsymbol{x}, c) \\ \mu &= f(c) - \nabla_{\boldsymbol{x}}^2 c + \omega f'(c) - \nabla_{\boldsymbol{x}}^2 \omega + \epsilon c_t \\ \omega &= f(c) - \nabla_{\boldsymbol{x}}^2 c \end{aligned} \tag{2.74}$$

2.1.6 Convergence Analysis

2.1.6.1 Method of Manufactured Solution

In this section, we will employ a manufactured solution to verify our approximate solution. Assume the concentration has the following form.

$$\widehat{c} = (t+1)\sin(\alpha\pi\boldsymbol{x}), \tag{2.75}$$

Substituting the function (2.75) in Equation (2.1), we obtain residual $\mathcal{S}$.

$$\frac{\partial \widehat{c}}{\partial t} - \operatorname{div}\left(\mathbf{M}\nabla_{\boldsymbol{x}}\left(f'(\widehat{c}) - \epsilon\nabla_{\boldsymbol{x}}^2\widehat{c}\right)\right) = \mathcal{S} \tag{2.76}$$

where

$$f(\widehat{c}) = \frac{\widehat{c}^4}{4} - \frac{\widehat{c}^2}{2}$$
$$\mathbf{M} = \mathbf{1} \tag{2.77}$$

$$\begin{aligned}\mathcal{S} = &\sin(\alpha\pi\boldsymbol{x}) + 3(t+1)^3\alpha^2\pi^2\sin^3(\alpha\pi\boldsymbol{x}) + \epsilon(t+1)\alpha^4\pi^4\sin(\alpha\pi\boldsymbol{x}) \\ &- (t+1)\alpha^2\pi^2\sin(\alpha\pi\boldsymbol{x}) - 6(t+1)^3\alpha^2\pi^2\sin(\alpha\pi\boldsymbol{x})\cos^2(\alpha\pi\boldsymbol{x})\end{aligned} \tag{2.78}$$

Then we will split the Equation (2.76),

$$\begin{cases} \frac{\partial\widehat{c}}{\partial t} = \operatorname{div}(\nabla_{\boldsymbol{x}}\widehat{\mu}) + \mathcal{S} \\ \widehat{\mu} = -\epsilon\Delta\widehat{c} + f'(\widehat{c}) \end{cases} \tag{2.79}$$

where the chemical potential becomes,

$$\widehat{\mu} = \epsilon(t+1)\alpha^2\pi^2\sin(\alpha\pi\boldsymbol{x}) + (t+1)^3\sin^3(\alpha\pi\boldsymbol{x}) - (t+1)\sin(\alpha\pi\boldsymbol{x}) \tag{2.80}$$

We compute the L^2-error norms and H^1-error norms for convergence analysis. These norms are defined as

$$\begin{aligned}\|\widehat{c} - \widehat{c}_h\|_{L^2(\mathcal{B})} &= \left(\int_{\mathcal{B}} |\widehat{c} - \widehat{c}_h|^2 \, dV\right)^{1/2} \\ \|\widehat{c} - \widehat{c}_h\|_{H^1(\mathcal{B})} &= \left(\int_{\mathcal{B}} \left(|\widehat{c} - \widehat{c}_h|^2 + |\nabla_{\boldsymbol{x}}\left(\widehat{c} - \widehat{c}_h\right)|^2\right) dV\right)^{1/2}\end{aligned} \tag{2.81}$$

The unit square (centered at the origin) domain is considered. The linear Lagrange triangle finite element discretization is used. Four uniform meshes ($50 \times 25 = 1250$, $100 \times 50 = 5000$, $200 \times 100 = 20000$ and $400 \times 200 = 80000$ T1 elements) are created. In Figure 2.2, $50 \times 25 = 1250$ T1 elements mesh are presented. Parameters of problem are presented in Table 2.1. Then $\|\widehat{c} - \widehat{c}_h\|_{L^2(\mathcal{B})}$ and $\|\widehat{c} - \widehat{c}_h\|_{H^1(\mathcal{B})}$ are calculated at the final time, T_{final}. $\widehat{c}$ and $\widehat{c}_h$ denote the manufactured solution and the finite element solution, respectively.

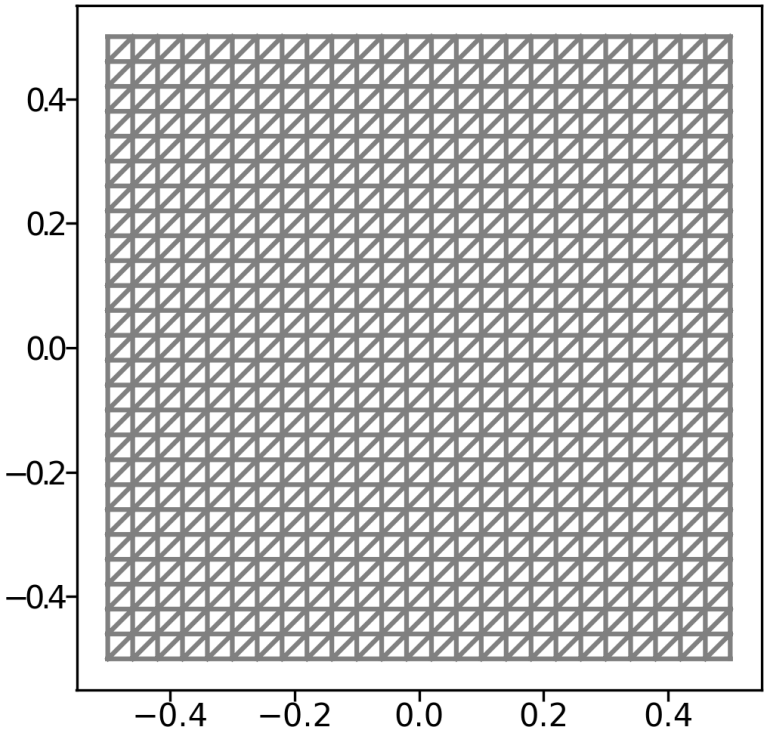

Figure 2.2: $50 \times 25 = 1250$ T1 elements mesh

Table 2.1: The parameters of the L^2-error norms and H^1-error norms example

No.	Parameter	Name	Value
1	$\mathcal{B}$	Domain	$[-0.5, 0.5] \times [-0.5, 0.5]$
2	Δt	Time step	1×10^{-5}
3	ϵ	Surface parameter	1×10^{-4}
4	T_{final}	Final time	1×10^{-3}

The solutions of Equation 2.79 are presented in Figure 2.3. As can be seen from the figures, the finer meshes cause both L^2-error and H^1-error norms to decrease. In other words, the solution converges to the exact solution as the finer meshes are used.

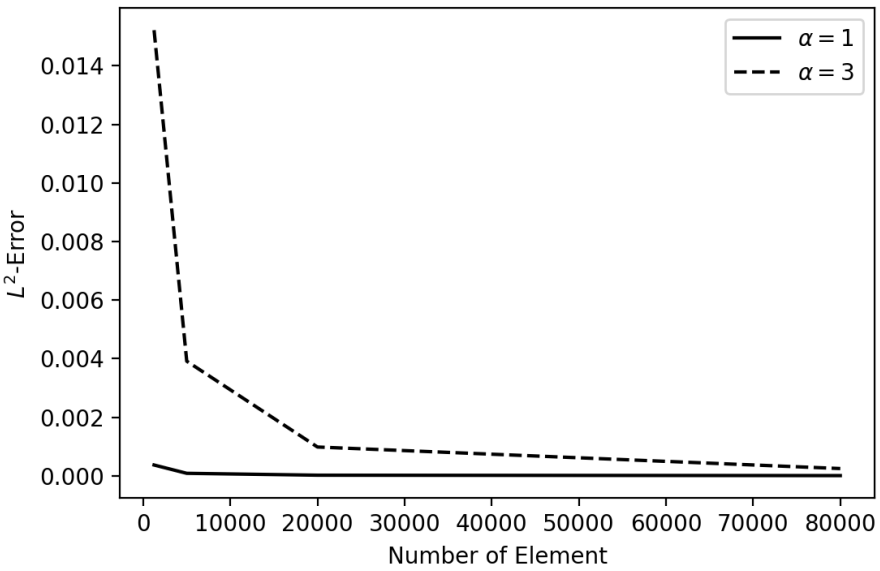

(a) L^2-error vs number of elements

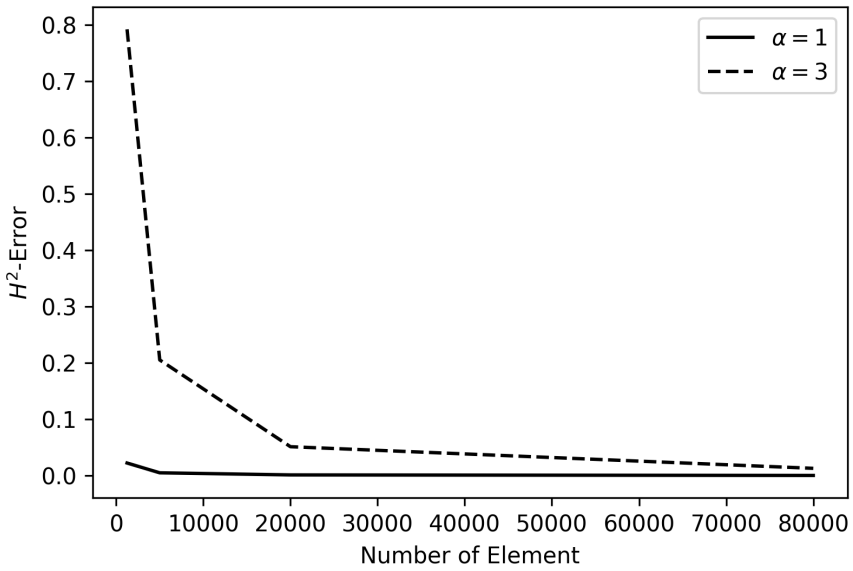

(b) H^1-error vs number of elements

Figure 2.3: L^2-error and H^1-error for different α values and mesh sizes

2.1.6.2 Convergence Analysis by Relative Error

In this part, the convergence of solutions for different mesh sizes and different time step values are studied. Random numbers are given as initial conditions. We have to give the same pattern as initial conditions in order to compare concentration, chemical potential, and Ginzburg-Landau Free Energy function. Even if seed is used to give a random number, the same pattern can not be obtained for different mesh sizes since mesh with different mesh sizes has different node numbers. To solve this problem, the initial condition is set for the coarsest mesh, and for the finer meshes, nodal values are obtained from the initial condition of the coarsest mesh. After that, empty nodal values in the finer meshes are interpolated. Initial conditions for different mesh sizes are shown in Figure 2.4

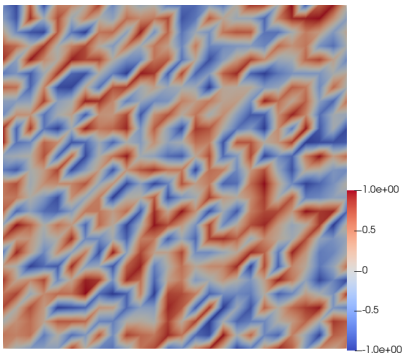

(a) Initial condition for $h = 1/25$

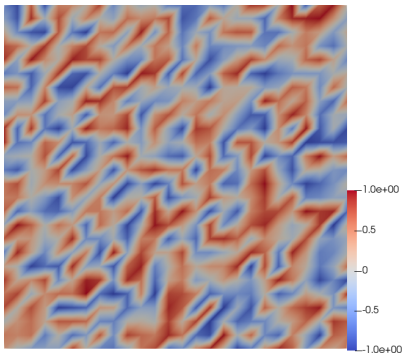

(b) Initial condition for $h = 1/50$

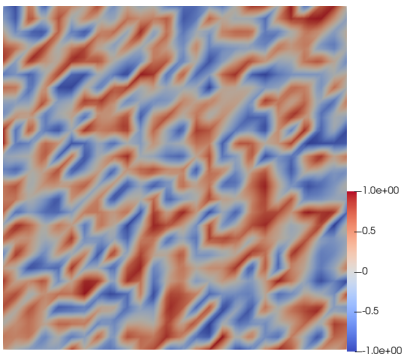

(c) Initial condition for $h = 1/80$

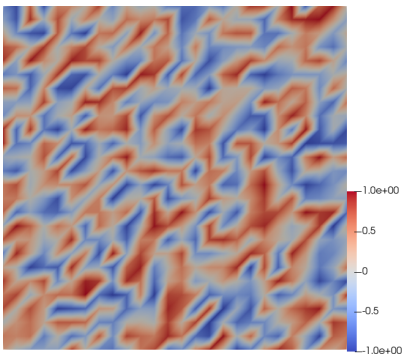

(d) Initial condition for $h = 1/100$

Figure 2.4: Finer meshes have the same pattern as the initial condition of the coarsest mesh. Four uniform meshes ($50 \times 25 = 1250$, $100 \times 50 = 5000$, $160 \times 80 = 12800$ and $200 \times 100 = 20000$ T1 elements) are presented

Equation (2.14) is solved for all mesh sizes ($h = 1/25$, $h = 1/50$, $h = 1/80$, $h = 1/100$) for the given parameters in Table 2.2

Table 2.2: The parameters of the mesh convergence analysis example

No.	Parameter	Name	Value
1	$\mathcal{B}$	Domain	$[-0.5, 0.5] \times [-0.5, 0.5]$
2	Δt	Time step	10^{-4}
3	ϵ	Surface parameter	10^{-2}
4	M	Mobility	1
5	$f(c)$	Free energy	$c^4/4 - c^2/2$
6	c_0	Initial concentration	Random number between -1 and 1

The line graph of the concentration, the chemical potential, and the Ginzburg-Landau free energy per unit volume are obtained from the same diagonal line in solution at $t = 0.0025$ for each mesh size. These graphs are presented in Figure 2.6. According to Figure 2.6, $h = 1/50$ is fine enough since solution is nearly the same as the solution of finer meshes. As an example, the diagonal line is depicted in Figure 2.5.

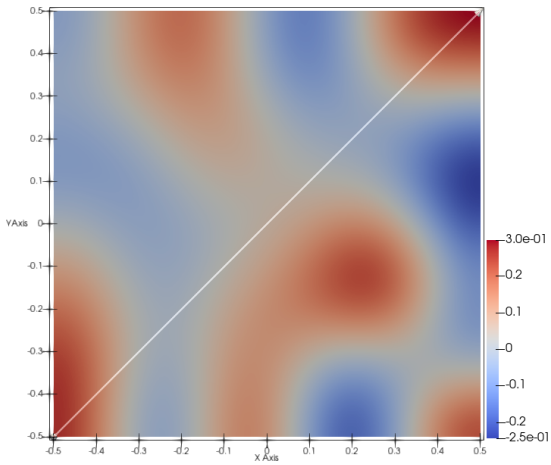

Figure 2.5: Concentration for $h = 1/100$, at $t = 0.0025$

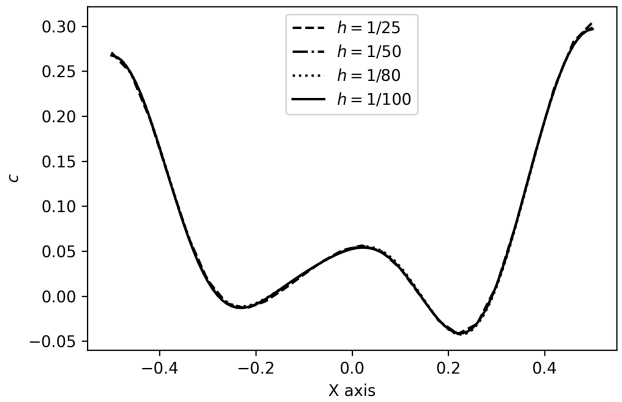

(a) c vs x axis for different mesh sizes

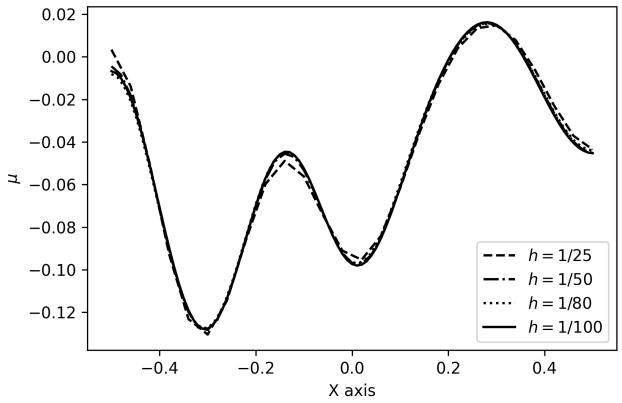

(b) μ vs x axis for different mesh sizes

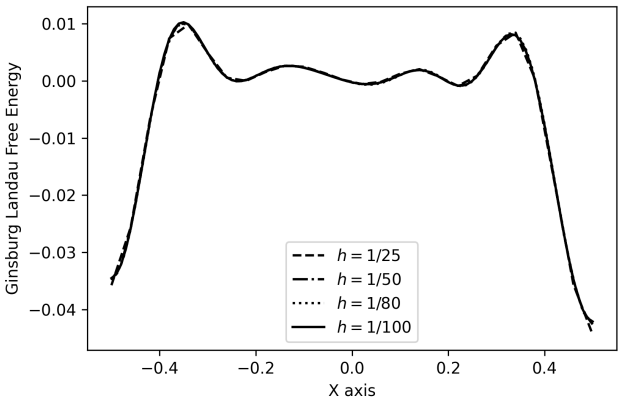

(c) Ginzburg-Landau free energy vs x axis for different mesh sizes

Figure 2.6: Convergence analysis for different mesh sizes

Now, we will solve same problem with given parameters in Table 2.3 but now for different time step values ($\Delta t = 1 \times 10^{-3}$, $\Delta t = 5 \times 10^{-4}$, $\Delta t = 1 \times 10^{-4}$). The line graphs of the concentration, the chemical potential and the Ginzburg-Landau free energy per unit volume are obtained from the same diagonal line which is from point $(-0.5, -0.5)$ to point $(0.5, 0.5)$ at $t = 0.025$ for different time steps. These line graphs can be seen in Figure 2.7.

According to Figure 2.7, it can be stated that $\Delta t = 1 \times 10^{-3}$ is good enough to solve the Cahn-Hilliard equation for the given parameters in Table 2.3.

Table 2.3: The parameters of the time step convergence analysis example

No.	Parameter	Name	Value
1	$\mathcal{B}$	Domain	$[-0.5, 0.5] \times [-0.5, 0.5]$
2	h	Mesh size	10^{-2}
3	ϵ	Surface parameter	10^{-2}
4	M	Mobility	1
5	$f(c)$	Free energy	$c^4/4 - c^2/2$
6	c_0	Initial concentration	Random values between -1 and 1

In Figure 2.8, Ginzburg-Landau free energy function ($\int_{\mathcal{B}} \left(\frac{\epsilon}{2}|\nabla_{\boldsymbol{x}} c|^2 + f(c)\right) dV$) values are plotted. The free energy function values decrease throughout the time since solution of the Cahn-Hilliard equation is minimization of the Ginzburg-Landau free energy function. In Figure 2.8a, Ginzburg-Landau free energy function values are same for different mesh sizes at $t = 0$. Similarly, in Figure 2.8b, Ginzburg-Landau free energy function values are same for different time steps at $t = 0$

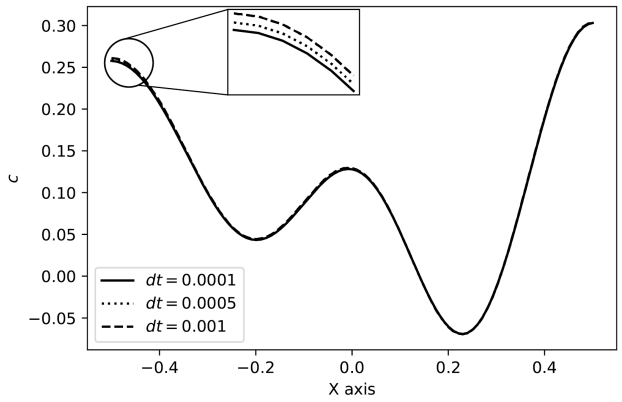

(a) c vs x axis for different time steps

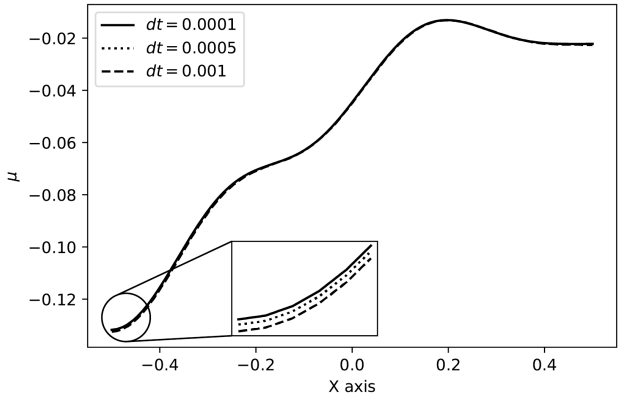

(b) μ vs x axis for different time steps

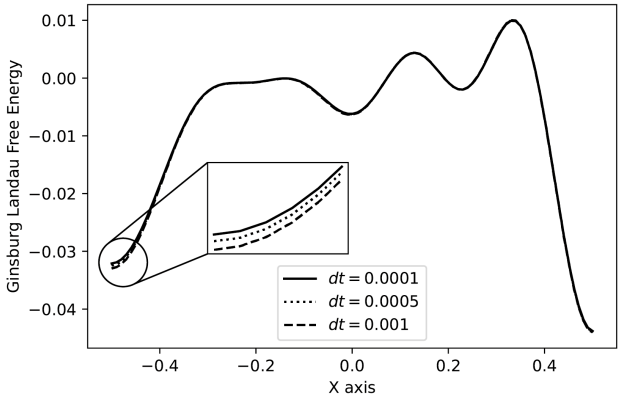

(c) Ginzburg-Landau Free Energy vs x axis for different time steps

Figure 2.7: Convergence analysis for different time steps

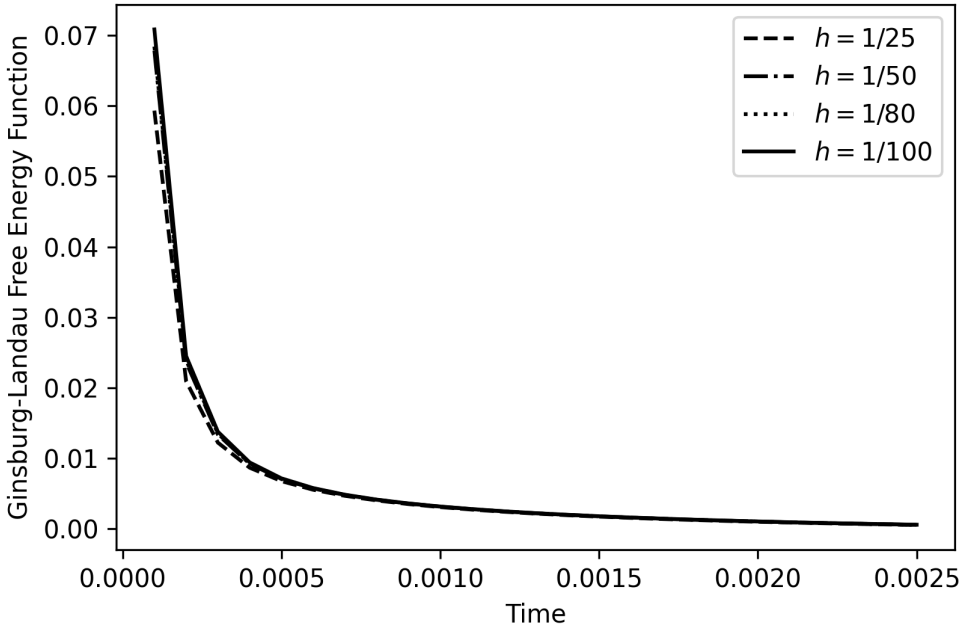

(a) For different mesh sizes

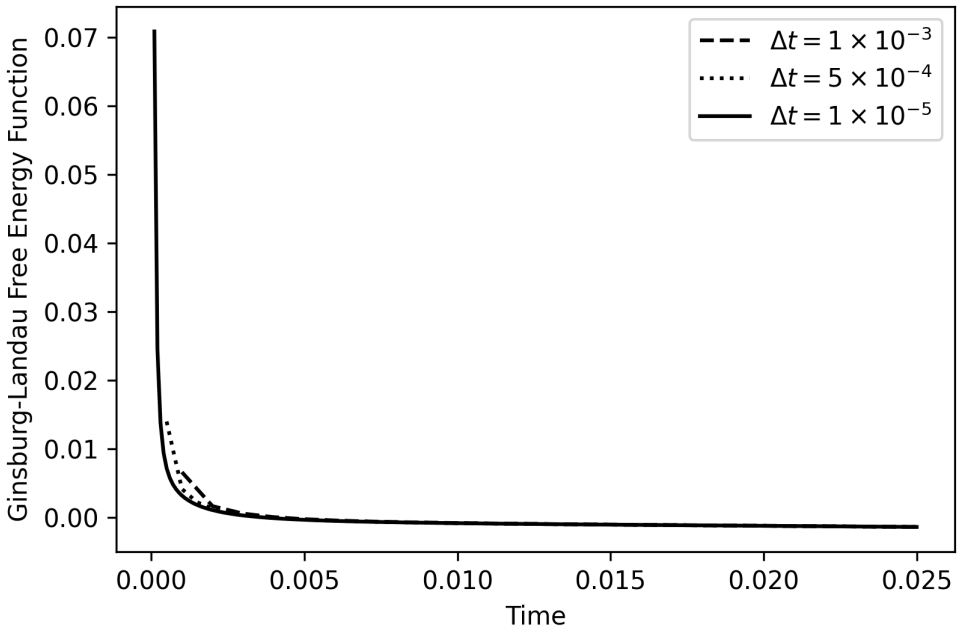

(b) For different time steps

Figure 2.8: Ginzburg-Landau free energy function values throughout the time

2.1.7 Numerical Examples

In the numerical examples, we assumed isotropic behavior through the scalar mobility parameter M to simplify the equation. Mobility tensor can be represented by multiplication of scalar value with identity tensor. Furthermore, in the literature, mobility is usually stated as a scalar number.

2.1.7.1 Cahn-Hilliard Equation with Different Free Energy Density Functions

In this part, we solve the Cahn-Hilliard problem with given parameters in Table 2.4 for different free energy densities. In other words, everything is the same except for the free energy densities. The initial condition is presented in Figure 2.9 for all cases. The free energy densities are shown in Figure 2.10.

$$\begin{aligned} \frac{\partial c}{\partial t} - \operatorname{div}(M \nabla_{\boldsymbol{x}} \mu) &= 0 \quad && \text{in } \mathcal{B} \\ \mu + f'(c) - \epsilon \nabla_{\boldsymbol{x}}^2 c &= 0 \quad && \text{in } \mathcal{B} \\ \nabla_{\boldsymbol{x}} \mu \cdot n &= 0 \quad && \text{on } \partial\mathcal{B}, \\ \nabla_{\boldsymbol{x}} c \cdot n &= 0 \quad && \text{on } \partial\mathcal{B}. \\ c &= c_0 \quad && \text{in } \mathcal{B} \text{ at } t = 0 \end{aligned} \tag{2.82}$$

Table 2.4: Parameters of the Cahn-Hilliard equation for different free energy densities

No.	Parameter	Name	Value
1	$\mathcal{B}$	Domain	$[0,1] \times [0,1]$
2	h	Mesh size	10^{-2}
3	ϵ	Surface parameter	10^{-2}
4	M	Mobility	1
5	Δt	Time step	5×10^{-4}
6	c_0	Initial concentration	Random values between -1 and 1

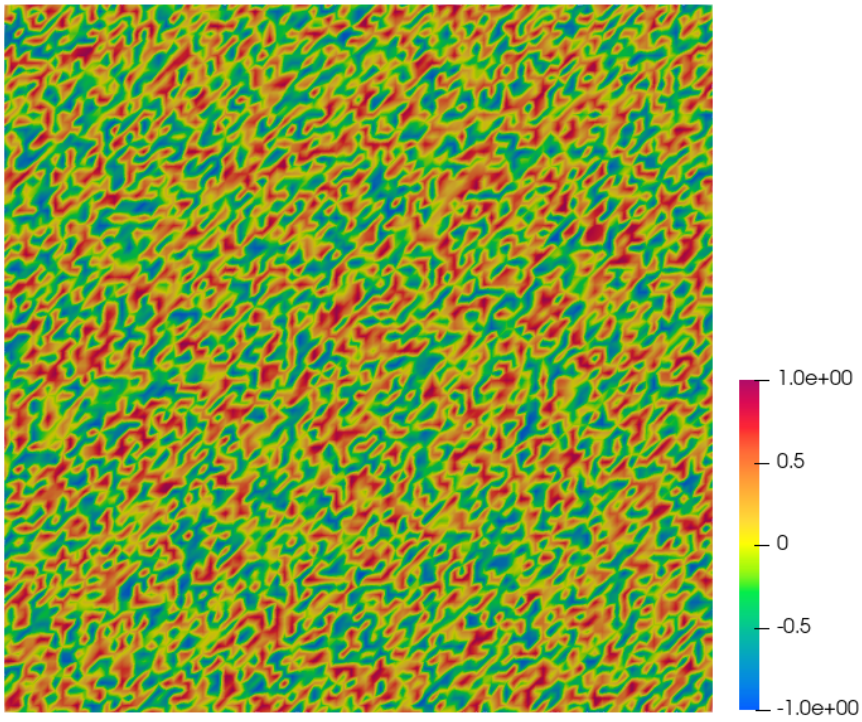

Figure 2.9: Initial condition is the same for all cases with different free energy densities. The color indicates the value of the concentration field.

Five different free energy density function functions are used. These are shown in Figure 2.10. The functions in Figures 2.10a, 2.10b, 2.10c, and 2.10e are double-well potential. In other words, those have two local minimums in the range of interest, which is $[-1, 1]$. The double-well potential will lead to a pattern formation. One phase will occur around the first minimum point, and the other phase will occur around the second minimum point.

The function in Figure 2.10d has only one minimum point. Therefore, we will not observe any two-phase pattern formation.

With this study, we will see whether the pattern changes or not with the free energy density function. In Figure 2.10a, the free energy function has symmetry. The energies in Figure 2.10b and 2.10c are not symmetric and one of the minimum point has a lower value. The free energy function in Figure 2.10e, is not symmetric, and the local maximum point is slightly shifted towards $c = 1$ axis. In all energy functions, we expect different patterns at the final time since the derivatives of energy functions are

different, and they play a role in pattern evolution. The solutions of the Cahn-Hilliard problem are depicted in Figures 2.11 - 2.15 at different times.

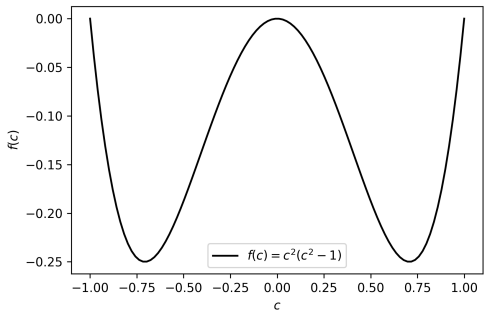

(a) $f(c) = c^2(c^2 - 1)$

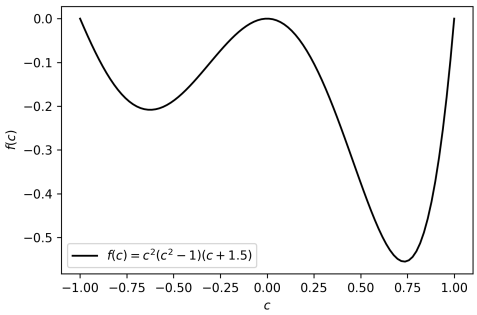

(b) $f(c) = c^2(c^2 - 1)(c + 1.5)$

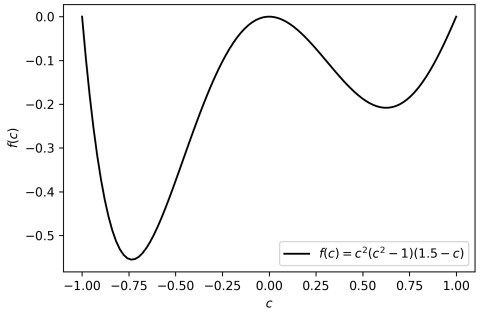

(c) $f(c) = c^2(c^2 - 1)(1.5 - c)$

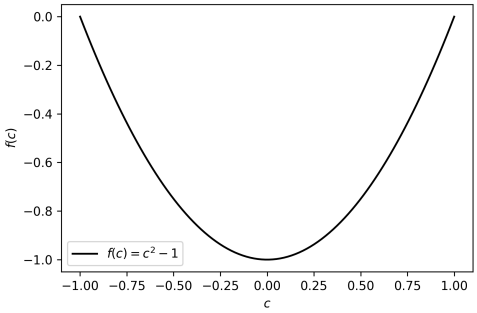

(d) $f(c) = c^2 - 1$

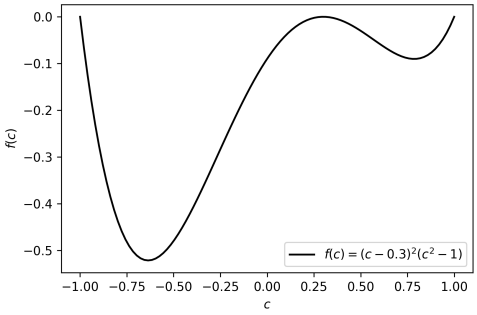

(e) $f(c) = (c - 0.3)^2(c^2 - 1)$

Figure 2.10: Different free energy function functions for the CH problem

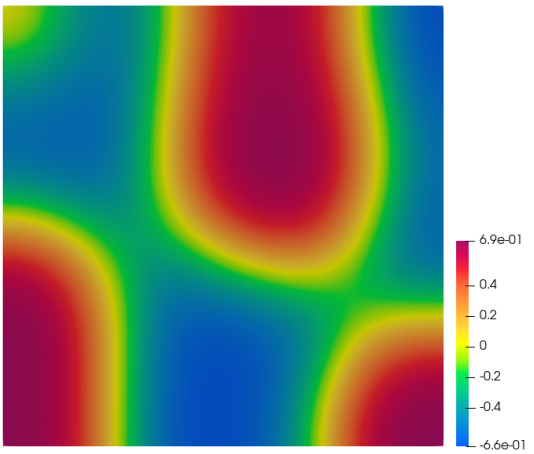

(a) Concentration for $f(c) = c^2(c^2 - 1)$

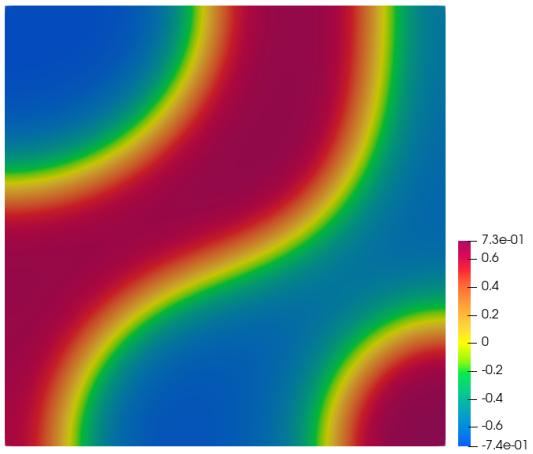

(b) Concentration for $f(c) = c^2(c^2 - 1)(c + 1.5)$

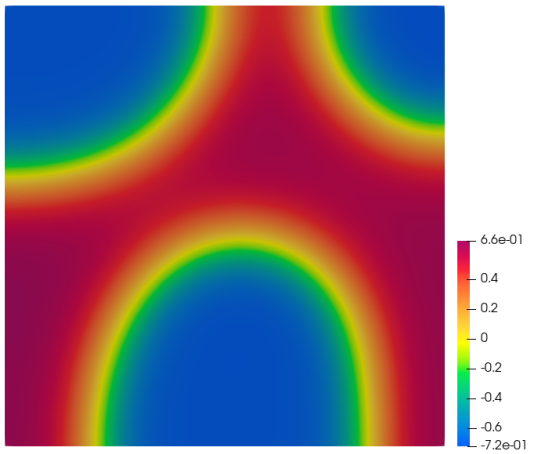

(c) Concentration for $f(c) = c^2(c^2 - 1)(1.5 - c)$

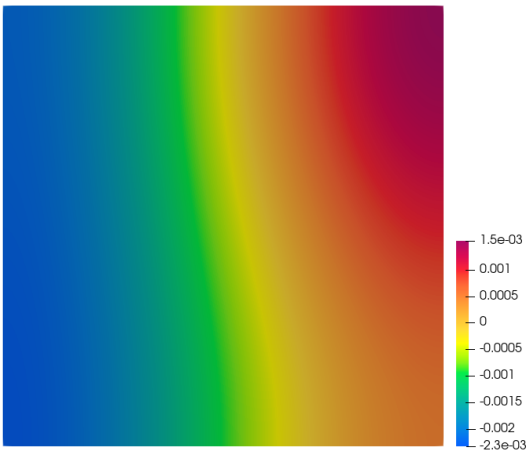

(d) Concentration for $f(c) = c^2 - 1$

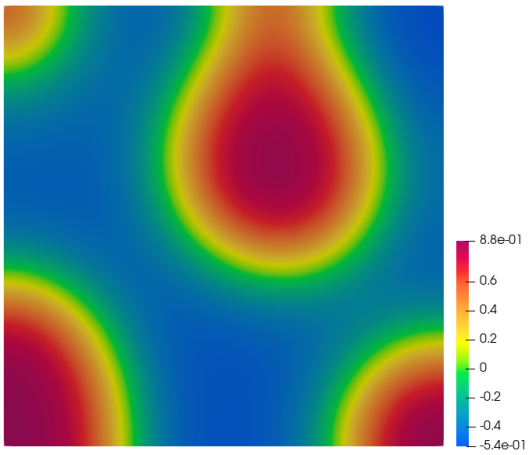

(e) Concentration for $f(c) = (c - 0.3)^2(c^2 - 1)$

Figure 2.11: Solutions of CH problem at $t = 0.1$. The color indicates the value of the concentration field.

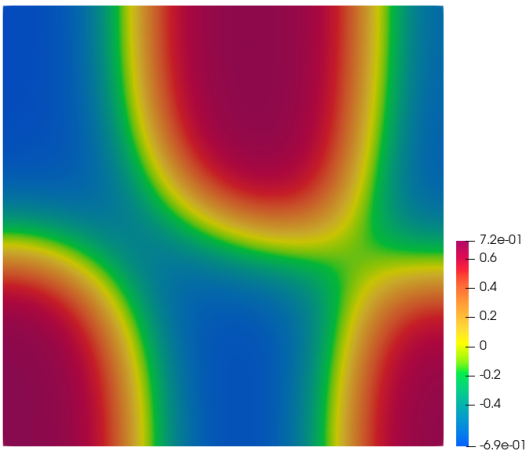

(a) Concentration for $f(c) = c^2(c^2 - 1)$

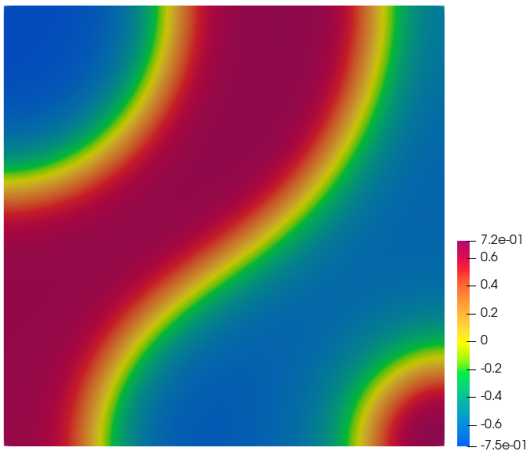

(b) Concentration for $f(c) = c^2(c^2 - 1)(c + 1.5)$

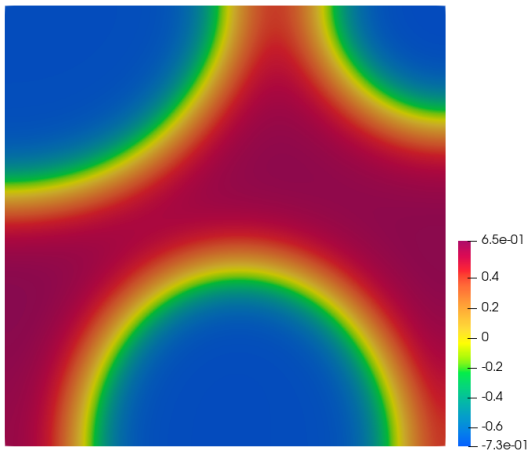

(c) Concentration for $f(c) = c^2(c^2 - 1)(1.5 - c)$

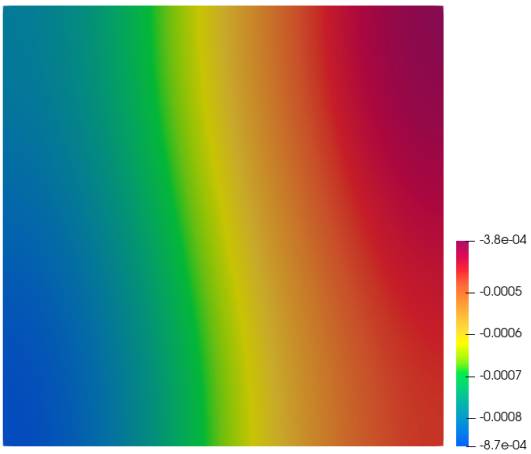

(d) Concentration for $f(c) = c^2 - 1$

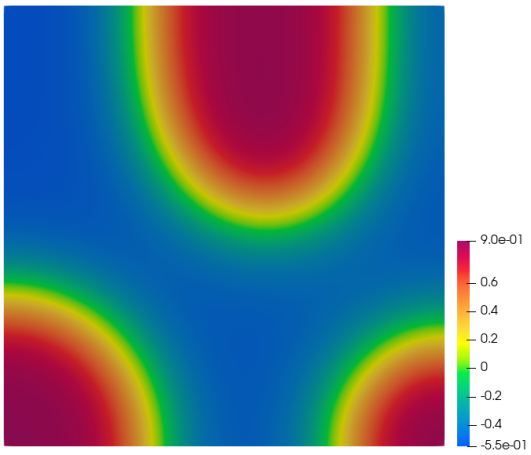

(e) Concentration for $f(c) = (c - 0.3)^2(c^2 - 1)$

Figure 2.12: Solutions of CH problem at $t = 0.2$. The color indicates the value of the concentration field.

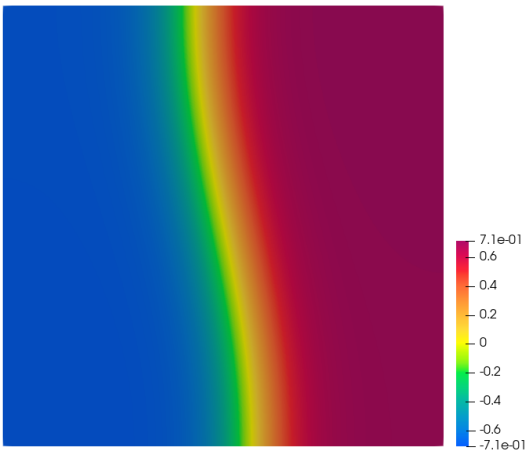

(a) Concentration for $f(c) = c^2(c^2 - 1)$

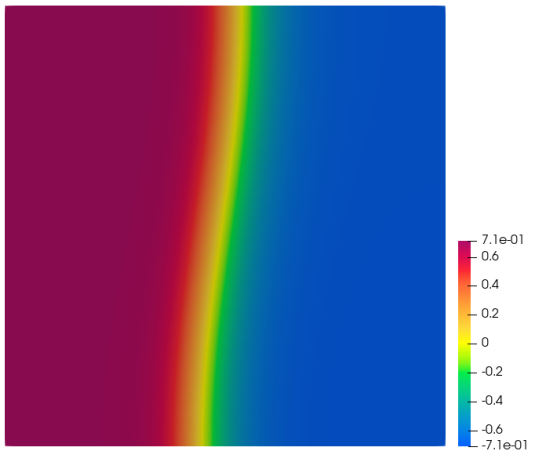

(b) Concentration for $f(c) = c^2(c^2 - 1)(c + 1.5)$

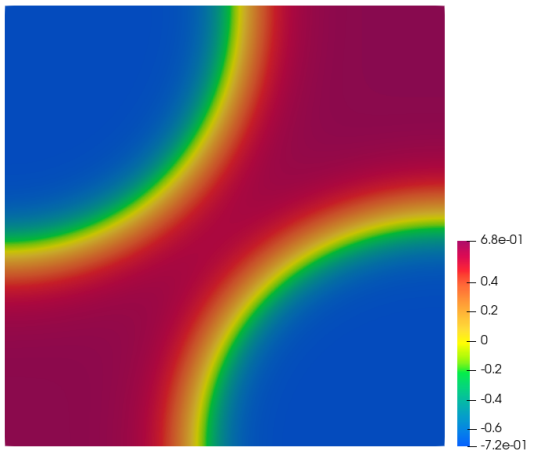

(c) Concentration for $f(c) = c^2(c^2 - 1)(1.5 - c)$

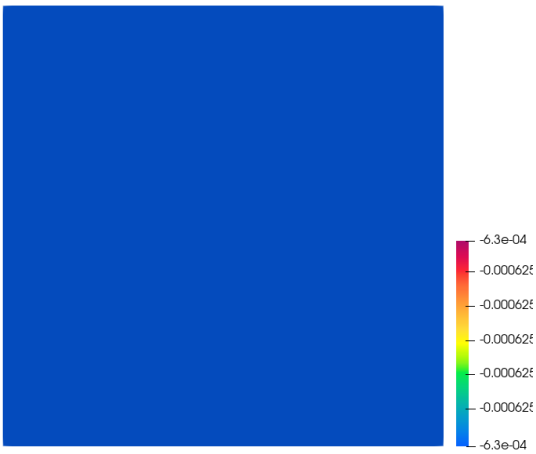

(d) Concentration for $f(c) = c^2 - 1$

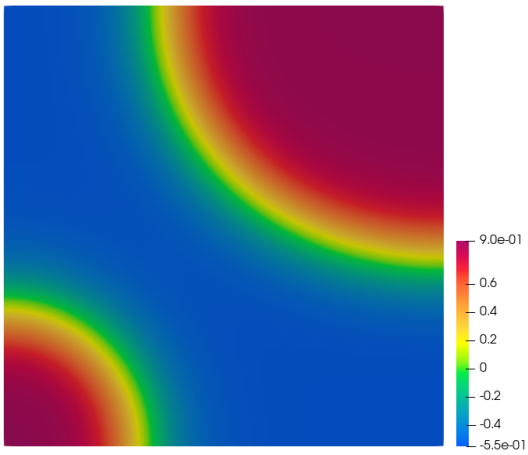

(e) Concentration for $f(c) = (c - 0.3)^2(c^2 - 1)$

Figure 2.13: Solutions of CH problem at $t = 1$. The color indicates the value of the concentration field.

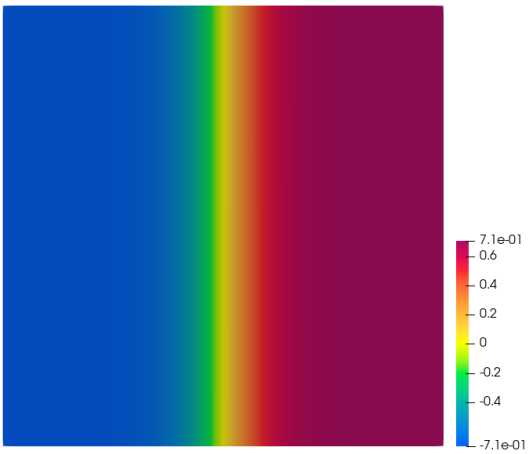

(a) Concentration for $f(c) = c^2(c^2 - 1)$

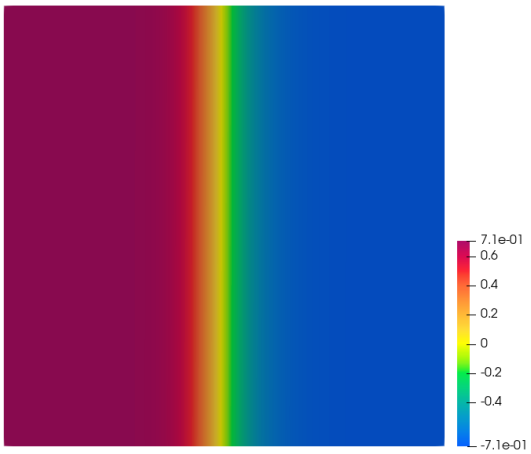

(b) Concentration for $f(c) = c^2(c^2 - 1)(c + 1.5)$

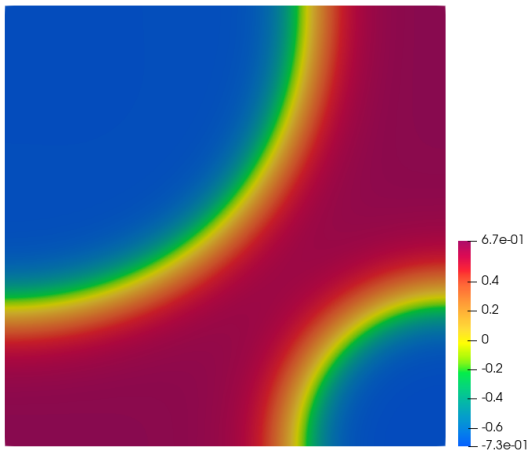

(c) Concentration for $f(c) = c^2(c^2 - 1)(1.5 - c)$

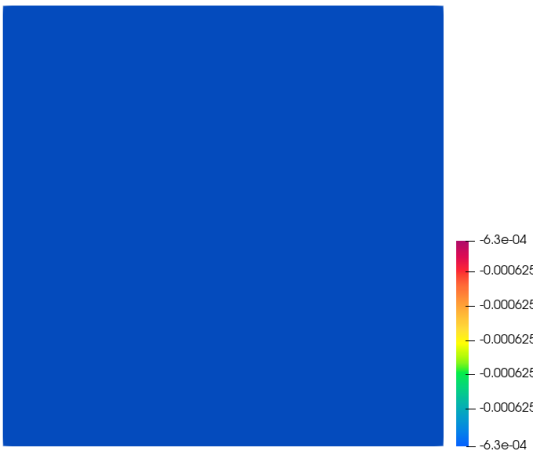

(d) Concentration for $f(c) = c^2 - 1$

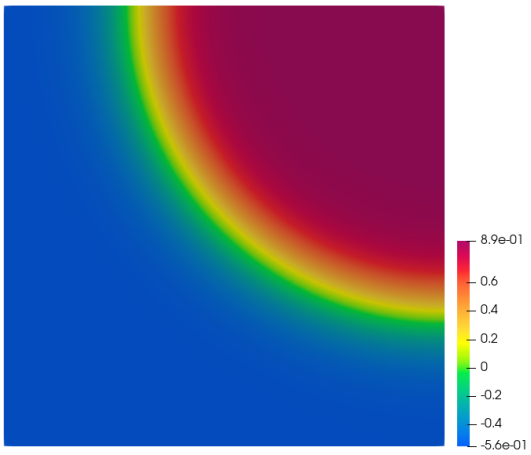

(e) Concentration for $f(c) = (c - 0.3)^2(c^2 - 1)$

Figure 2.14: Solutions of CH problem at $t = 5$. The color indicates the value of the concentration field.

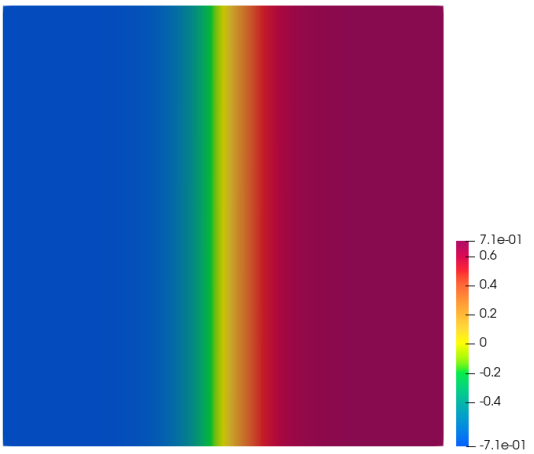

(a) Concentration for $f(c) = c^2(c^2 - 1)$

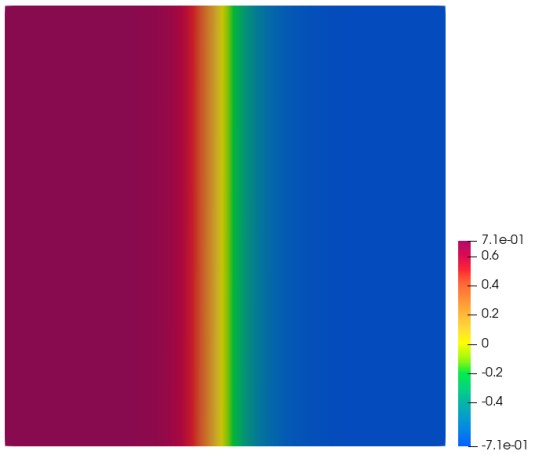

(b) Concentration for $f(c) = c^2(c^2 - 1)(c + 1.5)$

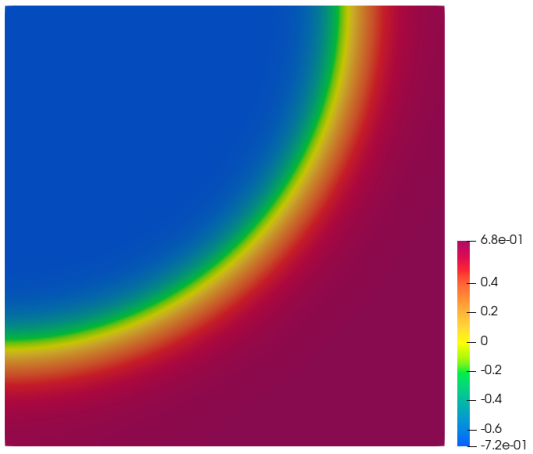

(c) Concentration for $f(c) = c^2(c^2 - 1)(1.5 - c)$

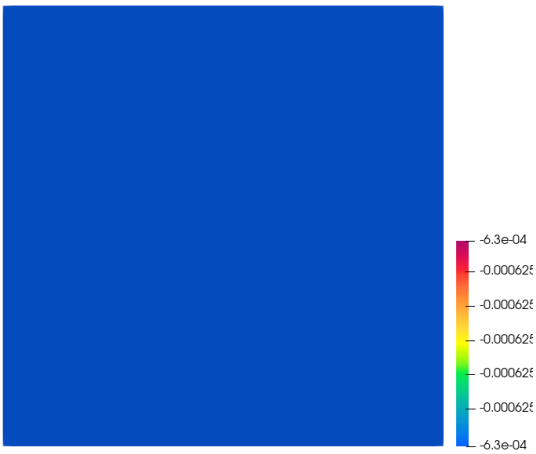

(d) Concentration for $f(c) = c^2 - 1$

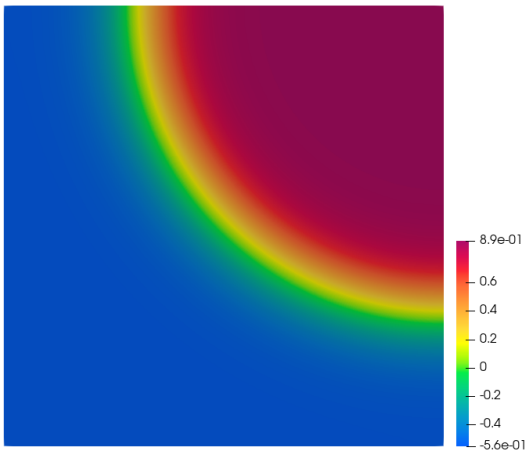

(e) Concentration for $f(c) = (c - 0.3)^2(c^2 - 1)$

Figure 2.15: Solutions of CH problem at $t = 20$. The color indicates the value of the concentration field.

As can be seen from Figure 2.15, we have different pattern formations for different free energy density functions. Initial conditions are approximately the same for all problems in this subsection. Therefore initial condition does not have an effect on the pattern change. For $f(c) = c^2 - 1$, no pattern formation is occurred as expected. For other free energy density functions, we state that the pattern at the final time is not predicted since the behavior of the governing equation is highly nonlinear. All we say is that for free energy in Figure 2.10e, we expect more blue region in Figure 2.15e since local maximum of the free energy density function is not in $c = 0$ axis. It is slightly shifted towards $c = 1$ axis. We have more region between $c = -1$ axis and the local maximum point than between the local maximum point and $c = 1$ axis and random initial condition is given. This leads to more blue region in Figure 2.15e.

2.1.7.2 Allen-Cahn Equation

Two examples of the Allen-Cahn problem and their finite element solutions are presented here.

$$\begin{aligned} c_t - \epsilon^2 \nabla_{\boldsymbol{x}}^2 c + f(c) = 0, \quad (x,t) \in \mathcal{B} \times (0,T] \\ \nabla_{\boldsymbol{x}} c \cdot \mathbf{n} = 0 \\ c(\boldsymbol{x}, 0) = c_0 \end{aligned} \tag{2.83}$$

Weak Form:

$$\int_{\mathcal{B}} c_t v dV + \int_{\mathcal{B}} \epsilon^2 \nabla_{\boldsymbol{x}} c \cdot \nabla_{\boldsymbol{x}} v dV + \int_{\mathcal{B}} f(c) v dV = 0, \quad v \in V \tag{2.84}$$

where

$$f(c) = c^3 - c \tag{2.85}$$

The model parameters used to generate the results in Figure 2.16 illustrated are given in Table 2.5.

Table 2.5: Parameters of Allen-Cahn model 1D problem

No.	Parameter	Name	Value
1	$\mathcal{B}$	Domain	$[-1, 1]$
2	ϵ	Surface parameter	10^{-2}
3	Δt	Time step	5×10^{-5}
4	c_0	Initial concentration	$0.1\cos(2\pi x)$

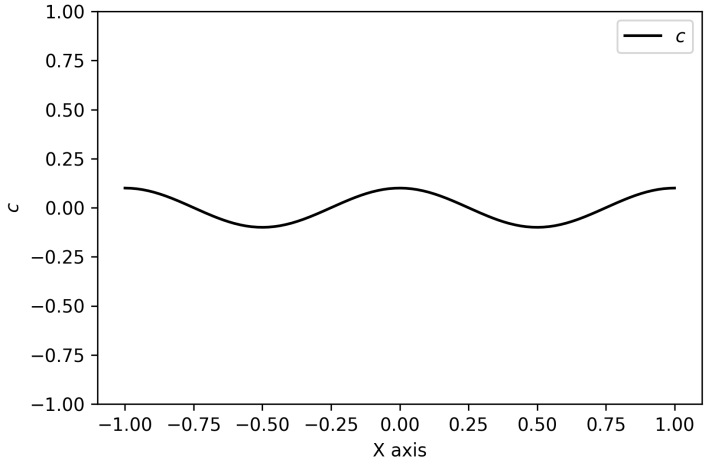

(a) c at $t = 0$

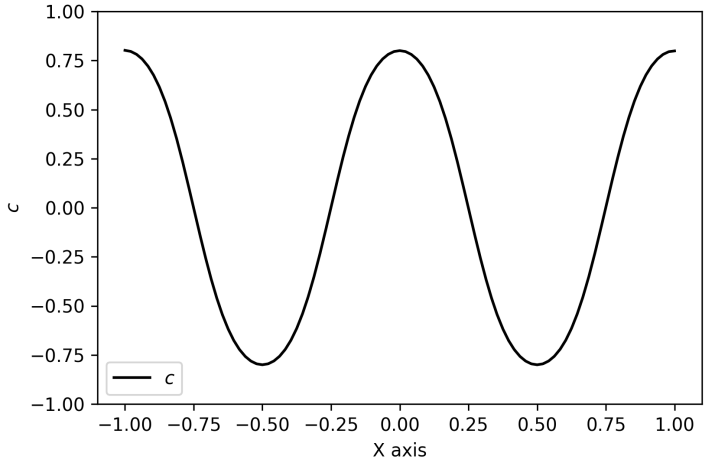

(b) c at $t = 5$

Figure 2.16: Solution of the first Allen-Cahn problem

The model parameters of the second example for Allen-Cahn equation are given in Table 2.6. Initial condition and solutions are shown in Figure 2.17 and Figure 2.18 respectively.

Table 2.6: Parameters of Allen-Cahn model 2D problem

No.	Parameter	Name	Value
1	$\mathcal{B}$	Domain	$[-1,1] \times [-1,1]$
2	ϵ	Surface parameter	10^{-2}
3	Δt	Time step	5×10^{-5}
4	c_0	Initial concentration	$0.1\cos(2\pi x)\cos(2\pi y)$

From the computational experiments of the Allen-Cahn problem, we observe that c increases for the region $c_0 > 0$ and c decreases for the region $c_0 < 0$. These observation can be seen from Figures 2.16 and 2.18.

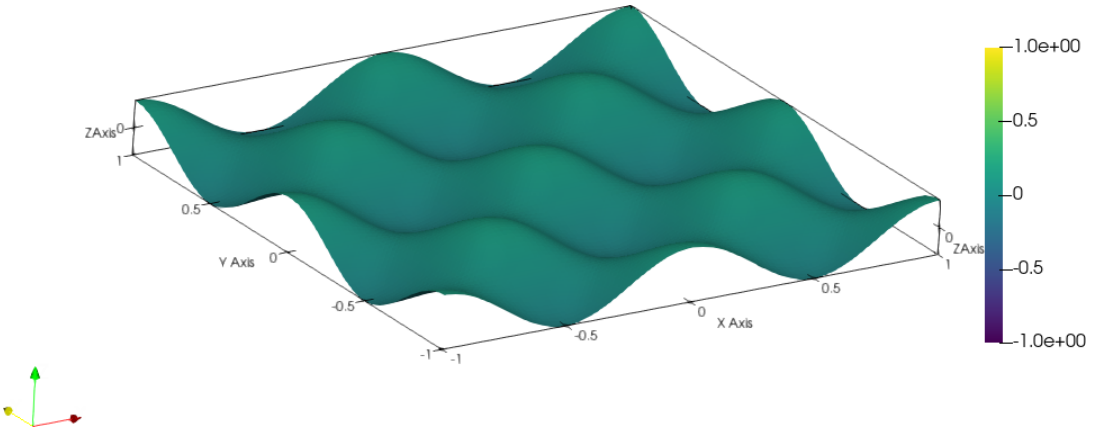

Figure 2.17: Initial concentration, c_0

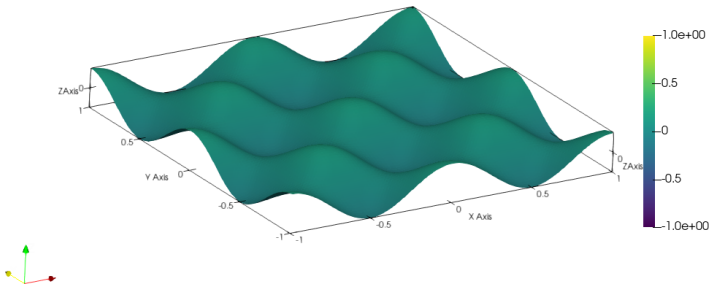

(a) Concentration at t = 0.5

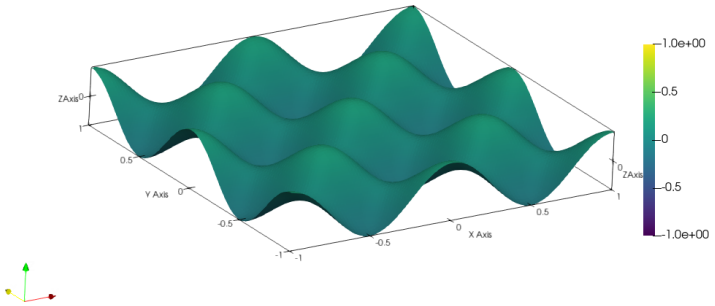

(b) Concentration at t = 2.5

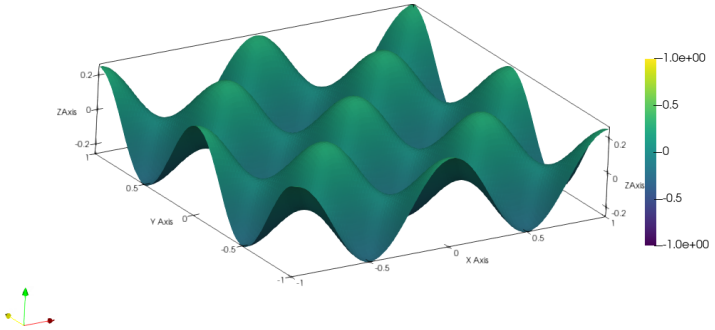

(c) Concentration at t = 5

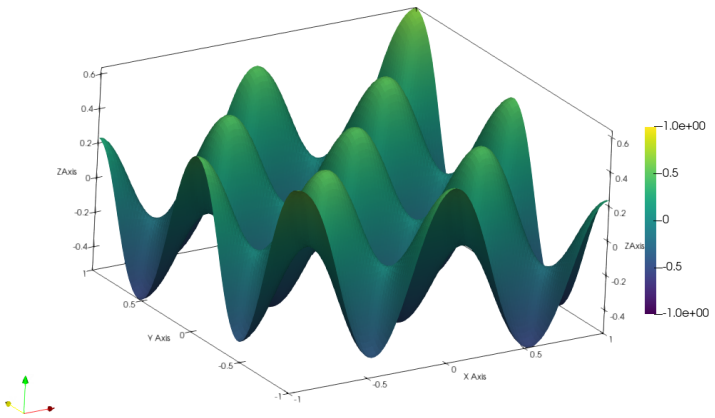

(d) Concentration at t = 10

Figure 2.18: Solution of the second Allen-Cahn problem. The color indicates the value of the concentration field.

2.1.7.3 Cahn-Hilliard Equation

In this part, we will solve Equation (2.17) using $\mathbf{C}_0$ and $\mathbf{C}_2$ elements. For both solutions, the parameters in Table 2.7 are used.

Table 2.7: Parameters of $\mathbf{C}_0$ and $\mathbf{C}_2$ comparison example

No.	Parameter	Name	Value
1	$\mathcal{B}$	Domain	$[0,1] \times [0,1]$
2	ϵ	Surface parameter	1×10^{-2}
3	M	Mobility	1
4	$f(c)$	Free energy	$100c^2(1-c)^2$
5	Δt	Time step	5×10^{-6}
6	c_0	Initial concentration	Random values between 0.61 and 0.65

Solution Obtained by Using $\mathbf{C}_0$ Elements

In the analysis, $200 \times 100 = 20000$ triangular elements (T1) are used. Initial condition is described in Figure 2.19a. The solution is shown in Figure 2.19. We aim to obtain similar results and observe the spinodal decomposition and the Ostwald ripening phenomenon for both solutions.

Weak Form:

$$\begin{aligned} \int_{\mathcal{B}} \frac{\partial c}{\partial t} v dV + \int_{\mathcal{B}} M \nabla_{\boldsymbol{x}} \mu \cdot \nabla_{\boldsymbol{x}} v dV = 0 \quad \forall v \in V_0 \\ \int_{\mathcal{B}} \mu q dV + \int_{\mathcal{B}} f'(c) q dV + \int_{\mathcal{B}} \epsilon \nabla_{\boldsymbol{x}} c \cdot \nabla_{\boldsymbol{x}} q dV = 0 \quad \forall q \in V_0 \\ c = c_0 \text{ in } \mathcal{B} \text{ at } t = 0 \end{aligned} \tag{2.86}$$

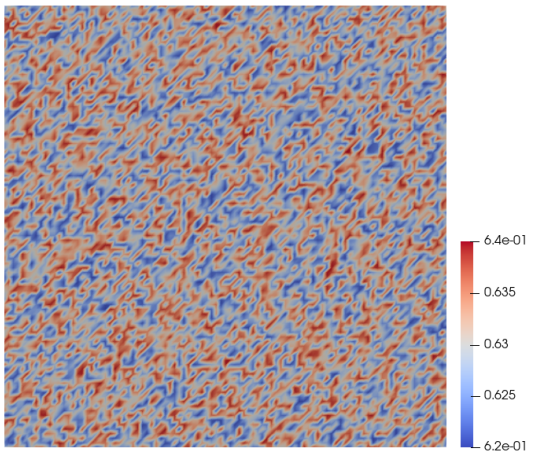

(a) Concentration at t = 0

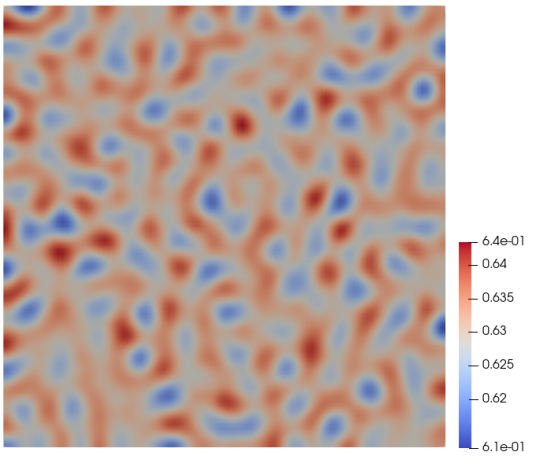

(b) Concentration at t = 0.00001

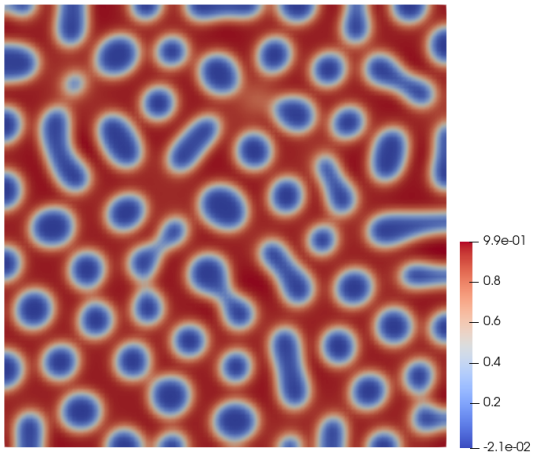

(c) Concentration at t = 0.0001

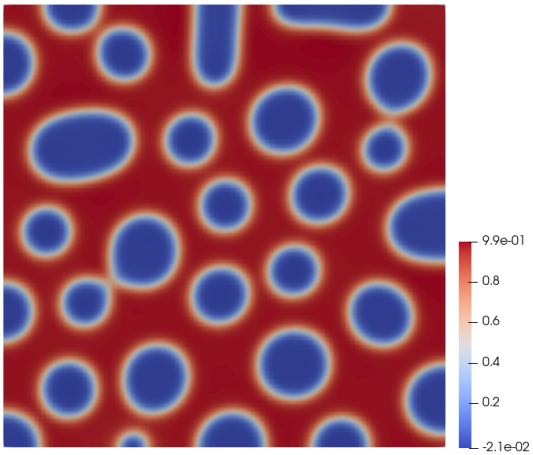

(d) Concentration at t = 0.0005

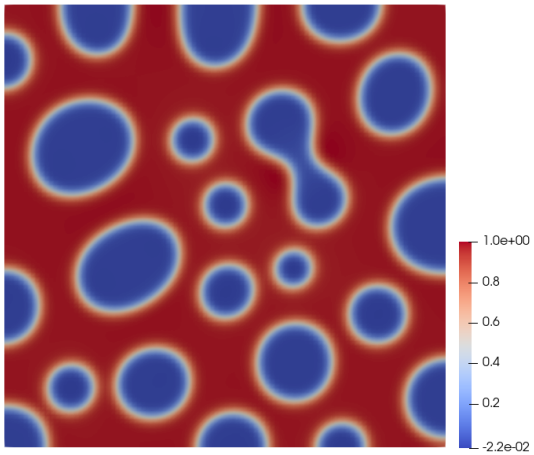

(e) Concentration at t = 0.001

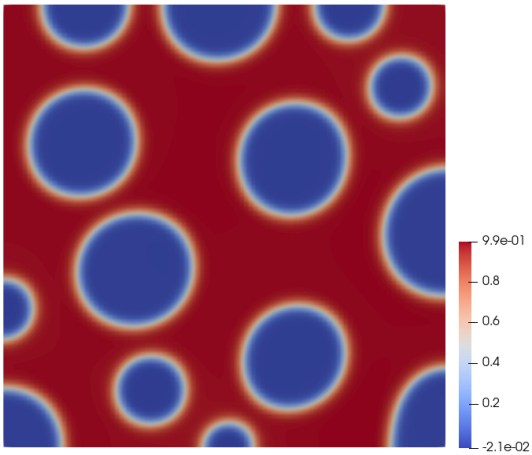

(f) Concentration at t = 0.0025

Figure 2.19: Solutions of CH problem using $\mathbf{C}_0$ elements

Solution Obtained by Using $\mathbf{C}_2$ Elements

Firedrake is used in order to solve this problem. Like FEniCS, Firedrake is a open-source computing platform for solving partial differential equations (PDEs) using the finite element method [61]. $32 \times 16 = 512$ triangular Bell elements are used. The Bell element has first and second derivative continuity at the nodes and it is depicted in Figure 2.20 [62]. The dots indicate that the nodal values are continuous, while the small and big hollow circles indicate that the first and second derivatives are continuous respectively in Figure 2.20. Initial condition is depicted in Figure 2.21a. The solution is shown in Figure 2.21.

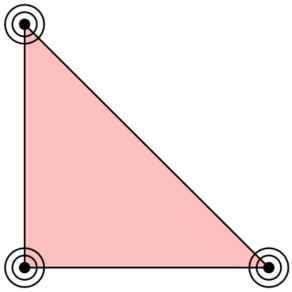

Figure 2.20: The Bell element

The same problem is solved using $\mathbf{C}_0$ and $\mathbf{C}_2$ elements. According to Figure 2.19 and Figure 2.21, similar solutions are obtained. Different initial conditions are used since it is challenging to use the same initial condition for FEniCS and Firedrake for different mesh sizes. Due to the different initial conditions used, differences in the patterns of the solutions occur. We obtained approximately twice speedup when using $\mathbf{C}_2$ elements. On the same virtual machine, to obtain FEM solutions using $\mathbf{C}_0$ and $\mathbf{C}_2$ elements took 305.1 and 150.4 seconds, respectively.

In Figure 2.19b and 2.21b, spinodal decomposition occurs. The spinodal decomposition phenomenon is that two phases start to occur from one phase due to fluctuations in the system to reduce the system's free energy. In Figures 2.19c - 2.19f and Figures 2.21c - 2.21f, the Ostwald ripening phenomenon is being observed. The phenomenon of merging of small phases to form a larger phase is called the Ostwald ripening. In the lithium-ion battery electrode and liquid crystal phase separation, we observe the Ostwald ripening phenomenon [63].

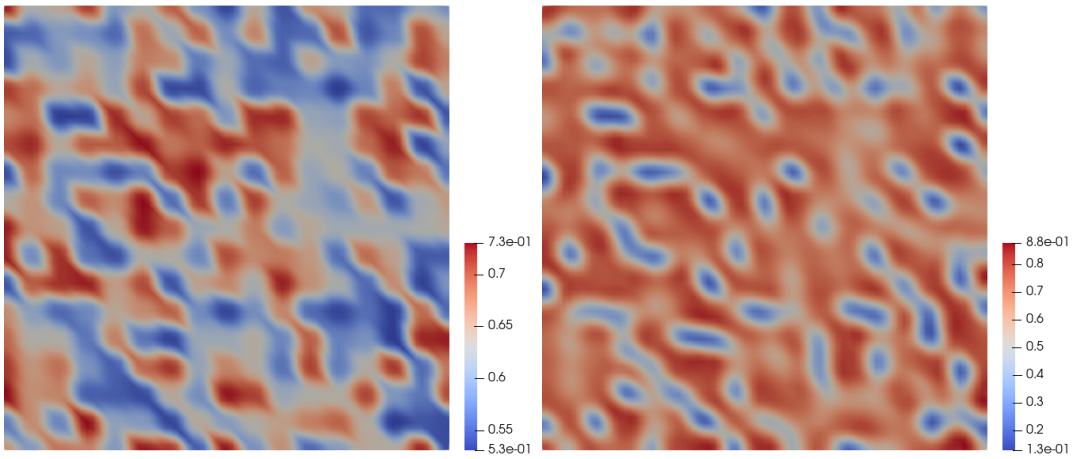

(a) Concentration at t = 0

(b) Concentration at t = 0.00001

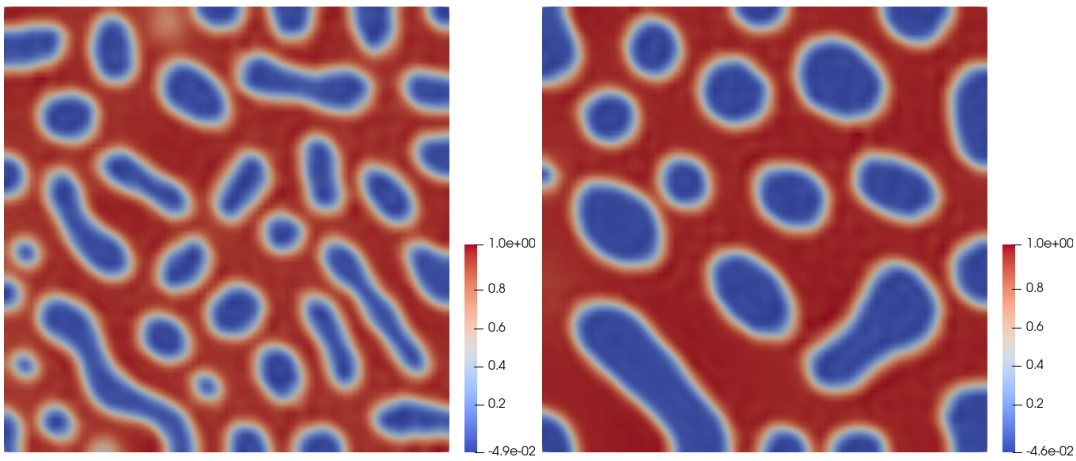

(c) Concentration at t = 0.0001

(d) Concentration at t = 0.0005

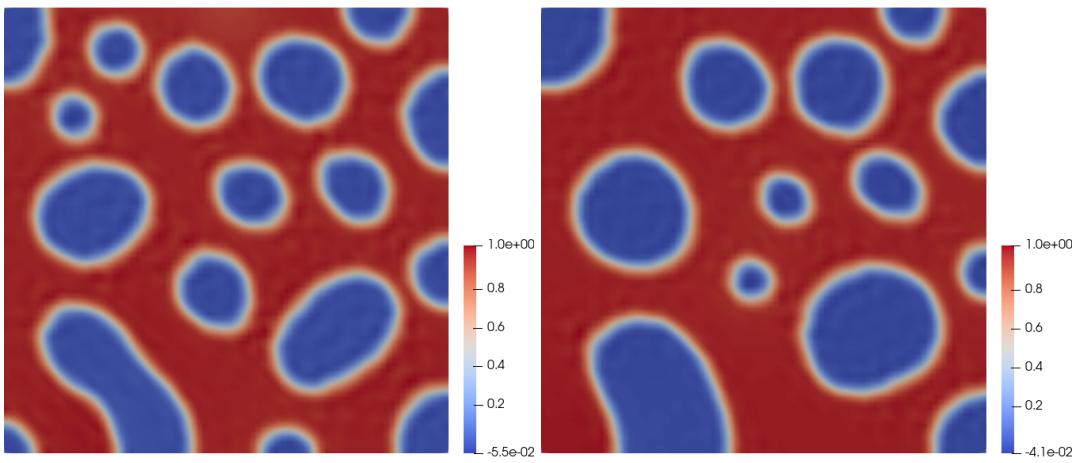

(e) Concentration at t = 0.001

(f) Concentration at t = 0.0025

Figure 2.21: Solutions of CH problem using $\mathbf{C}_2$ elements. The color indicates the value of the concentration field.

2.1.7.4 Generalized Cahn-Hilliard Equation

In this subsection, the sixth-order Cahn-Hilliard equation is solved using the finite element method. It is generally used for an anisotropic Cahn-Hilliard model. Two phase-field crystal examples are reproduced from [58].

$$\begin{aligned} \frac{\partial u}{\partial t} + \nabla_{\boldsymbol{x}}^2 w + \frac{1}{\varepsilon} g(x,u) = 0 \\ w + a_{20}\varepsilon \frac{\partial^4 u}{\partial x^4} + a_{02}\varepsilon \frac{\partial^4 u}{\partial y^4} + a_{11}\varepsilon \frac{\partial^4 u}{\partial x^2 \partial y^2} \\ -a_{10}\varepsilon \frac{\partial^2 u}{\partial x^2} - a_{01}\varepsilon \frac{\partial^2 u}{\partial y^2} + \frac{1}{\varepsilon} f(u) = 0 \\ u(0,x,y) = u_0(x,y) \end{aligned} \tag{2.87}$$

Weak Form:

$$\begin{aligned} \left(\left(\frac{\partial u}{\partial t}, v_1 \right) \right) - \left((\nabla_{\boldsymbol{x}} w, \nabla_{\boldsymbol{x}} v_1) \right) + \frac{1}{\varepsilon} \left((g(x,u), v_1) \right) = 0 \\ \left((w, v_2) \right) - a_{20}\varepsilon \left(\left(\frac{\partial p}{\partial x}, \frac{\partial v_2}{\partial x} \right) \right) - a_{02}\varepsilon \left(\left(\frac{\partial q}{\partial y}, \frac{\partial v_2}{\partial y} \right) \right) \\ -\frac{a_{11}\varepsilon}{2} \left(\left(\frac{\partial p}{\partial y'}, \frac{\partial v_2}{\partial y} \right) \right) - \frac{a_{11}\varepsilon}{2} \left(\left(\frac{\partial q}{\partial x}, \frac{\partial v_2}{\partial x} \right) \right) \\ -a_{10}\varepsilon \left((p, v_2) \right) - a_{01}\varepsilon \left((q, v_2) \right) + \frac{1}{\varepsilon} \left((f(u), v_2) \right) = 0 \\ \left((p, v_3) \right) + \left(\left(\frac{\partial u}{\partial x}, \frac{\partial v_3}{\partial x} \right) \right) = 0 \\ \left((q, v_4) \right) + \left(\left(\frac{\partial u}{\partial y}, \frac{\partial v_4}{\partial y} \right) \right) = 0 \end{aligned} \tag{2.88}$$

where

$$\begin{aligned} \frac{\partial^2 u}{\partial x^2} = p, \\ \frac{\partial^2 u}{\partial y^2} = q, \\ \frac{\partial^4 u}{\partial x^2 \partial y^2} = \frac{1}{2}\frac{\partial^2 p}{\partial y^2} + \frac{1}{2}\frac{\partial^2 q}{\partial x^2} \end{aligned} \tag{2.89}$$

Phase-Field Crystal Example 1:

Parameters of the phase-field crystal example 1 are in Table 2.8

Table 2.8: Parameters of phase-field crystal example 1

No.	Parameter	Name	Value
1	$\mathcal{B}$	Domain	$[-10, 10] \times [-10, 10]$
2	$f(u)$	Free energy	$u^3 + (1 - 0.025)u$
3	$g(x, u)$	Mobility	$2u$
4	Δt	Time step	1×10^{-4}
5	u_0	Initial concentration	Randomly distributed between -0.2 and 0.3
6	a_{20}	Coefficient	1
7	a_{11}	Coefficient	0.1
8	a_{02}	Coefficient	0.1
9	a_{10}	Coefficient	-2
10	a_{01}	Coefficient	-2

Phase-Field Crystal Example 2:

Parameters of the phase-field crystal example 2 are in Table 2.9

Table 2.9: Parameters of phase-field crystal example 2

No.	Parameter	Name	Value
1	$\mathcal{B}$	Domain	$[-10, 10] \times [-10, 10]$
2	$f(u)$	Free energy	$u^3 + (1 - 0.025)u$
3	$g(x, u)$	Mobility	$2u$
4	Δt	Time step	1×10^{-4}
5	u_0	Initial concentration	Randomly distributed between -0.2 and 0.3
6	a_{20}	Coefficient	0.1
7	a_{11}	Coefficient	0.1
8	a_{02}	Coefficient	1
9	a_{10}	Coefficient	-2
10	a_{01}	Coefficient	-2

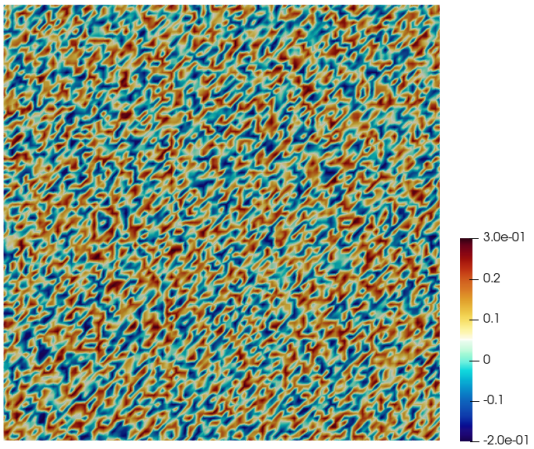

(a) u_0

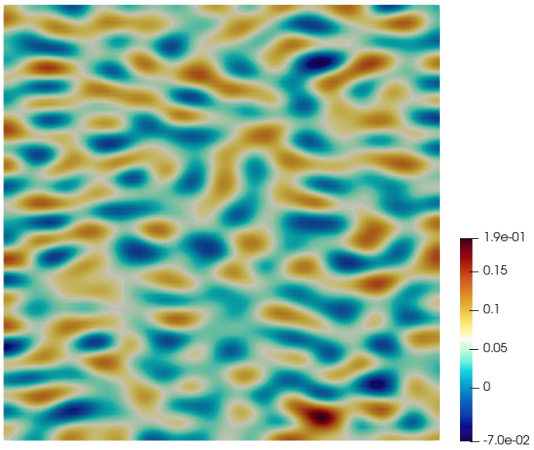

(b) u at t = 0.002

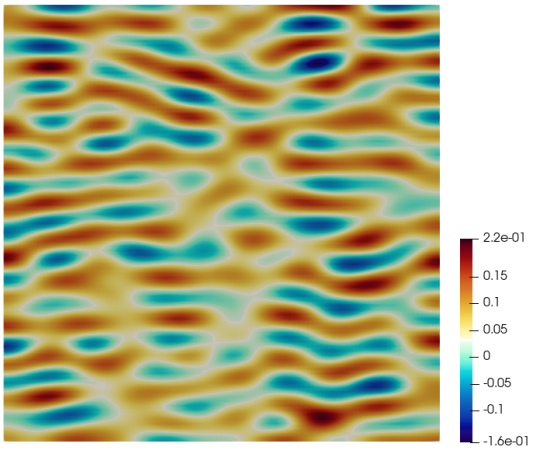

(c) u at t = 0.01

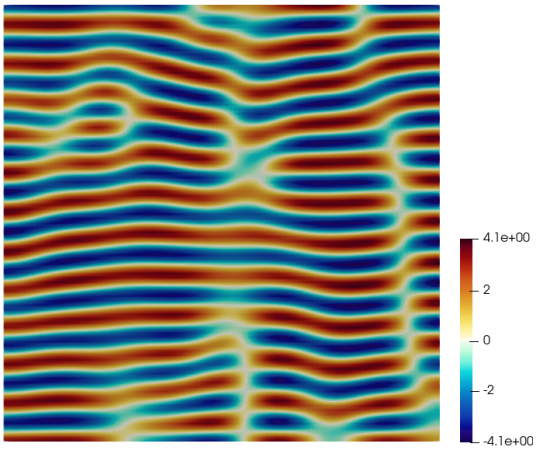

(d) u at t = 0.05

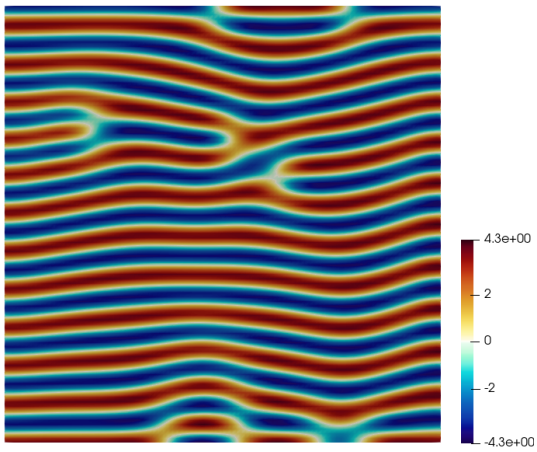

(e) u at t = 0.1

Figure 2.22: Solutions of phase-field crystal example 1. The color indicates the value of u field.

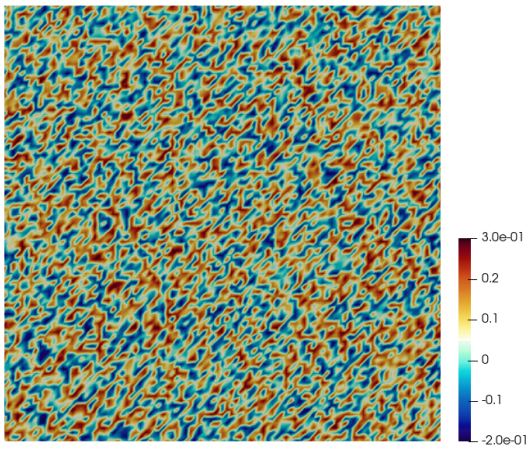

(a) u_0

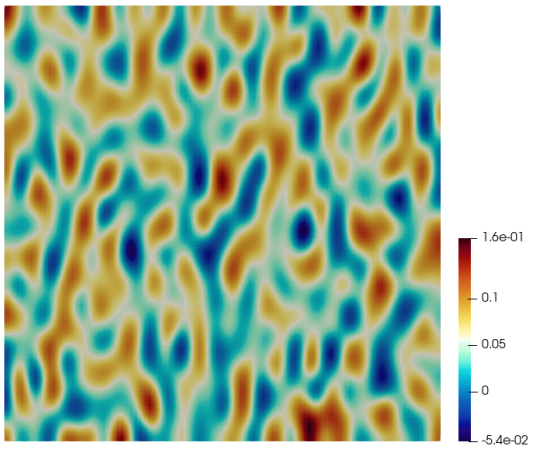

(b) u at t = 0.002

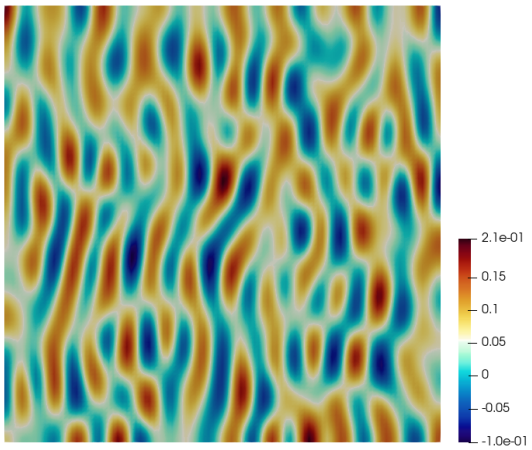

(c) u at t = 0.01

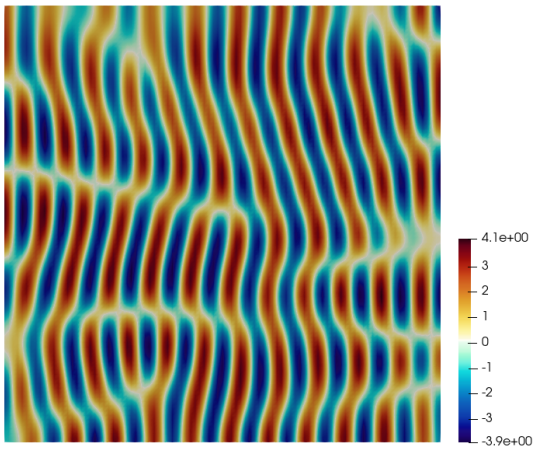

(d) u at t = 0.05

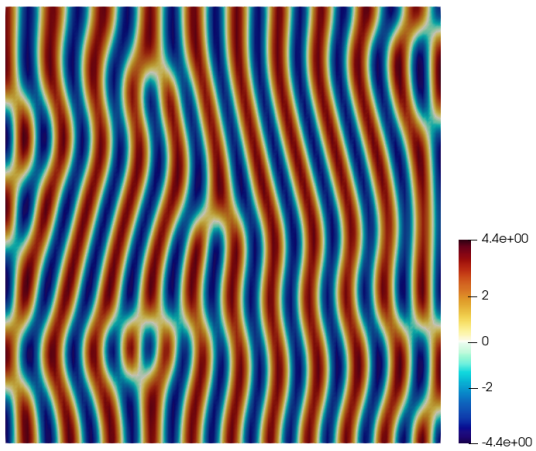

(e) u at t = 0.1

Figure 2.23: Solutions of phase-field crystal example 2. The color indicates the value of u field.

Considering Figures 2.22 and 2.23, we state that anisotropic pattern formation has been successfully modeled by the sixth-order Cahn-Hilliard equation. Using the fourth-order Cahn-Hilliard equation, it is not easy to model anisotropy because we encounter the ill-posedness. Therefore, it is recommended to use the sixth-order Cahn-Hilliard equation to model tumor growth and wound healing. Here, for both examples, we have the same parameter values except for a_{20} and a_{02}. a_{20} is the coefficient of the term $\frac{\partial^4 u}{\partial x^4}$. When a higher value of a_{20} is used, the interfacial area which has ∇u is in the x direction is going to be minimized. Therefore we obtain the Figure 2.22. Similarly, if a higher value of a_{02} is used, the interfacial area which has ∇u is in the y direction is going to be minimized.

CHAPTER 3

MECHANICS COUPLED WITH DIFFUSION

Lithium-ion batteries plays an important role in power systems such as electrical vehicles. Appropriate chemo-mechanical theory of the underlying physics of the lithium-ion batteries helps prevent the degradation of the performance of the electrode particles. In this manner, the diffusion-induced stress generation has been studied in [64, 65, 66] at small scales. In this chapter, we couple the Chan-Hilliard problem with mechanics considering the procedure in [40, 41].

3.1 Coupling of Cahn-Hilliard Equation with Finite Elasticity

The initial boundary-value problem of species diffusion in an elastic solid is a coupled problem, because the concentration of the species and deformation affect each other. In the coupling of mechanics and the Cahn-Hilliard equation, we have to consider three fields. These are the deformation field, the concentration, and the chemical potential.

$$\boldsymbol{\varphi} : \begin{cases} \mathcal{B}_0 \times T \longrightarrow \mathcal{B}_t \subset \boldsymbol{R}^3 \\ (\boldsymbol{X}, t) \longrightarrow \boldsymbol{x} = \varphi(\boldsymbol{X}, t) \end{cases} \tag{3.1}$$

$$c : \begin{cases} \mathcal{B}_0 \times T \longrightarrow [0,1] \\ (\boldsymbol{X}, t) \longrightarrow c(\boldsymbol{X}, t) \end{cases} \quad \text{and} \quad \mu : \begin{cases} \mathcal{B}_0 \times T \longrightarrow \boldsymbol{R} \\ (\boldsymbol{X}, t) \longrightarrow \mu(\boldsymbol{X}, t) \end{cases} \tag{3.2}$$

The deformation field $\boldsymbol{\varphi}$ maps the points in the reference configuration onto the points of the current configuration.

The concentration gradient, the negative of the chemical potential gradient and the deformation gradient are defined as:

$$\mathbb{C} := \nabla_{\boldsymbol{X}} c(\boldsymbol{X}, t) \tag{3.3a}$$

$$\mathbb{M} := -\nabla_{\boldsymbol{X}} \mu(\boldsymbol{X}, t) \tag{3.3b}$$

$$\boldsymbol{F} := \nabla_{\boldsymbol{X}} \boldsymbol{\varphi}(\boldsymbol{X}, t) \tag{3.3c}$$

$\boldsymbol{F}$ is the deformation gradient, its cofactor and its Jacobian are defined as $\mathrm{cof}[\boldsymbol{F}] := \det[\boldsymbol{F}]\boldsymbol{F}^{-T}$, $J := \det[\boldsymbol{F}]$ respectively. By the condition $J > 0$, the map, $\boldsymbol{\varphi}$ is constrained due to the non-penetrable deformation.

$$d\boldsymbol{x} = \boldsymbol{F} d\boldsymbol{X}, \quad d\boldsymbol{a} = \mathrm{cof}[\boldsymbol{F}] d\boldsymbol{A}, \quad dv = \det[\boldsymbol{F}] dV \tag{3.4}$$

Let $\boldsymbol{g}, \boldsymbol{G} \in Sym_+(3)$ be the standard metric tensors of the current and reference configurations. Then, the right and inverse of the left Cauchy-Green tensors are defined as:

$$\boldsymbol{C} := \boldsymbol{F}^T \boldsymbol{g} \boldsymbol{F} \quad \text{and} \quad \boldsymbol{c} := \boldsymbol{F}^{-T} \boldsymbol{G} \boldsymbol{F}^{-1} \tag{3.5}$$

3.1.1 Derivation of Local Balance Equations

No mass production is assumed due to chemical reactions. Therefore, conservation of solid mass is

$$\int_{P_t} \rho dv = \int_{P_0} \rho_0 dV \quad \text{and} \quad P_0 \subset \mathcal{B}_0, \quad P_t \subset \mathcal{B}_t \tag{3.6}$$

where $\rho(\boldsymbol{x}, t)$ and $\rho_0(\boldsymbol{X})$ are the density fields belonging to the current and reference configurations as shown in Figure 3.1.

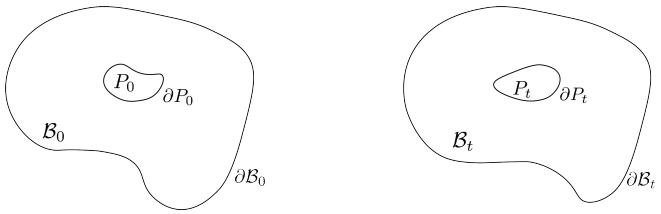

Figure 3.1: P_0 and P_t

It is assumed that no species is produced due to chemical reactions. Thus, conservation of the species is

$$\frac{d}{dt}\int_{P_0} c dV = -\int_{\partial P_t} h da \tag{3.7}$$

where h is the out-flux of species through the surface and $c(\boldsymbol{x}, t) \in [0, 1]$ is the concentration of species. The outward flux is defined through

$$h(\boldsymbol{x}, t; \mathbf{n}) := \mathbf{h}(\boldsymbol{x}, t) \cdot \mathbf{n} \tag{3.8}$$

where the $\mathbf{h}(\boldsymbol{x}, t)$ is spatial species flux vector. Then, the material species flux vector is defined as

$$\mathbf{H} \cdot d\boldsymbol{A} = \mathbf{h} \cdot d\boldsymbol{a} \quad \text{and} \quad \mathbf{H} := \boldsymbol{F}^{-1}(J\mathbf{h}), \tag{3.9}$$

The conservation of chemical microforces reads

$$\int_{P_0} g dV = -\int_{\partial P_t} \xi da \tag{3.10}$$

$g(\boldsymbol{x}, t)$ is the chemical microforce per unit volume of the reference configuration and $\xi(\boldsymbol{x}, t)$ is the normal microtraction.

$$\xi(\boldsymbol{x}, t; \mathbf{n}) := \mathbf{k}(\boldsymbol{x}, t) \cdot \mathbf{n} \tag{3.11}$$

where $\mathbf{k}(\boldsymbol{x}, t)$ is the spatial microtraction vector. Then the material microtraction vector is defined below.

$$\mathbf{K} \cdot d\boldsymbol{A} = \mathbf{k} \cdot d\boldsymbol{a} \quad \text{and} \quad \mathbf{K} := \boldsymbol{F}^{-1}(J\mathbf{k}) \tag{3.12}$$

By neglecting the inertia effect, the conservation of linear momentum becomes

$$\int_{\partial P_t} \boldsymbol{t} da + \int_{P_0} \bar{\boldsymbol{\gamma}} dV = \mathbf{0} \tag{3.13}$$

where $\bar{\boldsymbol{\gamma}}$ is the body force per unit volume of the reference configuration and $\boldsymbol{t}$ is the spatial stress traction vector. Cauchy's stress theorem, which is shown below, defines the stress traction vector.

$$\boldsymbol{t}(\boldsymbol{x}, t; \mathbf{n}) := \boldsymbol{\sigma}(\boldsymbol{x}, t)\mathbf{n} \tag{3.14}$$

where $\boldsymbol{\sigma}(\boldsymbol{x}, t)$ is the Cauchy stress tensor. Then the definition of the nominal stress tensor, $\boldsymbol{P}$ is

$$\boldsymbol{P} d\boldsymbol{A} = \boldsymbol{\sigma} d\boldsymbol{a} \quad \text{and} \quad \boldsymbol{P} := (J\boldsymbol{\sigma})\boldsymbol{F}^{-T} \tag{3.15}$$

The conservation of the angular momentum reads

$$\int_{\partial P_t} \boldsymbol{x} \times \boldsymbol{t} d\boldsymbol{a} + \int_{P_0} \boldsymbol{x} \times \overline{\boldsymbol{\gamma}} dV = \mathbf{0} \tag{3.16}$$

Through the localization of Equations (3.6), (3.7), (3.10), (3.13) and (3.16), we obtain the local form of the balance equations for finite elasticity coupled with diffusion. These local balance equations and their constitutive equations are presented in Equa-

tion (3.17)

1.	Balance of solid mass	$\rho_0 = \rho J$
2.	Balance of species content	$\dot{c} = -\operatorname{Div}[\boldsymbol{H}]$
3.	Balance of chemical microforce	$g = -\operatorname{Div}[\boldsymbol{K}]$
4.	Balance of linear momentum	$\operatorname{Div}[\boldsymbol{P}] + \bar{\boldsymbol{\gamma}} = \mathbf{0}$
5.	Balance of angular momentum	$\operatorname{skew}\left[\boldsymbol{P}\boldsymbol{F}^T\right] = \mathbf{0}$
6.	Constitutive stresses	$\boldsymbol{P} = \partial_{\boldsymbol{F}}\hat{\psi}(\boldsymbol{F}, c, \mathbb{C})$
7.	Constitutive microforce	$g = \mu - \partial_c\hat{\psi}(\boldsymbol{F}, c, \mathbb{C})$
8.	Constitutive microtraction	$\boldsymbol{K} = \partial_{\mathbb{C}}\hat{\psi}(\boldsymbol{F}, c, \mathbb{C})$
9.	Constitutive species flux	$\boldsymbol{H} = \partial_{\mathbb{M}}\hat{\phi}(\mathbb{M}; \boldsymbol{F}, c)$

(3.17)

The constitutive equations are obtained following the procedure outlined in [40]. $\hat{\psi}$ and $\hat{\phi}$ are expressed in Equations (3.24) and (3.30) respectively.

3.1.2 The Boundary Conditions and Initial Condition for the Coupled Problem

We have three primary fields; therefore, we need to write the boundary conditions for these three primary fields. These boundaries are shown in Equation (3.18)

$$\partial\mathcal{B}_0 = \partial\mathcal{B}_0^{\varphi} \cup \partial\mathcal{B}_0^{t}, \quad \partial\mathcal{B}_0 = \partial\mathcal{B}_0^{c} \cup \partial\mathcal{B}_0^{\xi}, \quad \partial\mathcal{B}_0 = \partial\mathcal{B}_0^{\mu} \cup \partial\mathcal{B}_0^{h} \tag{3.18}$$

$$\partial\mathcal{B}_0^{\varphi} \cap \partial\mathcal{B}_0^{t} = \emptyset, \quad \partial\mathcal{B}_0^{c} \cap \partial\mathcal{B}_0^{\xi} = \emptyset, \quad \partial\mathcal{B}_0^{\mu} \cap \partial\mathcal{B}_0^{h} = \emptyset \tag{3.19}$$

The Dirichlet and Neumann-type boundary conditions for the deformation field

$$\boldsymbol{\varphi} = \bar{\boldsymbol{\varphi}}(\boldsymbol{X}, t) \text{ on } \partial\mathcal{B}_0^{\varphi} \quad \text{and} \quad \boldsymbol{P}\mathbf{N} = \bar{\boldsymbol{t}}(x, t) \text{ on } \partial\mathcal{B}_t^{t} \tag{3.20}$$

for the concentration field

$$c = \bar{c}(X, t) \text{ on } \partial\mathcal{B}_0^{c} \text{ and } \mathbf{K}\cdot\mathbf{N} = \bar{\xi}(x, t) \text{ on } \partial\mathcal{B}_0^{\xi} \tag{3.21}$$

for the chemical potential field

$$\mu = \bar{\mu}(\boldsymbol{X}, t) \text{ on } \partial\mathcal{B}_0^{\mu} \quad \text{and} \quad \mathbf{H} \cdot \mathbf{N} = \bar{h}(\boldsymbol{x}, t) \text{ on } \partial\mathcal{B}_0^{h} \tag{3.22}$$

Here, $\mathbf{N}$ is the unit normal vector on the surface $\partial\mathcal{B}_0$ and the initial condition of concentration field is

$$c\left(\boldsymbol{X}, t_0\right) = c_0(\boldsymbol{X}) \text{ in } \mathcal{B}_0 \tag{3.23}$$

3.1.3 Isotropic Constitutive Model for Coupling Through Volumetric Deformation

Following [40], we consider a simple isotropic model for a coupled problem. Two constitutive functions, $\hat{\psi}, \hat{\phi}$ are chosen as follows. $\hat{\psi}$ is the energy storage function that is decomposed into elastic, chemical, and interface contributions.

$$\hat{\psi}(\boldsymbol{F}, c, \mathbb{C}) = \hat{\psi}_{el}\left(\boldsymbol{F}^{el}(\boldsymbol{F}, c)\right) + \hat{\psi}_{che}(c) + \hat{\psi}_{int}(\mathbb{C}) \tag{3.24}$$

A compressible Neo-Hookean form [67] is assumed for the elastic contribution.

$$\hat{\psi}_{el}\left(\boldsymbol{F}^{el}\right) = \frac{\gamma}{2}\left[\boldsymbol{F}^{el} : \boldsymbol{F}^{el} - 3\right] + \frac{\gamma}{\beta}\left[\left(\det \boldsymbol{F}^{el}\right)^{-\beta} - 1\right] \tag{3.25}$$

where γ is the shear modulus and the parameter β describes the weak volumetric compressibility of material, which has a relation with Poisson's ratio as $\beta = 2v/1-2v$

The deformation gradient is split into the elastic part, $\boldsymbol{F}^{el}$ and the volumetric swelling part, $\boldsymbol{F}^{c}$ multiplicatively. Thus, the coupling will be incorporated through the volumetric swelling part [41, 40].

$$\boldsymbol{F} = \boldsymbol{F}^{el}\boldsymbol{F}^{c} \quad \text{with} \quad \boldsymbol{F}^{c} := J_c^{1/3}\mathbf{1} \tag{3.26}$$

$$\boldsymbol{F}^{el} = J_c^{-1/3}\boldsymbol{F} \quad \text{with} \quad J_c = 1 + \Omega\left(c - c_0\right) \tag{3.27}$$

The chemical contribution to the free energy function is assumed to be the same as in the proposal of Cahn and Hilliard [45, 46, 48]. The chemical contribution is given for different a and b values in Figure 3.2. We must have a double-well chemical contribution to obtain a phase separation.

$$\hat{\psi}_{che}(c) = a[c \ln c + (1-c)\ln(1-c)] + bc(1-c) \tag{3.28}$$

The interface contribution is also the same as classical Cahn-Hilliard theory.

$$\hat{\psi}_{int}(\mathbb{C}) = \frac{\epsilon}{2}|\mathbb{C}|^2 \tag{3.29}$$

The convex quadratic form is assumed for the dissipation potential, $\hat{\phi}$, through the negative gradient of chemical potential.

$$\hat{\phi}(\mu; \boldsymbol{C}, c) = c(1-c)\frac{M}{2}\boldsymbol{C}^{-1} : (\mathbb{M} \otimes \mathbb{M}) \tag{3.30}$$

where $M > 0$ is the species mobility.

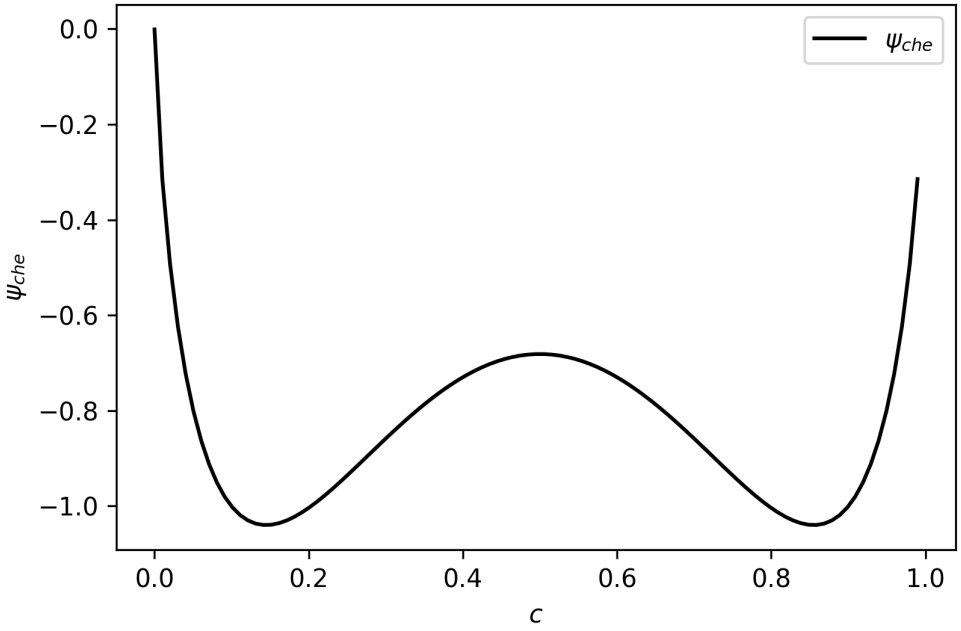

(a) Chemical energy, ψ_{che} for $a = 10$, $b = 25$

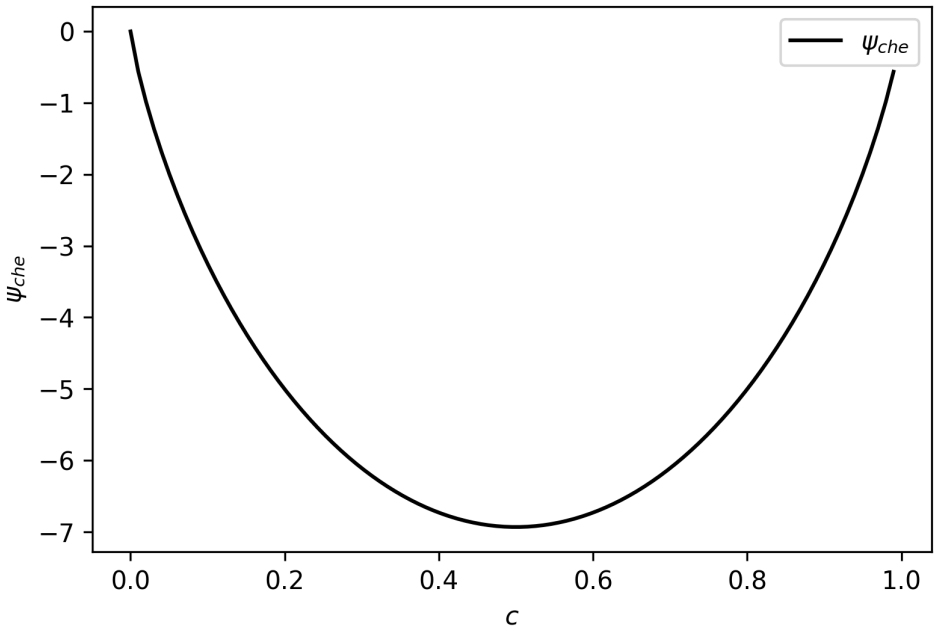

(b) Chemical energy, ψ_{che} for $a = 10$, $b = 0$

Figure 3.2: Chemical energy for different a and b values. $b > 2a$ leads to a double-well potential

Here, the expressions of $\boldsymbol{P}$, g, $\boldsymbol{H}$, and $\boldsymbol{K}$ in the local balance equations are determined using constitutive equations.

Since $\partial_{\boldsymbol{F}}\hat{\psi}_{che} = \mathbf{0}$ and $\partial_{\boldsymbol{F}}\hat{\psi}_{int} = \mathbf{0}$

$$\boldsymbol{P} = \partial_{\boldsymbol{F}}\hat{\psi}(\boldsymbol{F}, c, \mathbb{C}) = \partial_{\boldsymbol{F}}\hat{\psi}_{el} \tag{3.31}$$

$$\begin{aligned} \partial_{\boldsymbol{F}}\hat{\psi}_{el} &= J_c^{-1/3}\partial_{\boldsymbol{F}^{el}}\hat{\psi}_{el} \\ &= \gamma J_c^{-1/3}\left[\boldsymbol{F}^{el} - \left(\det \boldsymbol{F}^{el}\right)^{-\beta}\boldsymbol{F}^{e-T}\right] \end{aligned} \tag{3.32}$$

Therefore,

$$\boldsymbol{P} = \gamma J_c^{-1/3}\left[\boldsymbol{F}^{el} - \left(\det \boldsymbol{F}^{el}\right)^{-\beta}\boldsymbol{F}^{e-T}\right] \tag{3.33}$$

$$\partial_c\hat{\psi}_{el} = \Omega J_c^{-1} p \tag{3.34}$$

$$\begin{aligned} p &:= -\frac{1}{3}\partial_{\boldsymbol{F}}\hat{\psi}_{el} : \boldsymbol{F} \\ &= -\frac{1}{3}\boldsymbol{P} : \boldsymbol{F} \end{aligned} \tag{3.35}$$

where p is the pressure. Thus microforce is

$$\begin{aligned} g &= \mu - \partial_c\hat{\psi}_{che} - \partial_c\hat{\psi}_{el} \\ &= \mu - a\ln[\frac{c}{1-c}] - b(1-2c) - \Omega J_c^{-1} p \end{aligned} \tag{3.36}$$

The microtraction expression reads

$$\boldsymbol{K} = \partial_{\mathbb{C}}\hat{\psi} = \epsilon\nabla_{\boldsymbol{X}} c \tag{3.37}$$

Then, the species flux expression is

$$\boldsymbol{H} = -c_n\left(1 - c_n\right) M\boldsymbol{C}_n^{-1}\mathbb{M} \tag{3.38}$$

where c_n is the concentration at the previous time, and $\boldsymbol{C}_n$ is the right Cauchy-Green tensor at the previous time.

3.1.4 Curvature Calculation

The curvature of the concentration might have effects on the stress evolution in the body. These effects are not investigated in this thesis, but we will investigate them in the future. Moreover, we presented the curvature of the concentration using the following formulation.

Gaussian curvature K and mean curvature H of the surface are obtained from the first and second fundamental form of the surface [68].

The curvature of the concentration field can be calculated as follows. Note that the subscript x and y denote the partial derivatives of the field with respect to the spatial coordinates x and y.

$$\begin{aligned} K &= \frac{LN - M^2}{EG - F^2} \\ H &= \frac{1}{2}\frac{LG - 2MF + NE}{EG - F^2} \end{aligned} \tag{3.39}$$

where

$$\begin{aligned} E &= 1 + c_x^2 \\ F &= c_x c_y \\ G &= 1 + c_y^2 \\ L &= \frac{c_{xx}}{\sqrt{1 + c_x^2 + c_y^2}} \\ M &= \frac{c_{xy}}{\sqrt{1 + c_x^2 + c_y^2}} \\ N &= \frac{c_{yy}}{\sqrt{1 + c_x^2 + c_y^2}} \end{aligned} \tag{3.40}$$

Therefore the principal curvatures can be expressed as

$$\begin{aligned} \kappa_{max} &= H + \sqrt{H^2 - K} \\ \kappa_{min} &= H - \sqrt{H^2 - K} \end{aligned} \tag{3.41}$$

3.1.5 Numerical Simulations

To obtain the numerical solution of the chemomechanical problem, we need the weak form of the problem.

Weak Form of Three-Field Coupled Problem:

$$\int_{\mathcal{B}} \dot{c} q dV = \int_{\mathcal{B}} \boldsymbol{H} \cdot \nabla_{\boldsymbol{X}} q dV \tag{3.42a}$$

$$\int_{\mathcal{B}} g w dV = \int_{\mathcal{B}} \boldsymbol{K} \cdot \nabla_{\boldsymbol{X}} w dV \tag{3.42b}$$

$$\int_{\mathcal{B}} \boldsymbol{P} : \nabla_{\boldsymbol{X}} \boldsymbol{e} dV = \int_{\mathcal{B}} \bar{\boldsymbol{\gamma}} \cdot \boldsymbol{e} dV \tag{3.42c}$$

where q, w and $\boldsymbol{e}$ are the test functions for the concentration, the chemical potential and the deformation field, respectively. The model parameters are presented in Table 3.1. With these parameters we will solve the Cahn-Hilliard coupled with the finite elasticity problem in the two-dimensional ($[0, 0.5] \times [0, 0.5]$) and three-dimensional domains ($[0, 0.5] \times [0, 0.5] \times [0, 0.5]$). For the two-dimensional problem, the displacements are set as zero in the x and y direction at point (0,0). Also for point (0,0.5), the zero displacement is set in y direction. For the rest of the boundary, we have zero traction.

In addition, we solve the 3D problem as well using the same parameters as in the 2D problem. 3D solution is demonstrated in Figure 3.6

Table 3.1: Parameters of model problem

No.	Parameter	Name	Value	Unit
1	γ	Shear modulus	3	[N/m^2]
2	v	Poisson's ratio	0.3	[-]
3	Ω	Swelling parameter	$0-10$	[-]
4	a	Chemical energy parameter	10	[N/m^2]
5	b	Mixing energy parameter	$2.5a$	[N/m^2]
6	ϵ	Interface parameter	0.001	[N]
7	M	Mobility parameter	0.001	[m^4/Ns]
8	c_0	Initial concentration	0.5	[-]

In Figures 3.3 and 3.6, we see the diffusion induced deformation for 2D and 3D problem respectively. For the phase where the concentration is increased, we observe the expansion. For the phase where the concentration is decreased, we see the swelling. The mean and Gaussian curvature of the concentration field for 2D problem is visualized in Figures 3.4 and 3.5.

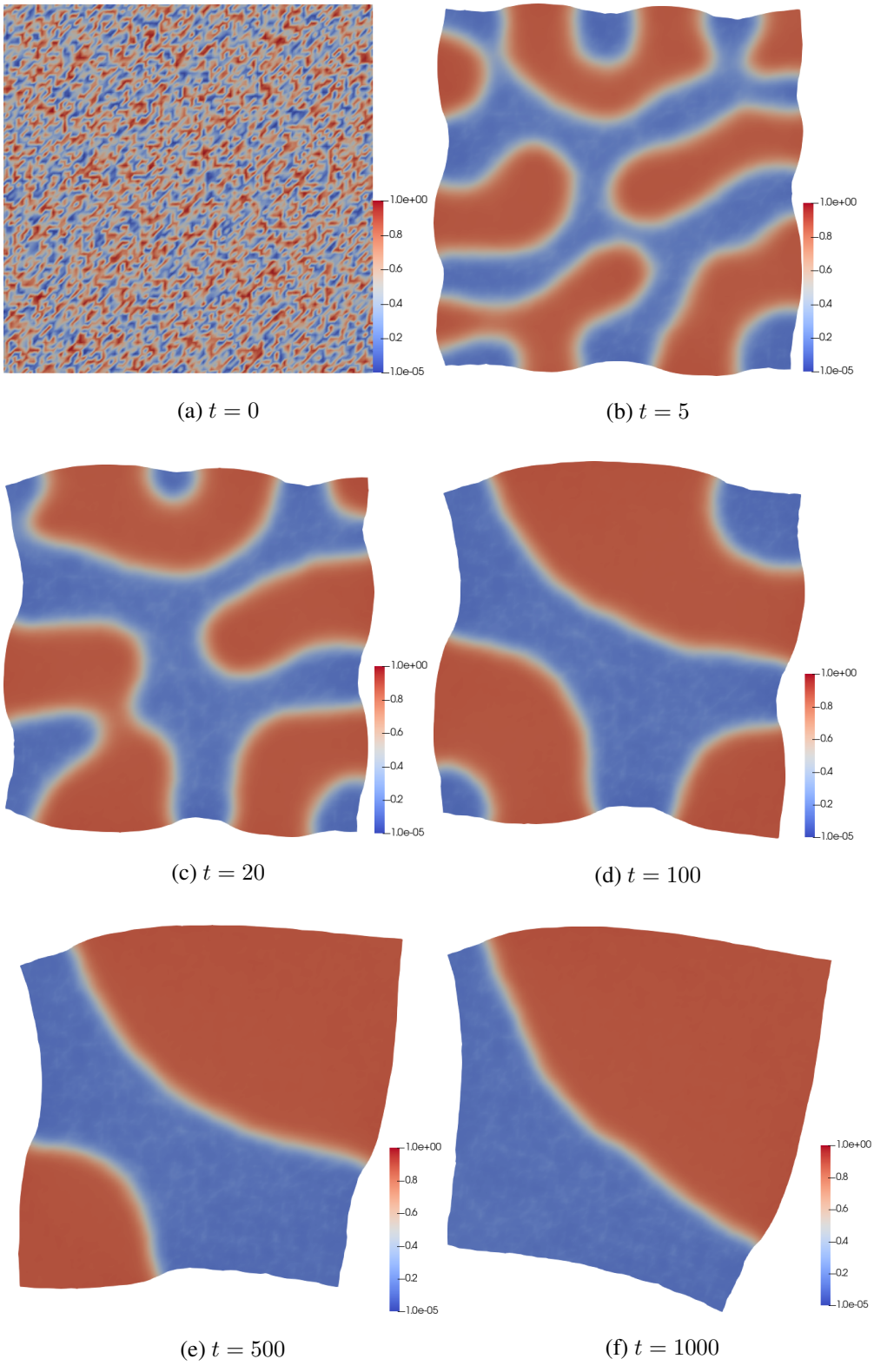

(a) $t = 0$ (b) $t = 5$

(c) $t = 20$ (d) $t = 100$

(e) $t = 500$ (f) $t = 1000$

Figure 3.3: Solution of the Cahn-Hilliard problem coupled with finite elasticity in the two-dimensional domain. The color indicates the concentration field, and deformed shapes show the deformation field.

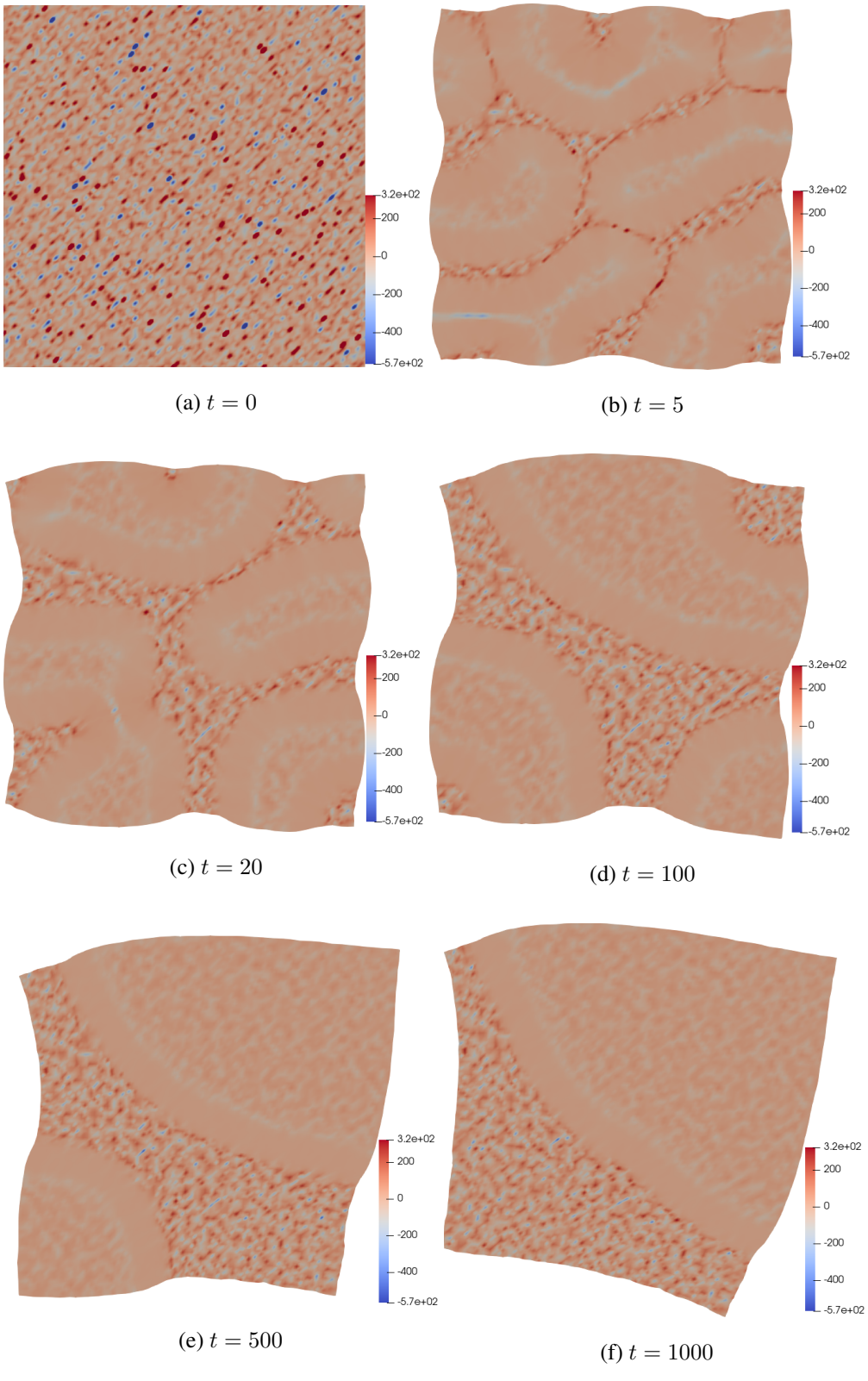

(a) $t = 0$ (b) $t = 5$

(c) $t = 20$ (d) $t = 100$

(e) $t = 500$ (f) $t = 1000$

Figure 3.4: Mean curvature of the concentration field in Figure 3.3. The color indicates the mean curvature field

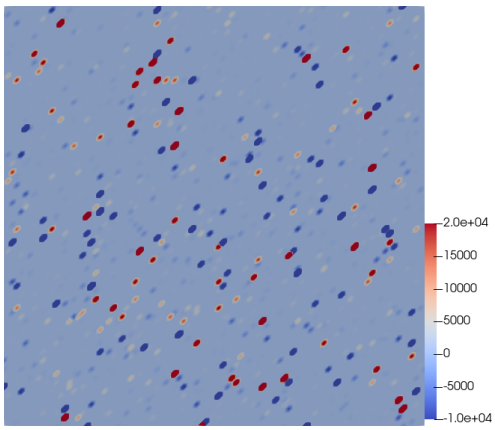

(a) $t = 0$

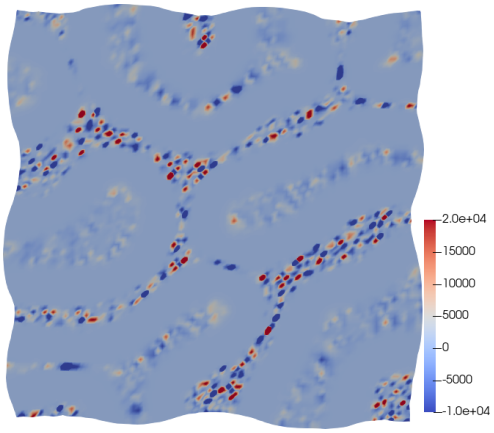

(b) $t = 5$

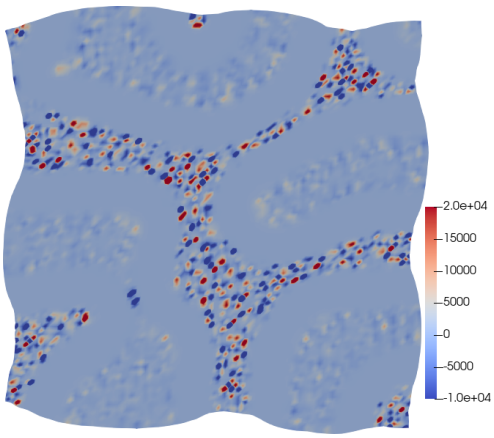

(c) $t = 20$

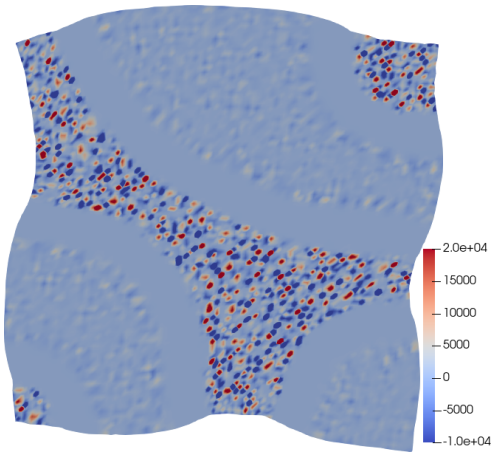

(d) $t = 100$

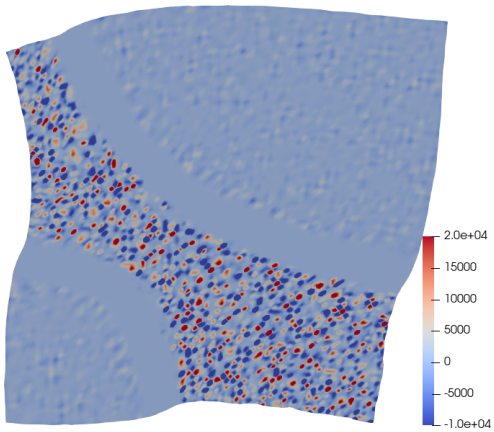

(e) $t = 500$

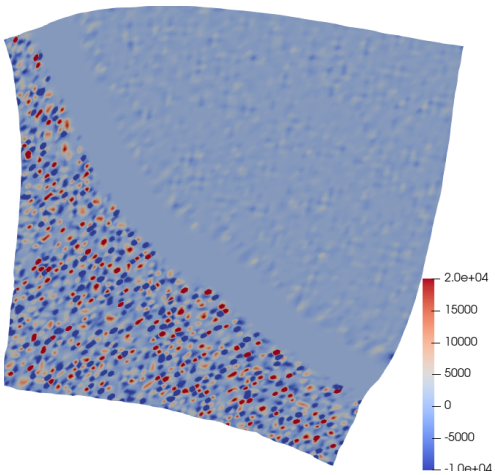

(f) $t = 1000$

Figure 3.5: Gaussian curvature of the concentration field in Figure 3.3. The color indicates the Gaussian curvature field

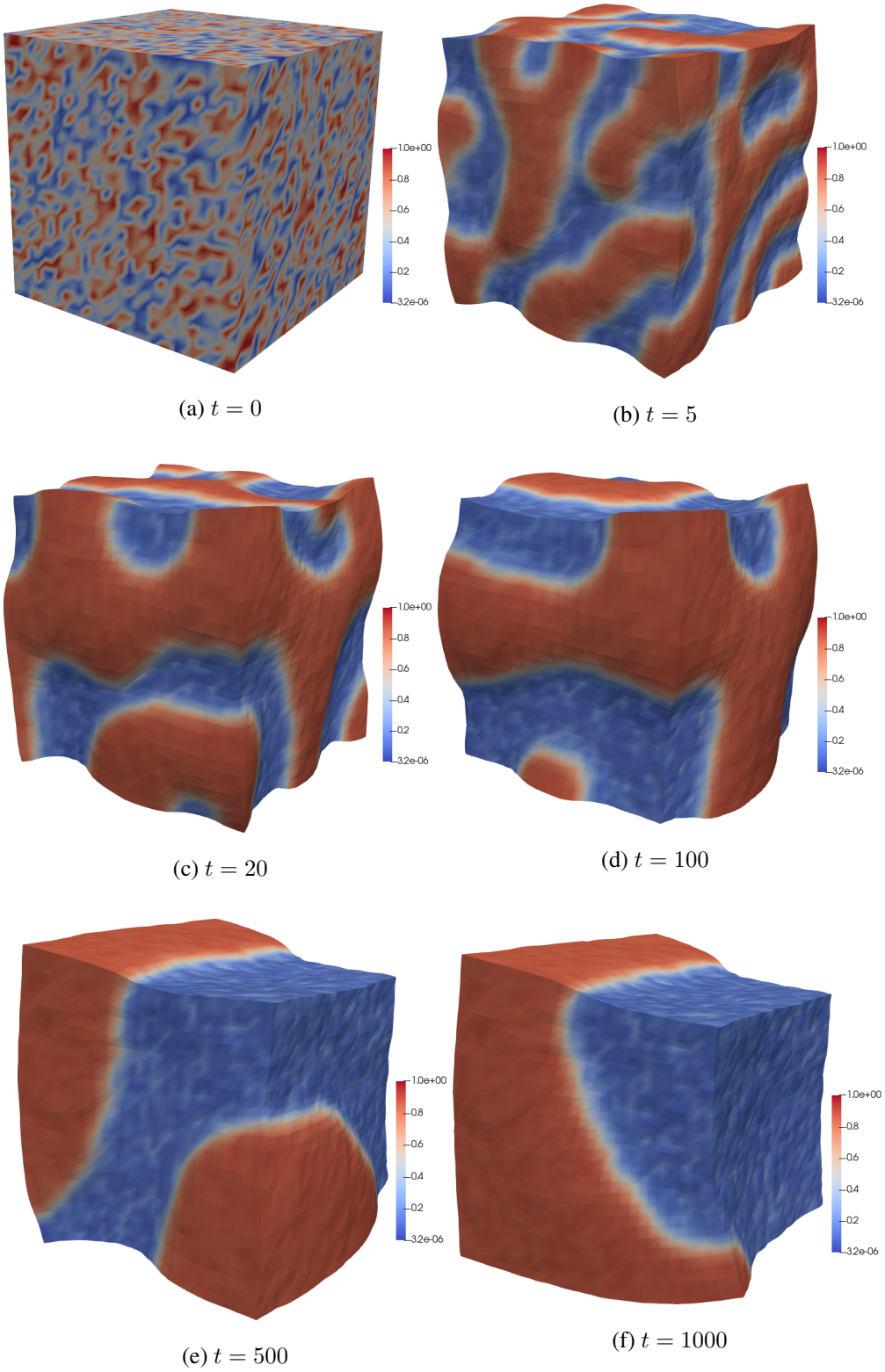

(a) $t = 0$ (b) $t = 5$

(c) $t = 20$ (d) $t = 100$

(e) $t = 500$ (f) $t = 1000$

Figure 3.6: Solution of the Cahn-Hilliard problem coupled with finite elasticity in the three-dimensional domain. The color indicates the concentration field, and deformed shapes show the deformation field.

3.1.5.1 Elasticity Coupled with the Cahn-Hilliard Equation with Extra Term

In this section, we add an extra term to the energy storage function $\hat{\psi}(\boldsymbol{F}, c, \mathbb{C})$. We consider Equation (3.24) as follows

$$\hat{\psi}(\boldsymbol{F}, c, \mathbb{C}) = \hat{\psi}_{el}\left(\boldsymbol{F}^{el}(\boldsymbol{F}, c)\right) + \hat{\psi}_{che}(c) + \hat{\psi}_{int}(\mathbb{C}) + \hat{\psi}_{extra}(\boldsymbol{F}^{el}(\boldsymbol{F}, c), \mathbb{C}) \quad (3.43)$$

with

$$\hat{\psi}_{extra}(\boldsymbol{F}^{el}(\boldsymbol{F}, c), \mathbb{C}) = d\boldsymbol{F}^{el^T}\boldsymbol{F}^{el} : (\mathbb{C} \otimes \mathbb{C}) \quad (3.44)$$

where d is the coefficient to control the contribution of the additional interface stretch term.

The interface stretch term couples the deformation gradient and the concentration gradient. We add this stretch term to the storage energy function. By solving the partial differential equations, we minimize the storage function. Therefore, interface stretch term contribution should be minimized. This term is only valid in the interface region because it has the concentration gradient term. To minimize the interface stretch term, the solution increases the interface area; this leads to decreasing the concentration gradient or decrease the deformation gradient in the interface region.

Here, we added the interface stretch term, but we will try to add the following term in the future.

$$\hat{\psi}_{newextra}(\boldsymbol{F}^{el}(\boldsymbol{F}, c), \mathbb{C}) = e\boldsymbol{F}^{el}\mathbb{C} \cdot \boldsymbol{F}^{el}\mathbb{C} \quad (3.45)$$

where e is the coefficient to control the contribution of the new interface stretch term. Again this is a future work.

To combine with the previous formulation, we need to add the terms below to the

necessary part of weak form of the equation.

$$\begin{aligned}
\partial_c \hat{\psi}_{extra}(\boldsymbol{F}^{el}(\boldsymbol{F}, c), \mathbb{C}) &= \Omega J_c^{-1} p_{extra} \\
\partial_{\boldsymbol{F}} \hat{\psi}_{extra}(\boldsymbol{F}^{el}(\boldsymbol{F}, c), \mathbb{C}) &= J_c^{-1/3} \partial_{\boldsymbol{F}^{el}} \hat{\psi}_{extra} \\
\partial_{\mathbb{C}} \hat{\psi}_{extra}(\boldsymbol{F}^{el}(\boldsymbol{F}, c), \mathbb{C}) &= \boldsymbol{F}^{el^T} \boldsymbol{F}^{el} : ((\delta_{ik}\mathbb{C}_j + \mathbb{C}_i\delta_{jk})\mathbf{e}_i \otimes \mathbf{e}_j \otimes \mathbf{e}_k)
\end{aligned} \tag{3.46}$$

where

$$\begin{aligned}
p_{extra} &:= -\frac{1}{3}\partial_{\boldsymbol{F}} \hat{\psi}_{extra} : \boldsymbol{F} \\
\partial_{\boldsymbol{F}^{el}} \hat{\psi}_{extra} &= \left((\delta_{Km}\delta_{kM}\boldsymbol{F}^{el}_{kL} + \boldsymbol{F}^{el}_{Kk}\delta_{km}\delta_{LM})\mathbf{e}_K \otimes \mathbf{e}_L \otimes \mathbf{e}_m \otimes \mathbf{e}_M\right) : (\mathbb{C} \otimes \mathbb{C})
\end{aligned} \tag{3.47}$$

since

$$\frac{\partial(\boldsymbol{F}^{el}_{kK}{}^T \boldsymbol{F}^{el}_{kL})}{\partial \boldsymbol{F}^{el}_{mM}} = (\delta_{Km}\delta_{kM}\boldsymbol{F}^{el}_{kL} + \boldsymbol{F}^{el}_{Kk}\delta_{km}\delta_{LM}) \tag{3.48}$$

where i, j, k, K, L, m, M are indices and $\mathbf{e}$ denotes the basis vector. Note that δ is Kronecker's delta.

Here, we used the values of given parameters in Table 3.1 and $d = 10^{-3}$. Figure 3.7 has different pattern than Figure 3.3. In other words, the additional interface stretch term affects the pattern formation. Furthermore, Figure 3.7 has more interface thickness as expected. We explained the reason of it. This interface thickness growth easily observed in mean and Gaussian curvature plots in Figures 3.8 and 3.9.

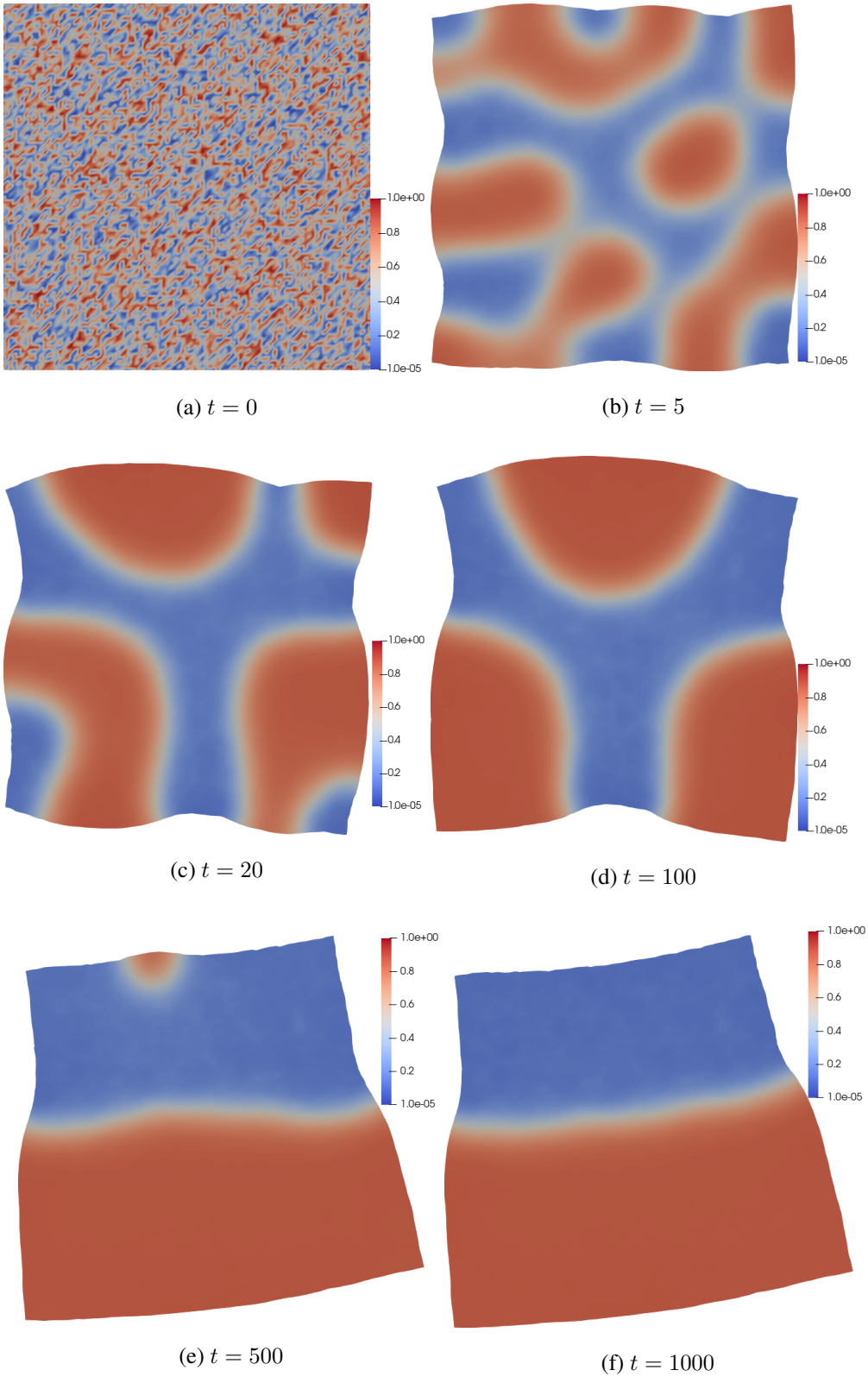

(a) $t = 0$ (b) $t = 5$

(c) $t = 20$ (d) $t = 100$

(e) $t = 500$ (f) $t = 1000$

Figure 3.7: Solution of the Cahn-Hilliard problem coupled with the finite elasticity considering the additional interface stretch term in the two-dimensional domain. The color indicates the concentration field, and deformed shapes show the deformation field.

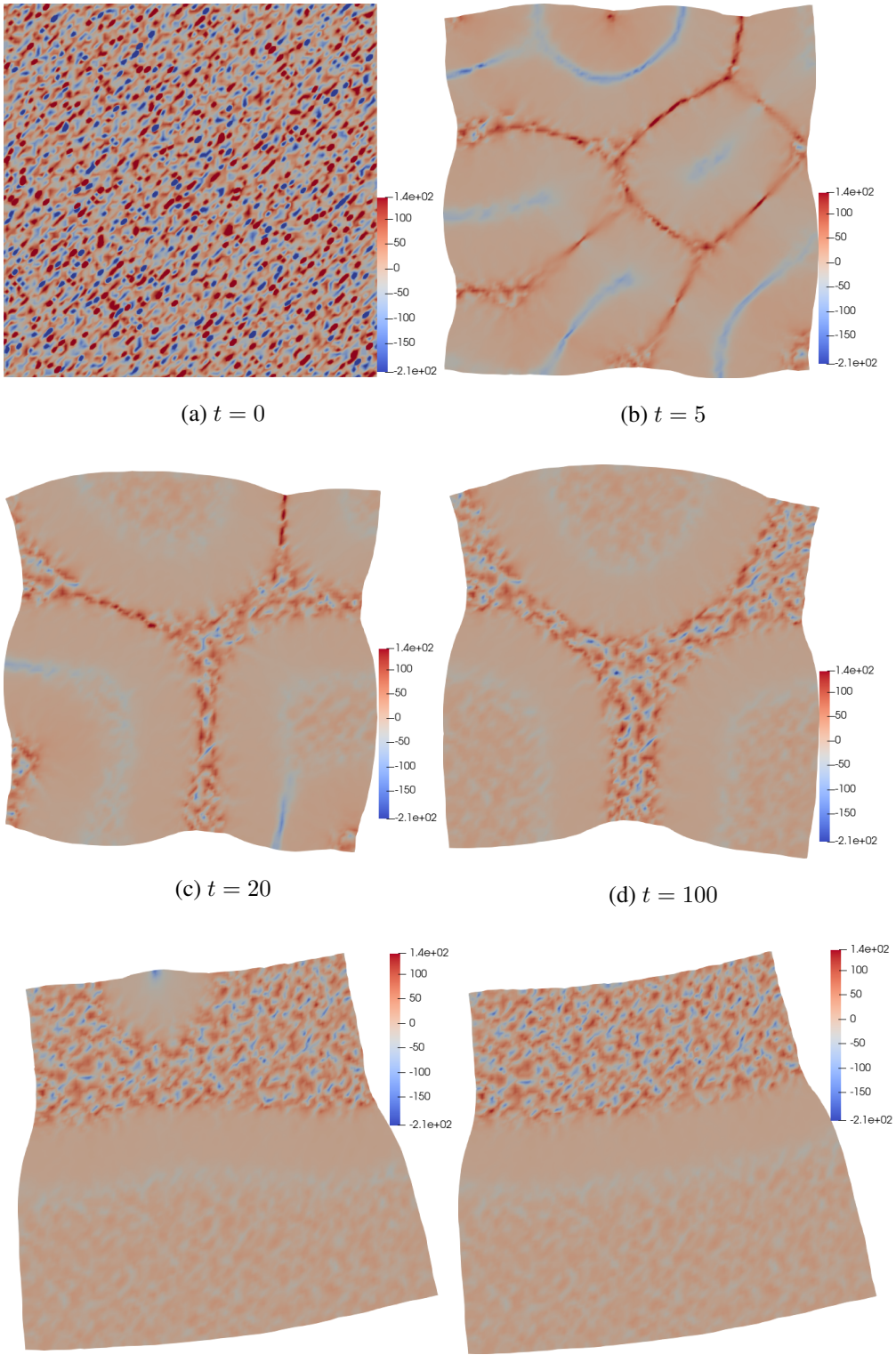

(a) $t = 0$ (b) $t = 5$

(c) $t = 20$ (d) $t = 100$

(e) $t = 500$ (f) $t = 1000$

Figure 3.8: Mean curvature of the concentration field in Figure 3.7

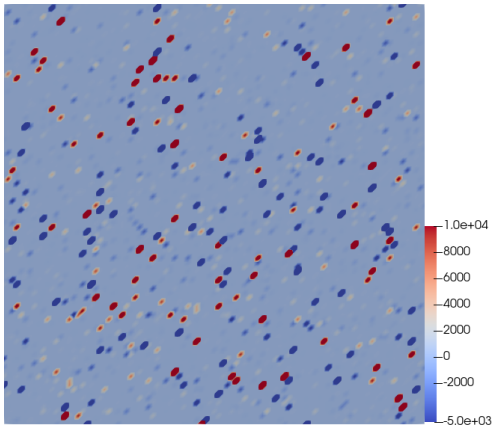

(a) $t = 0$

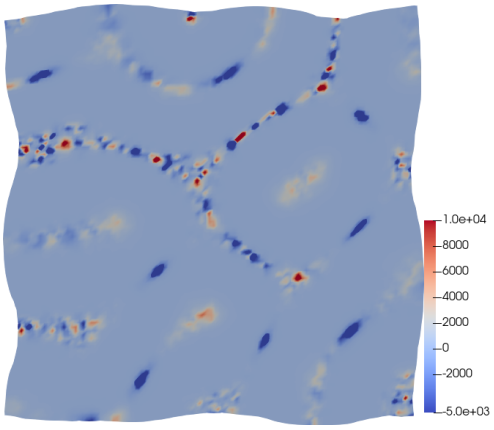

(b) $t = 5$

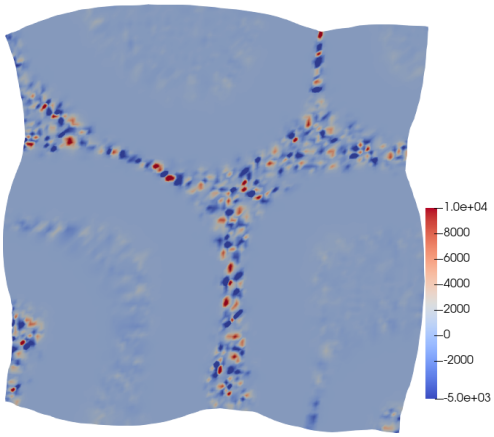

(c) $t = 20$

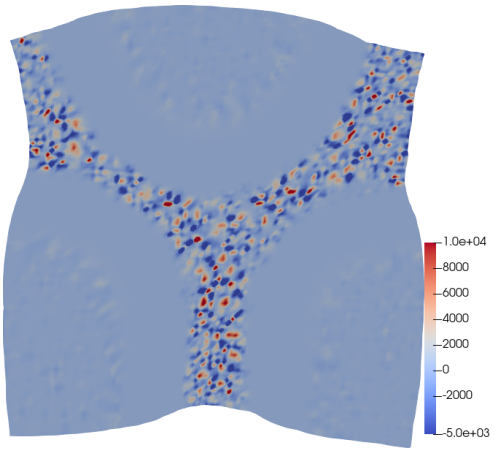

(d) $t = 100$

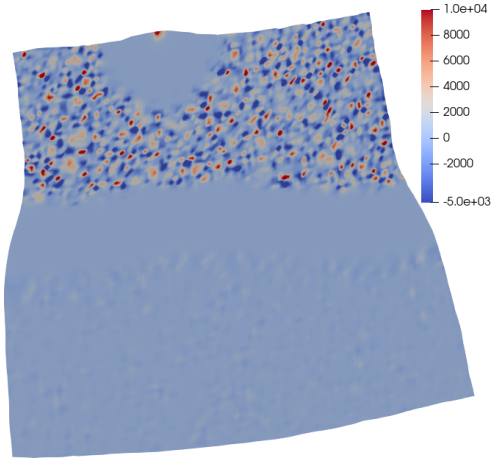

(e) $t = 500$

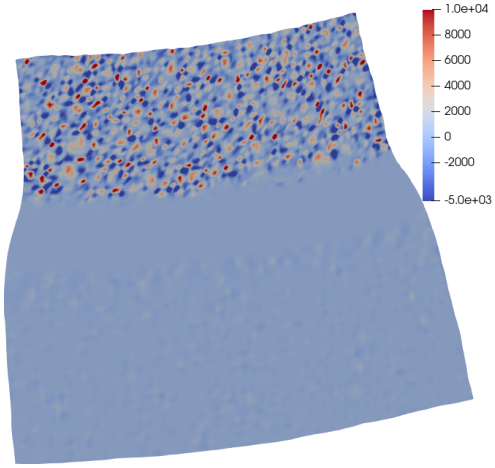

(f) $t = 1000$

Figure 3.9: Gaussian curvature of the concentration field in Figure 3.7

3.2 Finite Linear Viscoelasticity Coupled with Diffusion

3.2.1 Finite Linear Viscoelasticity with Volumetric-Isochoric Split

The finite linear elasticity is extended towards the finite linear viscoelasticity using the isochoric part of the free energy function through the procedure that is introduced in [69]. The multiplicative decomposition of the deformation gradient procedure is followed. Consider the deformation gradient decomposed as

$$\begin{aligned} \boldsymbol{F} &= \bar{\boldsymbol{F}}\boldsymbol{F}_{vol} \\ \bar{\boldsymbol{F}} &:= J^{-\frac{1}{3}}\boldsymbol{F} \\ \boldsymbol{F}_{vol} &:= J^{\frac{1}{3}}\mathbf{1} \end{aligned} \tag{3.49}$$

where $\boldsymbol{F}_{vol}$ and $\bar{\boldsymbol{F}}$ are the volumetric and isochoric part of the deformation gradient, respectively.

Consider that the volumetric deformation is purely elastic, and the isochoric deformation is viscoelastic. The following form of the stored-energy function is taken into account [69].

$$\hat{\psi}\left(\boldsymbol{C}\right) = \hat{\psi}_{vol}(J) + \hat{\psi}^{e}_{iso}\left(\bar{\boldsymbol{C}}\right) + \hat{\psi}^{v}_{iso}\left(\bar{\boldsymbol{C}}, \boldsymbol{A}\right) \tag{3.50}$$

with

$$\begin{aligned} \hat{\psi}_{vol}(J) &= \tfrac{1}{2}\kappa\left(\tfrac{1}{2}\left(J^2-1\right) - \ln J\right), \\ \hat{\psi}^{e}_{iso}\left(\bar{\boldsymbol{C}}\right) &= \tfrac{1}{2}\mu(\bar{\boldsymbol{C}} : \mathbf{1} - 3) = \tfrac{1}{2}\mu(\mathrm{tr}[\bar{\boldsymbol{C}}] - 3) \end{aligned} \tag{3.51}$$

where J is the Jacobian determinant $J := \det[\boldsymbol{F}]$ and $\bar{\boldsymbol{C}}$ is the right Cauchy-Green tensor which is defined as $\bar{\boldsymbol{C}} := \bar{\boldsymbol{F}}^T\bar{\boldsymbol{F}}$. Furthermore, κ and μ are the bulk and shear moduli respectively.

The second Piola-Kirchhoff stress tensor is stated as

$$\boldsymbol{S} = \boldsymbol{S}_{vol} + \boldsymbol{S}_{iso} \tag{3.52}$$

with

$$\begin{aligned}\boldsymbol{S}_{vol} &= J\hat{\psi}'_{vol}(J)\boldsymbol{C}^{-1}\\ \boldsymbol{S}_{iso} &= J^{-\frac{2}{3}}\mathrm{DEV}\left[\bar{\boldsymbol{S}}^{e}_{iso}+\bar{\boldsymbol{Q}}\right]\\ &= \boldsymbol{S}^{e}_{iso}+\boldsymbol{Q}\end{aligned} \tag{3.53}$$

where

$$\begin{aligned}\bar{\boldsymbol{S}}^{e}_{iso} &= 2\partial_{\bar{\boldsymbol{C}}}\hat{\psi}^{e}_{iso}(\bar{\boldsymbol{C}})\\ \bar{\boldsymbol{Q}} &= 2\partial_{\bar{\boldsymbol{C}}}\hat{\psi}^{v}_{iso}(\bar{\boldsymbol{C}},\boldsymbol{A})\end{aligned} \tag{3.54}$$

and $\overline{\boldsymbol{Q}}$ is the isochoric viscous overstress, which can be obtained by the following evolution equation.

$$\dot{\bar{\boldsymbol{Q}}}+\frac{1}{\tau}\bar{\boldsymbol{Q}} = \beta\frac{d}{dt}\left(\mathrm{DEV}\left[\bar{\boldsymbol{S}}^{e}_{iso}\right]\right) \tag{3.55}$$

where τ is the relaxation time, and β is the stiffness ratio

Note that $\mathrm{DEV}[\bullet] = [\bullet] : \left[\mathbb{I}-\frac{1}{3}\boldsymbol{C}\otimes\boldsymbol{C}^{-1}\right]$

There are many ways to deal with the evolution equation. Here, we solved coupled with the mechanics equations.

3.2.2 Finite Linear Viscoelasticity Coupled with the Cahn-Hilliard equation

The following energy storage function is used. This function is obtained by replacing the elastic part of the free energy in [40] with the free energy in Equation (3.50).

$$\hat{\psi}(\boldsymbol{F},c,\mathbb{C}) = \hat{\psi}_{mech}\left(\boldsymbol{F}^{mech}(\boldsymbol{F},c)\right)+\hat{\psi}_{che}(c)+\hat{\psi}_{int}(\mathbb{C}) \tag{3.56}$$

with

$$\hat{\psi}\left(\boldsymbol{F}^{mech}(\boldsymbol{F},c)\right)_{mech} = \hat{\psi}_{vol}(J)+\hat{\psi}_{iso}\left(\bar{\boldsymbol{C}}\right) \tag{3.57}$$

and

$$\begin{aligned} \hat{\psi}_{vol}(J_{mech}) &= \tfrac{1}{2}\kappa\left(\tfrac{1}{2}\left({J_{mech}}^2-1\right)-\ln J_{mech}\right), \\ \hat{\psi}_{iso}\left(\bar{\boldsymbol{C}}\right) &= \tfrac{1}{2}\mu(\bar{\boldsymbol{C}}:\mathbf{1}-3)=\tfrac{1}{2}\mu(\mathrm{tr}[\bar{\boldsymbol{C}}]-3) \end{aligned} \tag{3.58}$$

where $\bar{\boldsymbol{C}}$ and J are defined in Equations (3.61) and (3.62) respectively. The chemical and the interface contributions of the free energy function are same with Equation (3.28) and (3.29) respectively.

The deformation gradient splits into the mechanical part, $\boldsymbol{F}^{mech}$ and the volumetric swelling part $\boldsymbol{F}^{c}$ multiplicatively using the same procedure in [40].

$$\boldsymbol{F}=\boldsymbol{F}^{mech}\boldsymbol{F}^{c} \quad \text{with} \quad \boldsymbol{F}^{c}:=J_c^{1/3}\mathbf{1} \tag{3.59}$$

$$\boldsymbol{F}^{mech}=J_c^{-1/3}\boldsymbol{F} \quad \text{with} \quad J_c=1+\Omega\left(c-c_0\right) \tag{3.60}$$

The mechanical part of the deformation gradient is also split into volumetric and isochoric parts using the procedure which is explained in [69].

$$\begin{aligned} \boldsymbol{F}^{mech} &= \bar{\boldsymbol{F}}\boldsymbol{F}_{vol} \\ \bar{\boldsymbol{F}} &:= {J_{mech}}^{-\frac{1}{3}}\boldsymbol{F}^{mech} \\ \boldsymbol{F}_{vol} &:= {J_{mech}}^{\frac{1}{3}}\mathbf{1} \\ \bar{\boldsymbol{C}} &:= \bar{\boldsymbol{F}}^{T}\bar{\boldsymbol{F}} \\ \boldsymbol{C}^{mech} &:= {\boldsymbol{F}^{mech}}^{T}\boldsymbol{F}^{mech} \end{aligned} \tag{3.61}$$

with

$$J_{mech}:=\det[\boldsymbol{F}^{mech}] \tag{3.62}$$

The expressions of $\boldsymbol{P}$, g, $\boldsymbol{H}$, and $\boldsymbol{K}$ in the local balance equations are determined

using constitutive equations similarly to the previous section.

$$\boldsymbol{P} = \partial_{\boldsymbol{F}} \hat{\psi}(\boldsymbol{F}, c, \mathbb{C}) = \partial_{\boldsymbol{F}} \hat{\psi}_{mech} \tag{3.63}$$

$$\begin{aligned}
\partial_{\boldsymbol{F}} \hat{\psi}_{mech} &= J_c^{-1/3} \partial_{\boldsymbol{F}^{mech}} \hat{\psi}_{mech} \\
&= J_c^{-1/3} \boldsymbol{F} 2 \partial_{\boldsymbol{C}^{mech}} \hat{\psi}_{mech} \\
&= J_c^{-1/3} \boldsymbol{F} \underbrace{\left[J_{mech} \Psi'_{vol}(J_{mech}) \boldsymbol{C}^{-1} + {J_{mech}}^{-\frac{2}{3}} \mathrm{DEV}\left[2 \partial_{\bar{\boldsymbol{C}}} \Psi_{iso}(\bar{\boldsymbol{C}}) + \bar{\boldsymbol{Q}} \right] \right]}_{\boldsymbol{S}_{mech} := \boldsymbol{S}_{vol} + \boldsymbol{S}_{iso}}
\end{aligned} \tag{3.64}$$

Therefore,

$$\boldsymbol{P} = J_c^{-1/3} \boldsymbol{F} \left[J_{mech} \Psi'_{vol}(J_{mech}) \boldsymbol{C}^{-1} + {J_{mech}}^{-\frac{2}{3}} \mathrm{DEV}\left[2 \partial_{\bar{\boldsymbol{C}}} \Psi_{iso}(\bar{\boldsymbol{C}}) + \bar{\boldsymbol{Q}} \right] \right] \tag{3.65}$$

$$\partial_c \hat{\psi}_{mech} = \Omega J_c^{-1} p \tag{3.66}$$

$$\begin{aligned}
p &:= -\frac{1}{3} \partial_{\boldsymbol{F}} \hat{\psi}_{mech} : \boldsymbol{F} \\
&= -\frac{1}{3} \boldsymbol{P} : \boldsymbol{F}
\end{aligned} \tag{3.67}$$

where p is the pressure. Thus microforce is

$$\begin{aligned}
g &= \mu - \partial_c \hat{\psi}_{che} - \partial_c \hat{\psi}_{mech} \\
&= \mu - a \ln[\frac{c}{1-c}] - b(1-2c) - \Omega J_c^{-1} p
\end{aligned} \tag{3.68}$$

The microtraction and species flux are same with Equation (3.37) and (3.38) respectively.

Weak Form of the Finite Viscoelasticity Coupled with the Cahn-Hilliard Problem

$$\int_{\mathcal{B}} \dot{c} q dV = \int_{\mathcal{B}} \boldsymbol{H} \cdot \nabla_{\boldsymbol{X}} q dV \tag{3.69a}$$

$$\int_{\mathcal{B}} g w dV = \int_{\mathcal{B}} \boldsymbol{K} \cdot \nabla_{\boldsymbol{X}} w dV \tag{3.69b}$$

$$\int_{\mathcal{B}} \boldsymbol{P} : \nabla_{\boldsymbol{X}} \boldsymbol{e} dV = \int_{\mathcal{B}} \bar{\boldsymbol{\gamma}} \cdot \boldsymbol{e} dV \tag{3.69c}$$

with

$$\int_{\mathcal{B}} \dot{\bar{\boldsymbol{Q}}} : \boldsymbol{U} dV + \int_{\mathcal{B}} \frac{1}{\tau} \bar{\boldsymbol{Q}} : \boldsymbol{U} dV = \int_{\mathcal{B}} \beta \frac{d}{dt} \left(\mathrm{DEV} \left[\bar{\boldsymbol{S}}^{e}_{iso} \right] \right) : \boldsymbol{U} dV \tag{3.70}$$

where q, w, $\boldsymbol{e}$ and $\boldsymbol{U}$ are test functions for concentration, chemical potential, deformation and isochoric viscous overstress field respectively. The rest of the notations are defined in the previous subsections.

CHAPTER 4

MODELING OF SELF-ASSEMBLY

4.1 Coupled Cahn-Hilliard Equations

The coupling of two Cahn-Hilliard equations is used to model the self-assembly of the block copolymer [39]. Two or more chemically distinct block polymers forms the block copolymer.

Coupling of two Cahn-Hilliard equations are obtained by the minimization of the following energy functional.

$$\begin{aligned} F \equiv & F_{\epsilon_1,\epsilon_2,\varrho}(c_1,c_2) \\ = & \int_{\mathcal{B}} \left\{ \frac{\epsilon_1^2}{2}|\nabla_{\boldsymbol{x}} c_1|^2 + \frac{\epsilon_2^2}{2}|\nabla_{\boldsymbol{x}} c_2|^2 + W(c_1,c_2) \; + \frac{\varrho}{2}\left|(-\nabla_{\boldsymbol{x}}^2)^{-1/2}(c_2-\bar{c}_2)\right|^2 \right\} dV \end{aligned} \tag{4.1}$$

with

$$W(c_1,c_2) = \frac{\left(c_1^2-1\right)^2}{4} + \frac{\left(c_2^2-1\right)^2}{4} + \alpha c_1 c_2 + \beta c_1 c_2^2 + \gamma c_1^2 c_2 \tag{4.2}$$

The Euler-Lagrange system of equations of this functional will yield to the two coupled Cahn-Hilliard equations.

$$\begin{aligned} \tau_1 \dot{c}_1 &= \nabla_{\boldsymbol{x}}^2 \left(\frac{\delta F}{\delta c_1} \right) \\ &= -\nabla_{\boldsymbol{x}}^2 \left\{ \epsilon_1^2 \nabla_{\boldsymbol{x}}^2 c_1 + (1-c_1)(1+c_1)c_1 - \alpha c_2 - \beta c_2^2 \right\} \end{aligned} \tag{4.3}$$

Notice that Equation (4.4) is the Cahn-Hilliard-Oono eqaution since it has $\varrho(c_2 - \bar{c}_2)$ term.

$$\begin{aligned}\tau_2 \dot{c}_2 &= \nabla_{\boldsymbol{x}}^2 \left(\frac{\delta F}{\delta c_2} \right) \\ &= -\nabla_{\boldsymbol{x}}^2 \left\{ \epsilon_2^2 \nabla_{\boldsymbol{x}}^2 c_2 + (1 - c_2)(1 + c_2)c_2 - \alpha c_1 - 2\beta c_1 c_2 \right\} \\ &- \varrho(c_2 - \bar{c}_2)\end{aligned} \tag{4.4}$$

4.1.1 Initial Boundary-Value Problem

Here initial boundary value problem is stated. We give a brief description of the model. The system consists of a copolymer and a homopolymer mixture. Particularly, there exist two different phase separations. In other words, we make patterns for both micro and macro phases. The copolymer and homopolymer mixture form a macrophase. $c_1 \in [-1, 1]$ field shows the macrophase pattern. The value of the c_1 that is close to -1 and 1 states the homopolymer-rich mixture and the copolymer-rich mixture, respectively. The microphase separation is inside the copolymer among its two components (say polymer block A and polymer block B), and it is represented by $c_2 \in [-1, 1]$ field. Similarly, the value of the c_2 that is close to -1 and 1 indicates A polymer block rich mixture and B polymer block rich mixture, respectively. The representative figure for both c_1 and c_2 fields is illustrated in Figure 4.1.

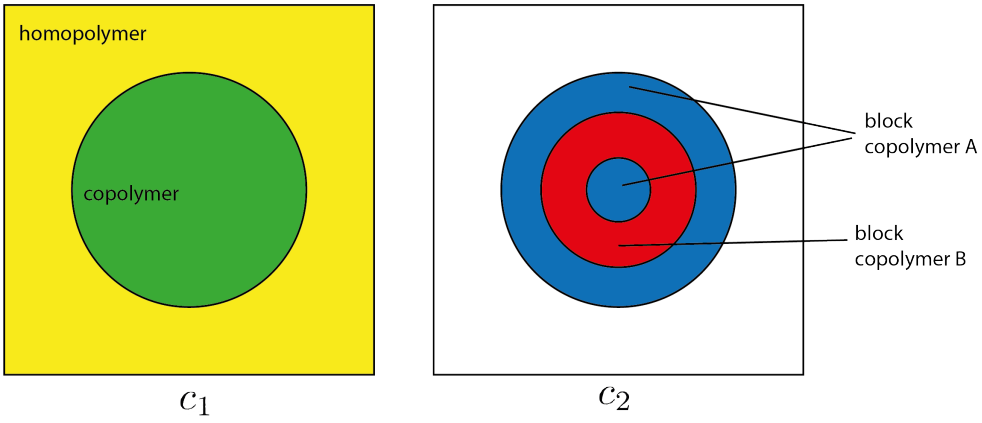

Figure 4.1: Illustration for c_1 and c_2 fields. The yellow and green regions represent the homopolymer and copolymer, respectively. The blue and red regions inside the copolymer represent the block copolymer A and B, respectively.

We investigate the problem with homogeneous Neumann boundary conditions.

$$
\begin{aligned}
\tau_1 \dot{c}_1 &= -\nabla_{\boldsymbol{x}}^2 \left\{ \epsilon_1^2 \nabla_{\boldsymbol{x}}^2 c_1 + f_1(c_1, c_2) \right\} && \text{in } \mathcal{B} \times [0, T] \\
\tau_2 \dot{c}_2 &= -\nabla_{\boldsymbol{x}}^2 \left\{ \epsilon_2^2 \nabla_{\boldsymbol{x}}^2 c_2 + f_2(c_1, c_2) \right\} - \varrho(c_2 - \bar{c}_2) && \text{in } \mathcal{B} \times [0, T] \\
c_1(\boldsymbol{x}, 0) &= c_{1,0} && \text{in } \mathcal{B}, \\
c_2(\boldsymbol{x}, 0) &= c_{2,0} && \text{in } \mathcal{B}, \\
\nabla_{\boldsymbol{x}} c_1 \cdot \mathbf{n} &= \nabla_{\boldsymbol{x}} \left\{ \epsilon_1^2 \nabla_{\boldsymbol{x}}^2 c_1 + f_1(c_1, c_2) \right\} \cdot \mathbf{n} = 0 && \text{on } \partial\mathcal{B} \times [0, T] \\
\nabla_{\boldsymbol{x}} c_2 \cdot \mathbf{n} &= \nabla_{\boldsymbol{x}} \left\{ \epsilon_2^2 \nabla_{\boldsymbol{x}}^2 c_2 + f_2(c_1, c_2) \right\} \cdot \mathbf{n} = 0 && \text{on } \partial\mathcal{B} \times [0, T]
\end{aligned}
\tag{4.5}
$$

with

$$
\begin{aligned}
f_1(c_1, c_2) &= (1 - c_1)(1 + c_1)c_1 - \alpha c_2 - \beta c_2^2 \\
f_2(c_1, c_2) &= (1 - c_2)(1 + c_2)c_2 - \alpha c_1 - 2\beta c_1 c_2
\end{aligned}
\tag{4.6}
$$

τ_1, τ_2 are the time constants to control the speed of the evolution of c_1 and c_2. In other words, a smaller value will lead to faster evolution. ϵ_1, ϵ_2 parameters are related to thickness of the interface for each c_1 and c_2 field. The parameter ϱ controls the bond in the copolymer. That is, it is related to bond between polymer block A and polymer block B. It deals with nonlocal interactions. $\bar{c}_2$ is the mass ratio between two polymers. α, β, and γ are the coefficients in the free energy density function.

$$
\bar{c}_2 = \frac{1}{|\mathcal{B}|} \int_{\mathcal{B}} c_2 dV = \text{ constant} \tag{4.7}
$$

μ_1 and μ_2 are defined as the chemical potentials in order to split the Cahn-Hilliard

equations. Therefore, we obtain the problem as follows.

$$
\begin{aligned}
&\tau_1 \dot{c}_1 = -\nabla^2_{\boldsymbol{x}} \mu_1 && \text{in } \mathcal{B} \times [0,T] \\
&\mu_1 = \epsilon_1^2 \nabla^2_{\boldsymbol{x}} c_1 + f_1(c_1) && \text{in } \mathcal{B} \times [0,T] \\
&\tau_2 \dot{c}_2 = -\nabla^2_{\boldsymbol{x}} \mu_2 - \varrho(c_2 - \bar{c_2}) && \text{in } \mathcal{B} \times [0,T], \\
&\mu_2 = \epsilon_2^2 \nabla^2_{\boldsymbol{x}} c_2 + f_2(c_2) && \text{in } \mathcal{B} \times [0,T], \\
&c_1(\boldsymbol{x},0) = c_{1,0} && \text{in } \mathcal{B}, \\
&c_2(\boldsymbol{x},0) = c_{2,0} && \text{in } \mathcal{B}, \\
&\nabla_{\boldsymbol{x}} c_1 \cdot \mathbf{n} = \nabla_{\boldsymbol{x}} c_2 \cdot \mathbf{n} = \nabla_{\boldsymbol{x}} \mu_1 \cdot \mathbf{n} = \nabla_{\boldsymbol{x}} \mu_2 \cdot \mathbf{n} = 0 && \text{on } \partial\mathcal{B} \times [0,T]
\end{aligned}
\tag{4.8}
$$

with

$$
\begin{aligned}
f_1(c_1, c_2) &= (1 - c_1)(1 + c_1)c_1 - \alpha c_2 - \beta c_2^2 \\
f_2(c_1, c_2) &= (1 - c_2)(1 + c_2)c_2 - \alpha c_1 - 2\beta c_1 c_2
\end{aligned}
\tag{4.9}
$$

4.1.2 Numerical Model Simulations

To solve the coupled problem with the finite element method, we need a weak form of the problem.

Weak Form of Coupled Cahn-Hilliard equations

$$
\begin{aligned}
\int_{\mathcal{B}} \tau_1 \dot{c}_1 \theta dV &= \int_{\mathcal{B}} \nabla_{\boldsymbol{x}} \mu_1 \cdot \nabla_{\boldsymbol{x}} \theta dV \\
\int_{\mathcal{B}} \mu_1 \eta dV &= \int_{\mathcal{B}} \left\{ -\epsilon_1^2 \nabla_{\boldsymbol{x}} c_1 \cdot \nabla_{\boldsymbol{x}} \eta + f_1(c_1, c_2)\eta \right\} dV \\
\int_{\mathcal{B}} \tau_2 \dot{c}_2 \vartheta dV &= \int_{\mathcal{B}} \left\{ \nabla_{\boldsymbol{x}} \mu_2 \cdot \nabla_{\boldsymbol{x}} \vartheta - \varrho \left(c_2 - \bar{c}_2 \right) \vartheta \right\} dV \\
\int_{\mathcal{B}} \mu_2 \zeta dV &= \int_{\mathcal{B}} \left\{ -\epsilon_2^2 \nabla_{\boldsymbol{x}} v \cdot \nabla_{\boldsymbol{x}} \zeta + f_2(c_1, c_2)\zeta \right\} dV \\
c_1(\boldsymbol{x}, 0) &= c_{1,0} \\
c_2(\boldsymbol{x}, 0) &= c_{2,0}
\end{aligned}
\tag{4.10}
$$

where θ, η, ϑ, and ζ are the test functions for order the parameters and their chemical potentials.

4.1.2.1 The First Example

The first model is reproduced example in [52]. The values of parameters are presented in Table 4.1 for this example. The solutions are presented in Figure 4.2.

Table 4.1: Parameters of Self-assembly Model 1

No.	Parameter	Name	Value
1	$\mathcal{B}$	Domain	$[0,1] \times [0,1]$
2	ϵ_1	Interface parameter	0.05
3	ϵ_2	Interface parameter	0.05
4	τ_1	Time coefficient	1
5	τ_2	Time coefficient	10
6	α	Surface energy coefficient	0.04
7	β	Surface energy coefficient	-0.9
8	γ	Surface energy coefficient	0
9	ϱ	Long range interaction coefficient	100
10	Δt	Time step	1×10^{-4}
11	$c_{1,0}$	Initial condition for c_1	$\sin 10xy$
12	$c_{2,0}$	Initial condition for c_2	$\cos 10(x-y)xy$
13	T_{final}	Final time	0.1

In the first example, we validate our solution because we obtain the same results in [52]. Figure 4.2c shows macrophase separation. The red and blue colors indicate the copolymer and the homopolymer, respectively. Figure 4.2d demonstrates the pattern in the copolymer.

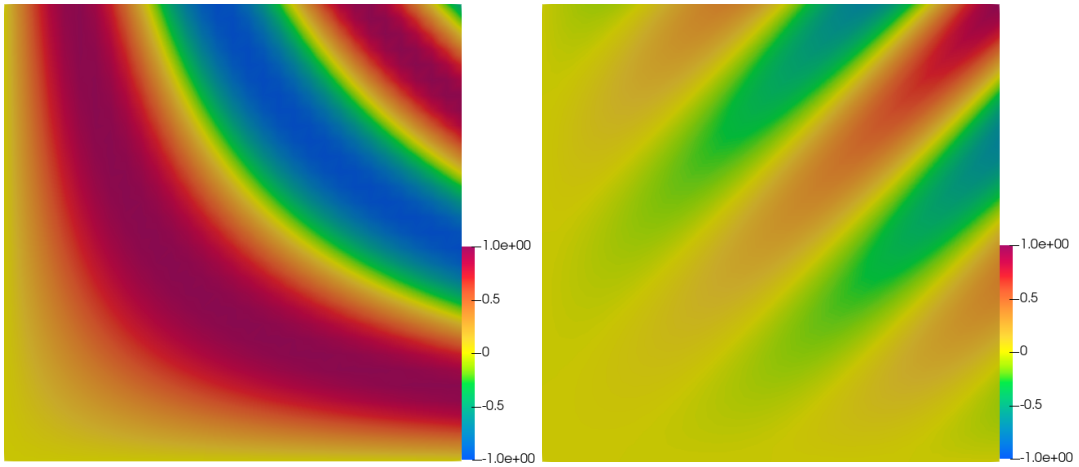

(a) $c_{1,0}$ (b) $c_{2,0}$

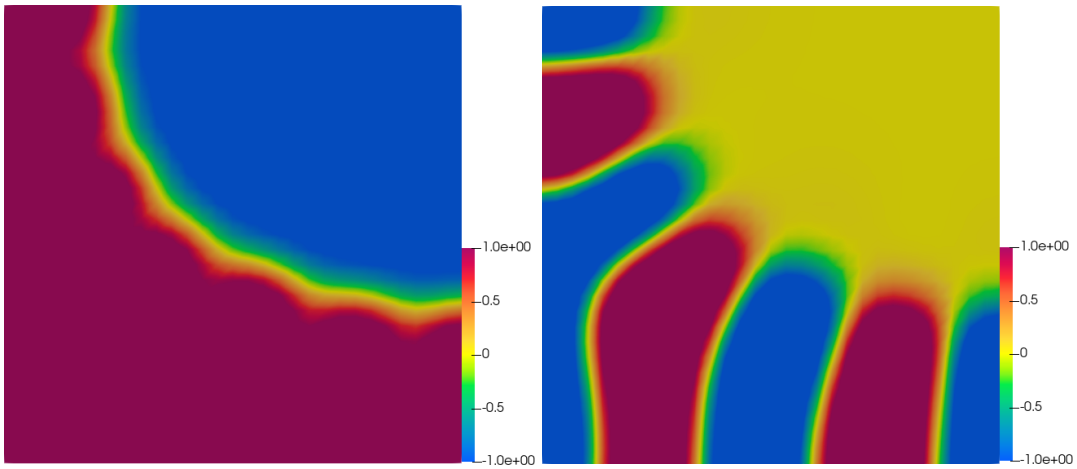

(c) c_1 at $t = 10$ (d) c_2 at $t = 10$

Figure 4.2: Solution of the coupled Cahn-Hilliard equations are presented. c_1 field shows the macrophase separation and c_2 field shows the microphase separation.

4.1.2.2 Onion Shape Example

Here we will solve the coupled Cahn-Hilliard equations with given parameters in Table 4.2. Onion shape is produced from the striped pattern. The initial condition for both c_1 and c_2 field are presented in Equations (4.11) and (4.12). The solutions of c_1

and c_2 fields are depicted in Figure 4.4 and 4.3 respectively.

$$c_{1,0} = \begin{cases} 0.6 & \text{for } (x-0.5)^2 + (y-0.5)^2 \leq 0.125 \\ -0.6 & \text{otherwise} \end{cases} \tag{4.11}$$

$$c_{2,0} = \begin{cases} \sin 15\pi x & \text{for } (x-0.5)^2 + (y-0.5)^2 \leq 0.125 \\ -0.2 & \text{otherwise} \end{cases} \tag{4.12}$$

Table 4.2: Parameters of Self-assembly Model 2

No.	Parameter	Name	Value
1	$\mathcal{B}$	Domain	$[0,1] \times [0,1]$
2	ϵ_1	Interface parameter	0.025
3	ϵ_2	Interface parameter	0.025
4	τ_1	Time coefficient	1
5	τ_2	Time coefficient	10
6	α	Surface energy coefficient	0.3
7	β	Surface energy coefficient	-0.8
8	γ	Surface energy coefficient	0
9	ϱ	Long range interaction coefficient	100
10	Δt	Time step	5×10^{-4}
11	T_{final}	Final time	1

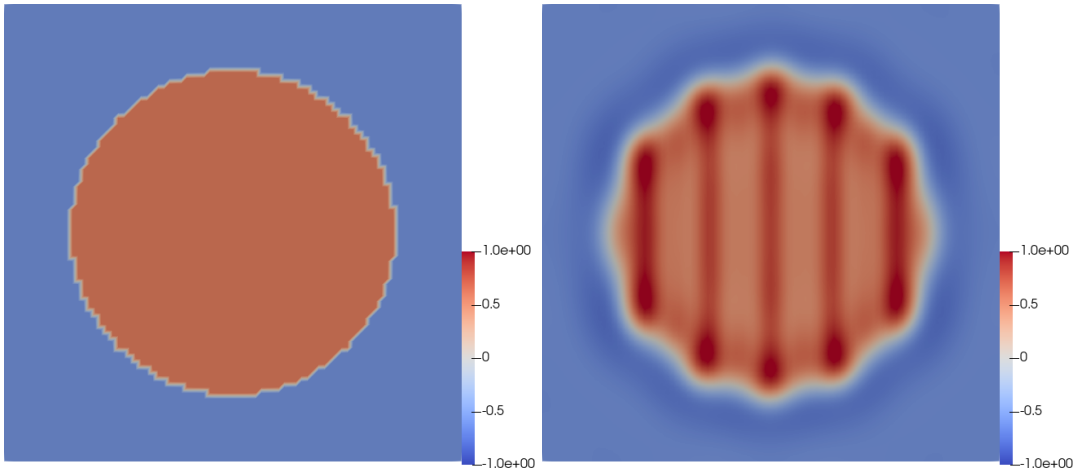

(a) c_1 at $t = 0$ (b) c_1 at $t = 0.001$

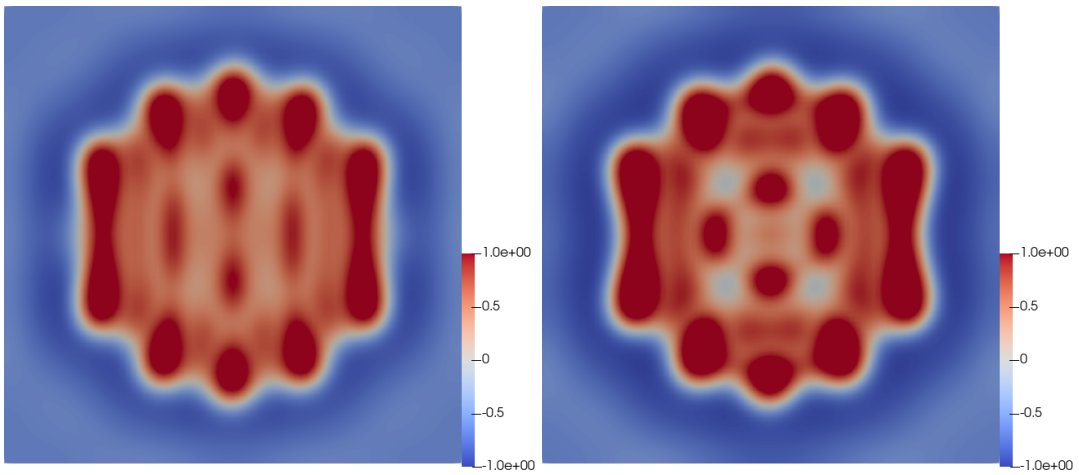

(c) c_1 at $t = 0.003$ (d) c_1 at $t = 0.005$

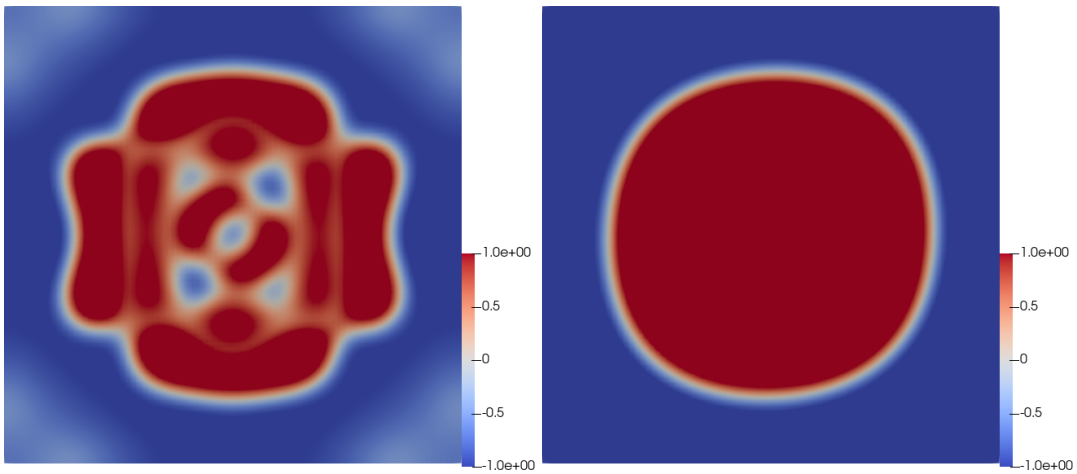

(e) c_1 at $t = 0.01$ (f) c_1 at $t = 1$

Figure 4.3: Evolution of c_1 field for onion shape production

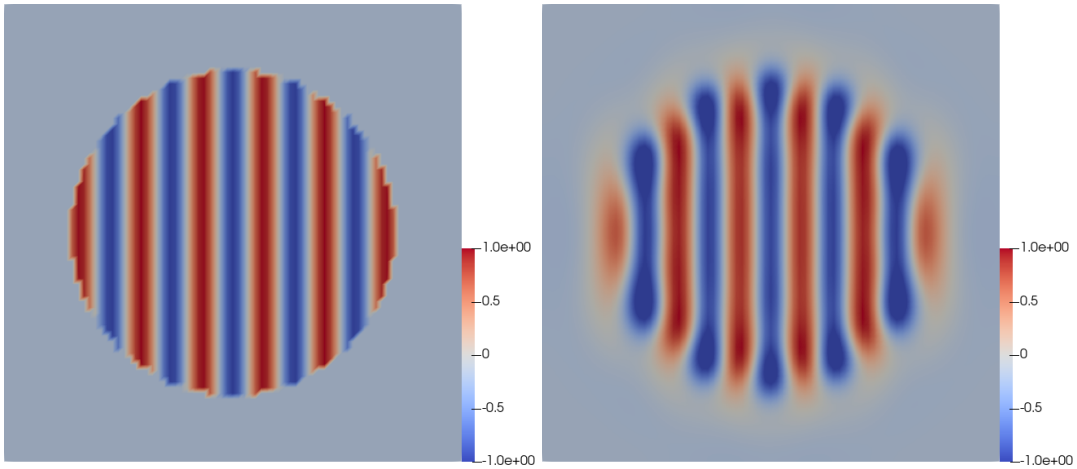

(a) c_2 at $t = 0$ (b) c_2 at $t = 0.001$

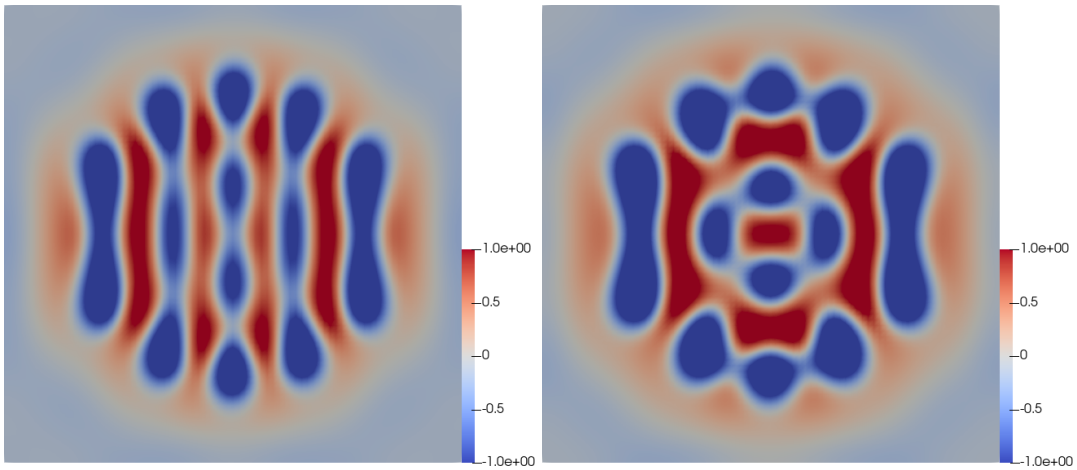

(c) c_2 at $t = 0.003$ (d) c_2 at $t = 0.005$

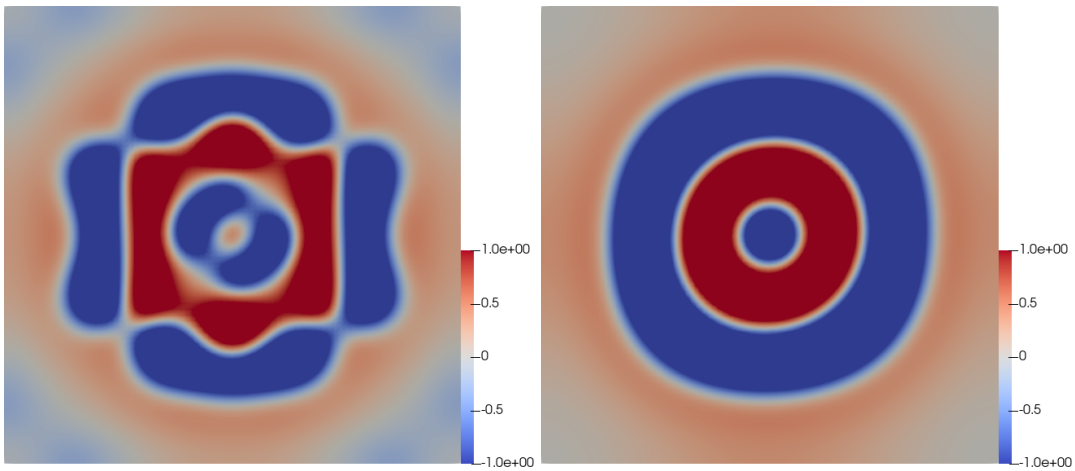

(e) c_2 at $t = 0.01$ (f) c_2 at $t = 1$

Figure 4.4: Evolution of c_2 field for onion shape production

Here, we solve the onion shape example in three-dimensional geometry. The same parameters are used in the two-dimensional example, which can be seen in Table 4.2. The following form of initial conditions is used in the three-dimensional example.

$$c_{1,0} = \begin{cases} 0.6 & \text{for } (x-0.5)^2 + (y-0.5)^2 + (z-0.5)^2 \leq 0.125 \\ -0.6 & \text{otherwise} \end{cases} \tag{4.13}$$

$$c_{2,0} = \begin{cases} \sin 15\pi x & \text{for } (x-0.5)^2 + (y-0.5)^2 + (z-0.5)^2 \leq 0.125 \\ -0.2 & \text{otherwise} \end{cases} \tag{4.14}$$

The solution of the 3D onion shape example is shown in Figures 4.5 - 4.9. In the visualization of the solution, the domain is cut in half to display better.

For both 2D and 3D onion shape examples, the transformation of the block copolymers from striped lamellae into an onionlike sphere is modeled through the coupled Cahn-Hilliard equations like in [39].

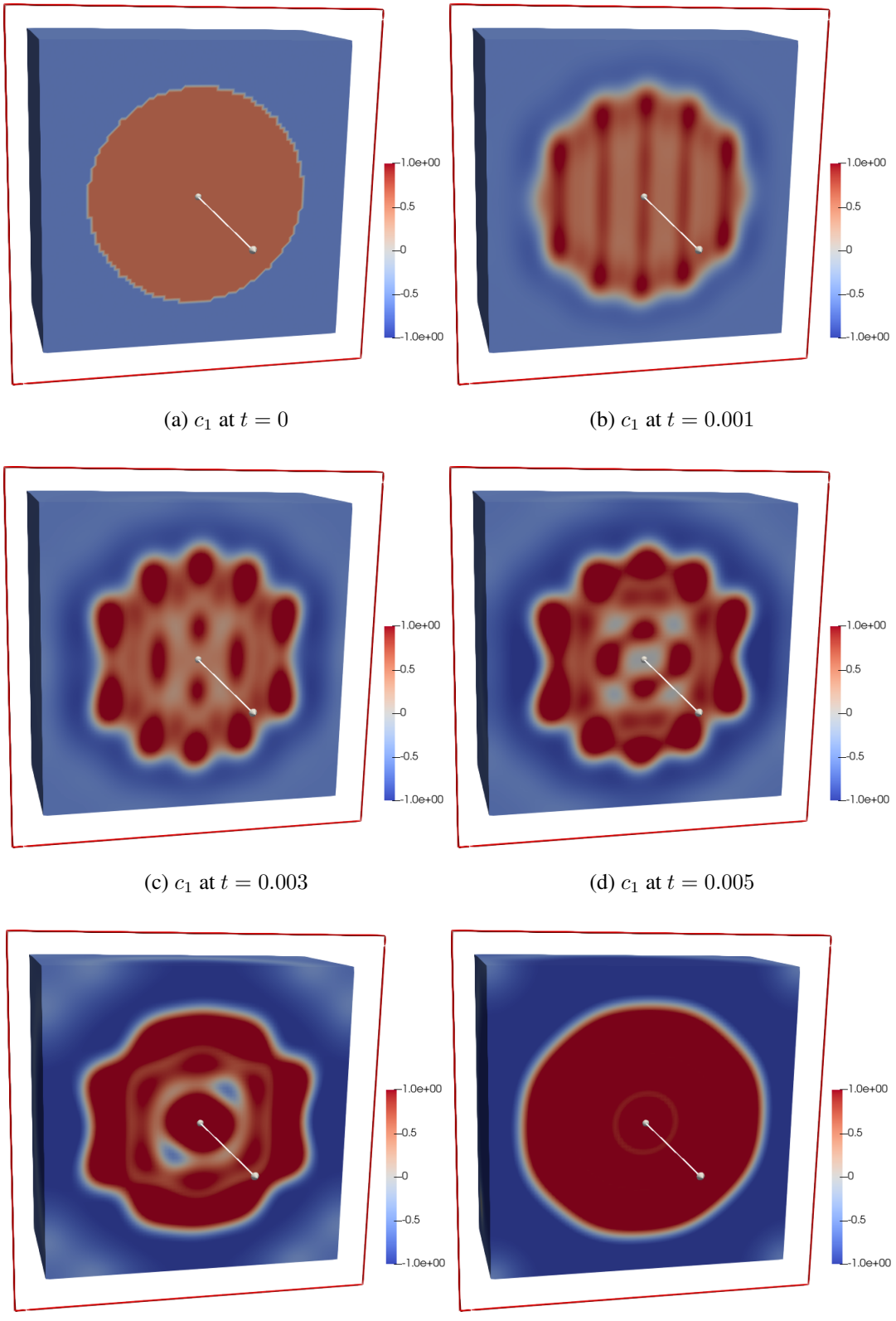

(a) c_1 at $t = 0$

(b) c_1 at $t = 0.001$

(c) c_1 at $t = 0.003$

(d) c_1 at $t = 0.005$

(e) c_1 at $t = 0.01$

(f) c_1 at $t = 0.25$

Figure 4.5: Evolution of c_1 field for 3D onion shape production example. The color indicates the c_1 field.

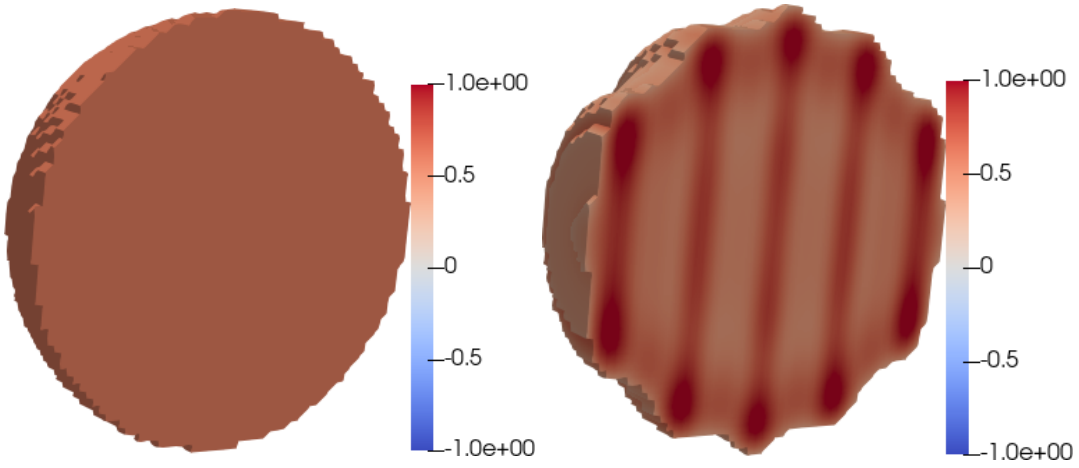

(a) c_1 at $t = 0$

(b) c_1 at $t = 0.001$

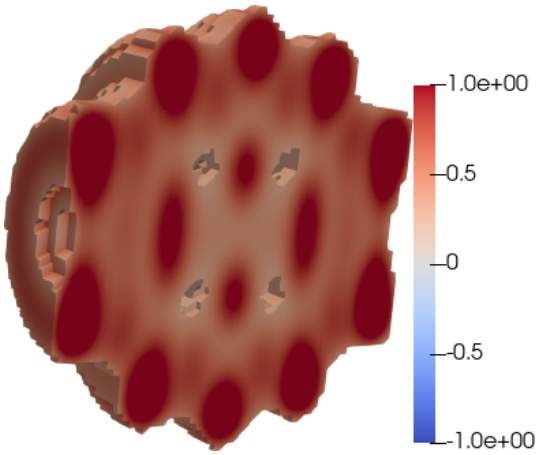

(c) c_1 at $t = 0.003$

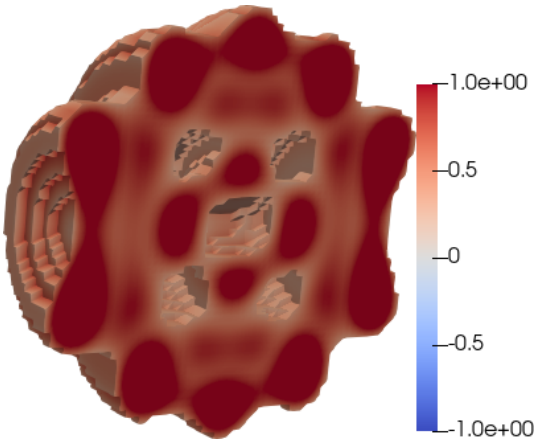

(d) c_1 at $t = 0.005$

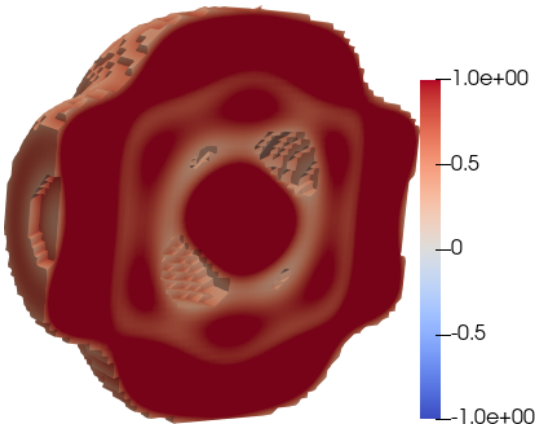

(e) c_1 at $t = 0.01$

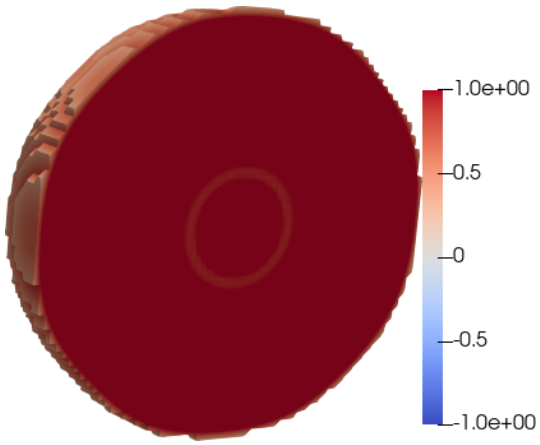

(f) c_1 at $t = 0.25$

Figure 4.6: Evolution of copolymer phases for 3D onion shape production. The copolymer consists of block polymer A and B. The color indicates the c_1 field.

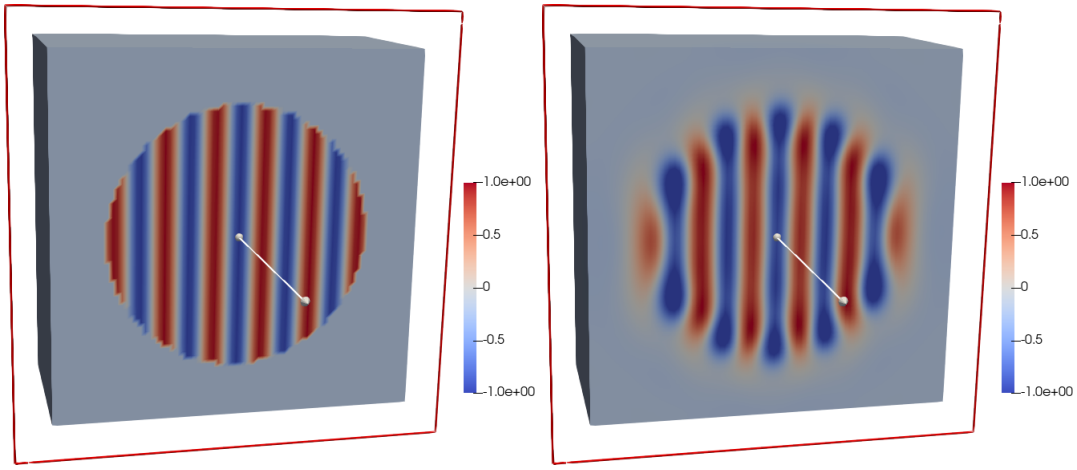

(a) c_2 at $t = 0$ (b) c_2 at $t = 0.001$

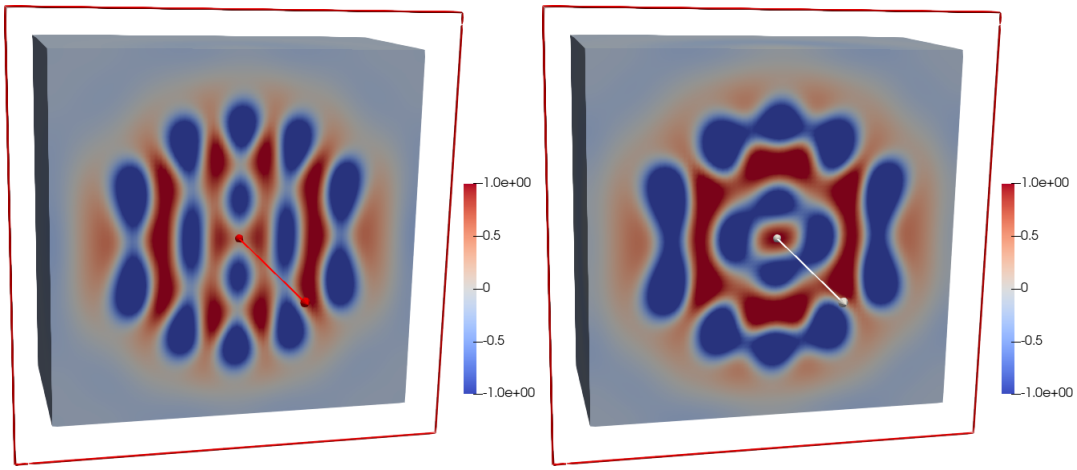

(c) c_2 at $t = 0.003$ (d) c_2 at $t = 0.005$

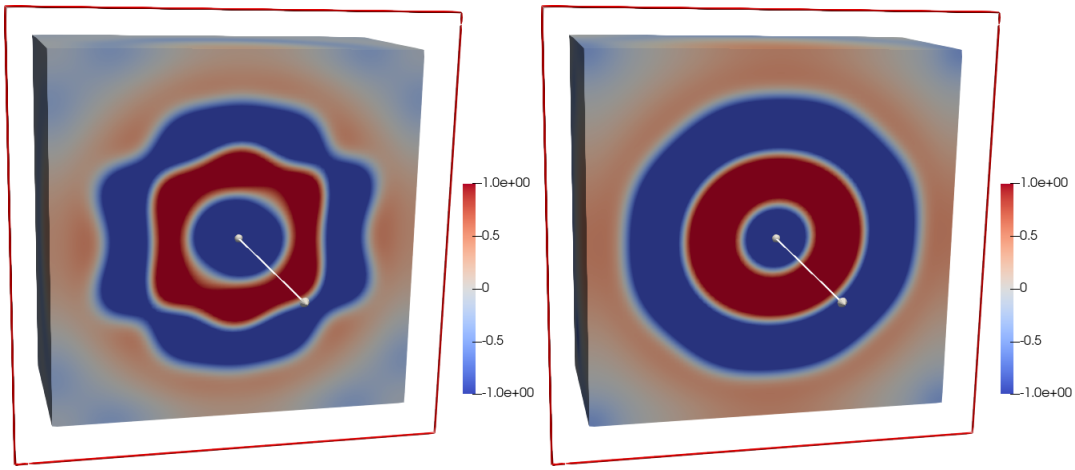

(e) c_2 at $t = 0.01$ (f) c_2 at $t = 0.025$

Figure 4.7: Evolution of c_2 field for 3D onion shape production. The color indicates the c_2 field.

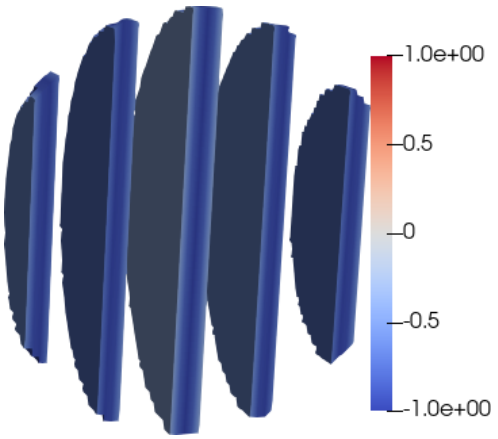

(a) Blue phase at $t = 0$

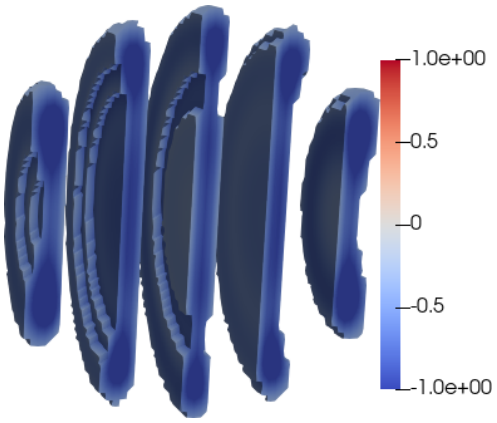

(b) Blue phase at $t = 0.001$

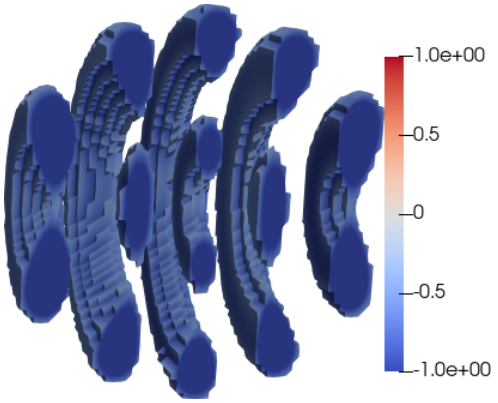

(c) Blue phase at $t = 0.003$

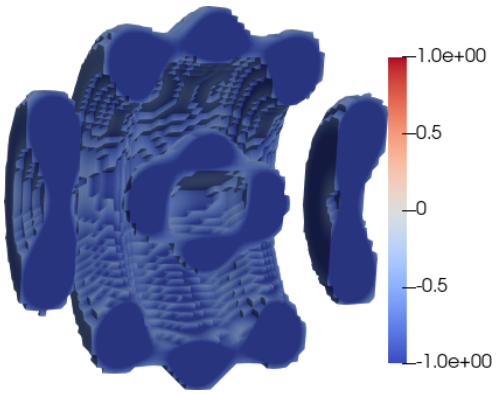

(d) Blue phase at $t = 0.005$

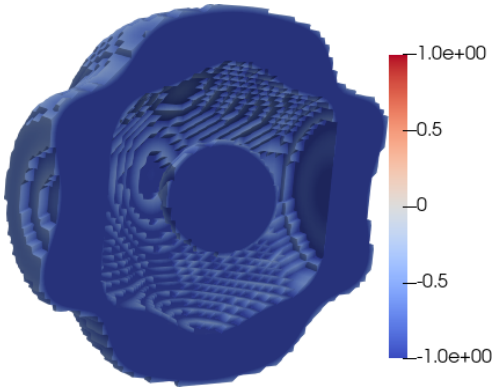

(e) Blue phase at $t = 0.01$

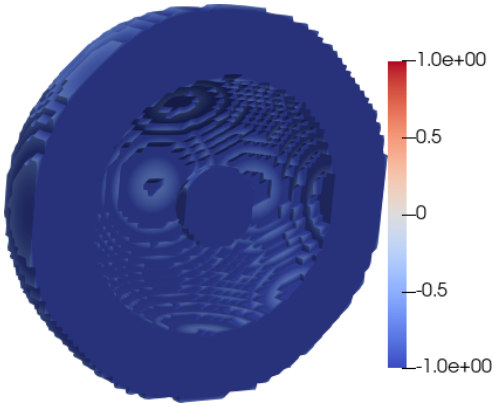

(f) Blue phase at $t = 0.025$

Figure 4.8: Evolution of blue phase in the copolymer. The blue phase and red phase in Figure 4.6 depict the onion shape formation. The color indicates the c_2 field.

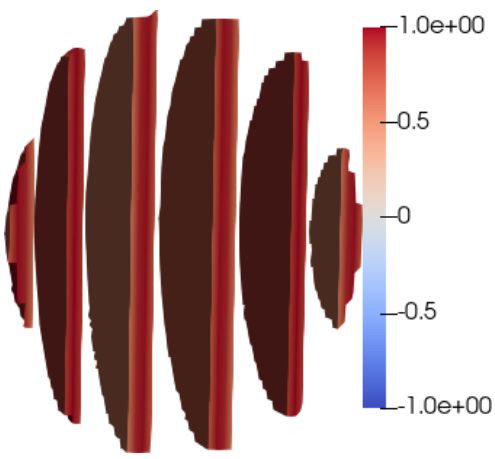

(a) Red phase at $t = 0$

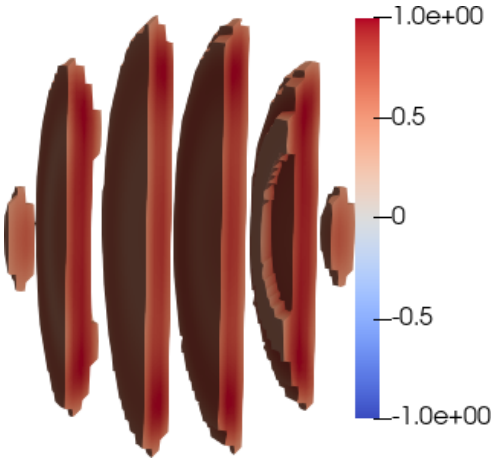

(b) Red phase at $t = 0.001$

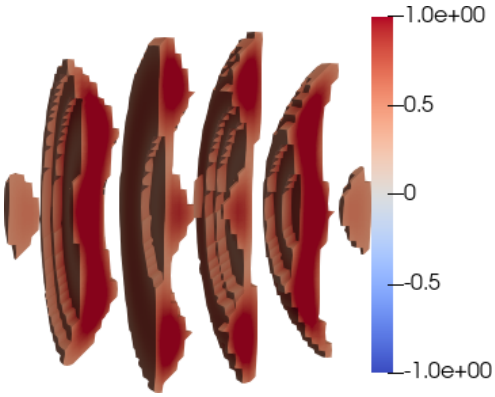

(c) Red phase at $t = 0.003$

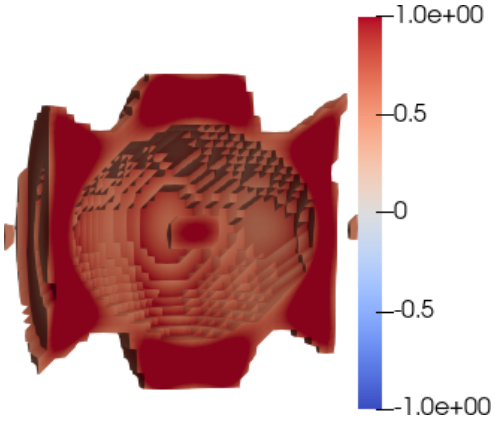

(d) Red phase at $t = 0.005$

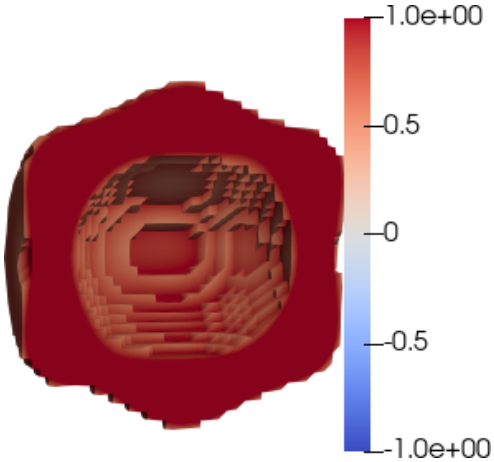

(e) Red phase at $t = 0.01$

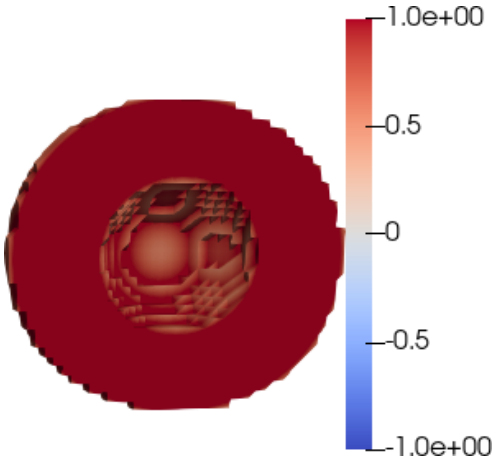

(f) Red phase at $t = 0.025$

Figure 4.9: Evolution of red phase in the copolymer. The combination of Figures 4.8 and 4.9 gives Figure 4.6. The color indicates the c_2 field.

CHAPTER 5

SELF-ASSEMBLY COUPLED WITH MECHANICS

This chapter contributes to the literature by combining self-assembly and mechanics. In other words, we solve two Cahn-Hilliard equations coupled with finite viscoelasticity.

5.1 Coupling of Self Assembly and Finite Viscoelasticity

In Chapter 3, we have investigated the coupling of the Cahn-Hilliard equation and the mechanics. In Chapter 4, we have studied the coupling of two Cahn-Hilliard equations and modeled self-assembly.

In modeling of self-assembly, we have two Cahn-Hilliard equations for both macrophase and microphase separation. Here, for microphase separation, we solve the Cahn-Hilliard equation with finite viscoelasticity using the procedure that is presented in Chapter 3.

Equations (3.59), (3.61) and (3.62) are used for the deformation gradient split. The following energy storage function is used.

$$W(\boldsymbol{F}, c_1, c_2) = W_{mech}\left(\boldsymbol{F}^{mech}(\boldsymbol{F}, c_2)\right) + W_{che}(c_1, c_2) \tag{5.1}$$

with

$$
\begin{aligned}
W_{che}(c_1, c_2) = \frac{\left(c_1^2 - 1\right)^2}{4} + \frac{\left(c_2^2 - 1\right)^2}{4} + \alpha c_1 c_2 + \beta c_1 c_2^2 + \gamma c_1^2 c_2 \\
W_{mech}\left(\boldsymbol{F}^{mech}(\boldsymbol{F}, c_2)\right) = W_{vol}(J) + W_{iso}\left(\bar{\boldsymbol{C}}\right)
\end{aligned}
\tag{5.2}
$$

and

$$
\begin{aligned}
W_{vol}(J_{mech}) &= \tfrac{1}{2}\kappa\left(\tfrac{1}{2}\left({J_{mech}}^2 - 1\right) - \ln J_{mech}\right), \\
W_{iso}\left(\bar{\boldsymbol{C}}\right) &= \tfrac{1}{2}\mu(\bar{\boldsymbol{C}} : \mathbf{1} - 3) = \tfrac{1}{2}\mu(\mathrm{tr}[\bar{\boldsymbol{C}}] - 3)
\end{aligned}
\tag{5.3}
$$

The coupling of the Cahn-Hilliard equation and mechanics is known. Now we can combine this coupling with self-assembly, which is described in Chapter 4. The following set of partial differential equations are considered.

$$
\begin{aligned}
&\tau_1 \dot{c}_1 = -\nabla_{\boldsymbol{x}}^2 \mu_1 && \text{in } \mathcal{B} \times [0, T] \\
&\mu_1 = \epsilon_1^2 \nabla_{\boldsymbol{x}}^2 c_1 + f_1(c_1, c_2) && \text{in } \mathcal{B} \times [0, T] \\
&\tau_2 \dot{c}_2 = -\nabla_{\boldsymbol{x}}^2 \mu_2 - \varrho(c_2 - \bar{c_2}) && \text{in } \mathcal{B} \times [0, T], \\
&\mu_2 = \epsilon_2^2 \nabla_{\boldsymbol{x}}^2 c_2 + f_2(c_1, c_2) && \text{in } \mathcal{B} \times [0, T], \\
&\mathrm{Div}[\boldsymbol{P}] + \bar{\boldsymbol{\gamma}} = \mathbf{0} && \text{in } \mathcal{B} \times [0, T] \\
&c_1(\boldsymbol{x}, 0) = c_{1,0} && \text{in } \mathcal{B}, \\
&c_2(\boldsymbol{x}, 0) = c_{2,0} && \text{in } \mathcal{B}, \\
&\boldsymbol{u}(\boldsymbol{x}, 0) = c_{2,0} && \text{in } \mathcal{B}, \\
&\boldsymbol{\varphi} = \bar{\boldsymbol{\varphi}}(\boldsymbol{X}, t) \text{ on } \partial\mathcal{B}_0^{\varphi} \quad \text{and} \quad \boldsymbol{P}\mathbf{n}_0 = \bar{\boldsymbol{t}}(x, t) \text{ on } \partial\mathcal{B}_0^{t} \\
&\nabla_{\boldsymbol{x}} c_1 \cdot \mathbf{n} = \nabla_{\boldsymbol{x}} c_2 \cdot \mathbf{n} = \nabla_{\boldsymbol{x}} \mu_1 \cdot \mathbf{n} = \nabla_{\boldsymbol{x}} \mu_2 \cdot \mathbf{n} = 0 && \text{on } \partial\mathcal{B} \times [0, T].
\end{aligned}
\tag{5.4}
$$

with

$$
\begin{aligned}
f_1(c_1, c_2) &= (1 - c_1)(1 + c_1)c_1 - \alpha c_2 - \beta c_2^2 \\
f_2(c_1, c_2) &= (1 - c_2)(1 + c_2)c_2 - \alpha c_1 - 2\beta c_1 c_2 + \Omega J_c^{-1} p
\end{aligned}
\tag{5.5}
$$

where $\boldsymbol{P}$ is defined in Equation (3.65)

5.1.1 Numerical Simulation

To solve the coupled problem with the finite element method, we need a weak form of the problem.

Weak Form of the Problem:

$$
\begin{aligned}
\int_{\mathcal{B}} \tau_1 \dot{c}_1 \theta dV &= \int_{\mathcal{B}} \nabla_{\boldsymbol{x}} \mu_1 \cdot \nabla_{\boldsymbol{x}} \theta dV \\
\int_{\mathcal{B}} \mu_1 \eta dV &= \int_{\mathcal{B}} \left\{ -\epsilon_1^2 \nabla_{\boldsymbol{x}} c_1 \cdot \nabla_{\boldsymbol{x}} \eta + f_1(c_1, c_2)\eta \right\} dV \\
\int_{\mathcal{B}} \tau_2 \dot{c}_2 \vartheta dV &= \int_{\mathcal{B}} \left\{ \nabla_{\boldsymbol{x}} \mu_2 \cdot \nabla_{\boldsymbol{x}} \vartheta - \varrho \left(c_2 - \bar{c}_2 \right) \vartheta \right\} dV \\
\int_{\mathcal{B}} \mu_2 \zeta dV &= \int_{\mathcal{B}} \left\{ -\epsilon_2^2 \nabla_{\boldsymbol{x}} v \cdot \nabla_{\boldsymbol{x}} \zeta + f_2(c_1, c_2)\zeta \right\} dV \\
\int_{\mathcal{B}} \boldsymbol{P} : \nabla_{\boldsymbol{x}} \boldsymbol{q} dV &= \int_{\mathcal{B}} \bar{\boldsymbol{\gamma}} \cdot \boldsymbol{q} dV \\
c_1(\boldsymbol{x}, 0) &= c_{1,0} \\
c_2(\boldsymbol{x}, 0) &= c_{2,0}
\end{aligned}
\tag{5.6}
$$

with

$$
\int_{\mathcal{B}} \dot{\bar{\boldsymbol{Q}}} : \boldsymbol{U} dV + \int_{\mathcal{B}} \frac{1}{\tau} \bar{\boldsymbol{Q}} : \boldsymbol{U} dV = \int_{\mathcal{B}} \beta \frac{d}{dt} \left(\mathrm{DEV} \left[\bar{\boldsymbol{S}}_{iso}^{e} \right] \right) : \boldsymbol{U} dV \tag{5.7}
$$

where θ, η, ϑ, ζ, $\boldsymbol{q}$ and $\boldsymbol{U}$ are test functions for order parameters, their chemical potentials, deformation field and isochoric viscous overstress field. Values of parameters are presented in Table 5.1.

The initial condition for both c_1 and c_2 field are shown in Figures 5.1a and 5.1a. These parameters and initial conditions are the same as the onion shape example in Chapter 4. Without mechanics effect, we obtained the onion shape. Now we get a different pattern. According to the result, we obtained, considering the effect of the viscoelasticity changes the concentration/order parameter. Solutions of c_1 and c_2 field

are depicted in Figure 5.2 and 5.1 respectively.

$$c_{1,0} = \begin{cases} \sin 15xy & \text{for } (x-0.5)^2 + (y-0.5)^2 \leq 0.125 \\ -0.2 & \text{otherwise} \end{cases} \tag{5.8}$$

$$c_{2,0} = \begin{cases} 0.6 & \text{for } (x-0.5)^2 + (y-0.5)^2 \leq 0.125 \\ -0.6 & \text{otherwise} \end{cases} \tag{5.9}$$

Table 5.1: Parameters of Self-assembly Coupled with Mechanics Model

No.	Parameter	Name	Value
1	$\mathcal{B}$	Domain	$[0,1] \times [0,1]$
2	ϵ_1	Interface parameter	0.025
3	ϵ_2	Interface parameter	0.025
4	τ_1	Time coefficient	1
5	τ_2	Time coefficient	10
6	α	Surface energy coefficient	0.3
7	β	Surface energy coefficient	-0.8
8	γ	Surface energy coefficient	0
9	ϱ	Long range interaction coefficient	100
10	Δt	Time step	5×10^{-4}
11	T_{final}	Final time	1

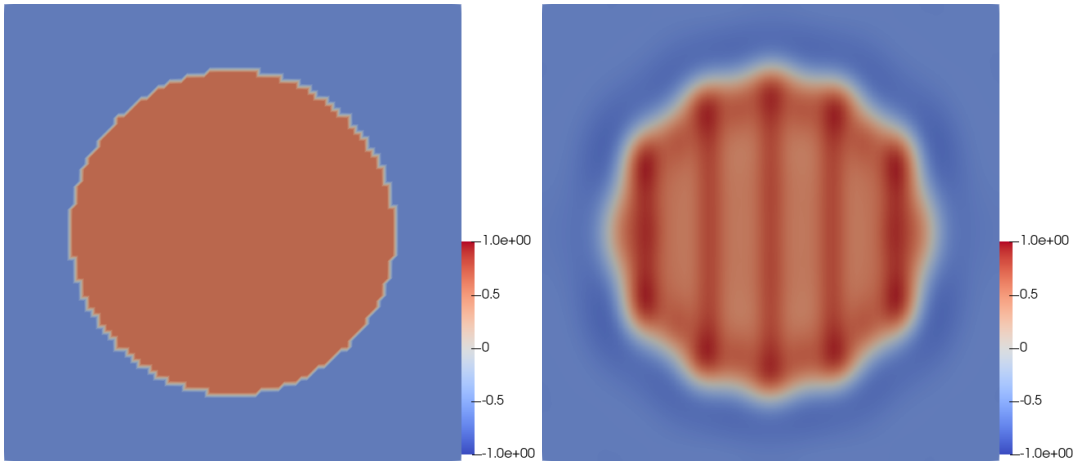

(a) c_1 at $t = 0$ (b) c_1 at $t = 0.001$

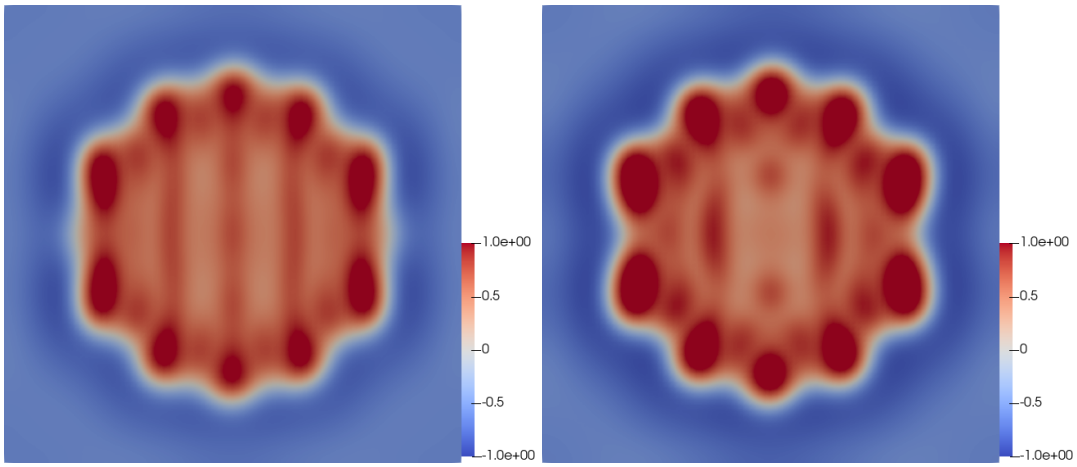

(c) c_1 at $t = 0.003$ (d) c_1 at $t = 0.005$

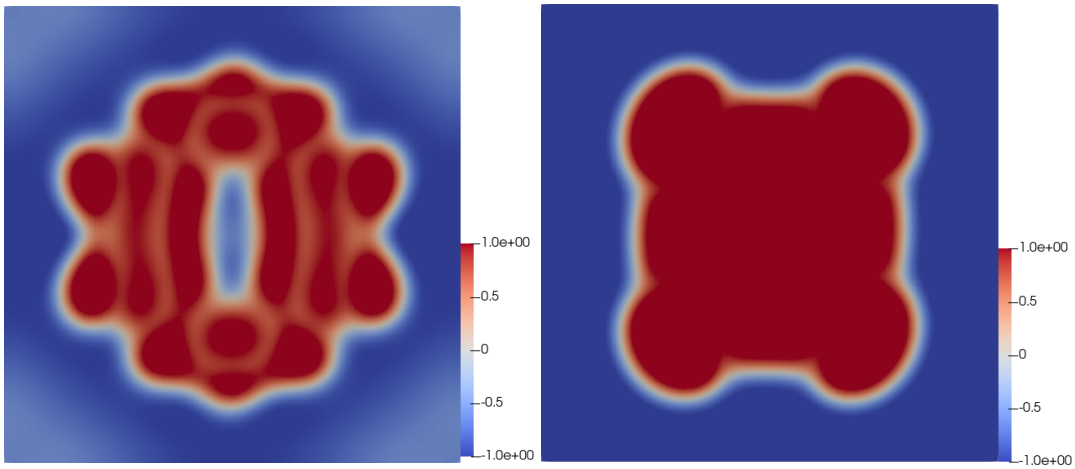

(e) c_1 at $t = 0.01$ (f) c_1 at $t = 1$

Figure 5.1: Evolution of c_1 field for self-assembly model considering finite viscoelasticity

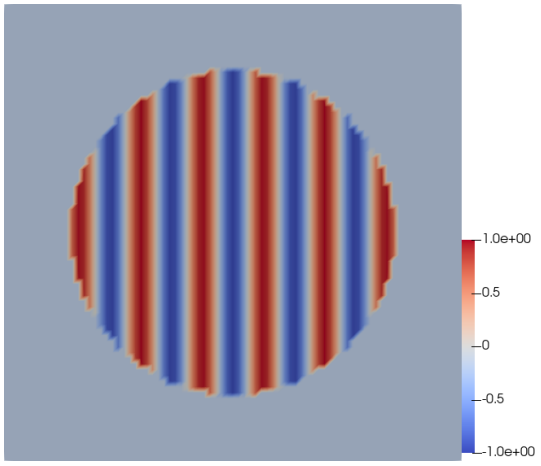

(a) c_2 at $t = 0$

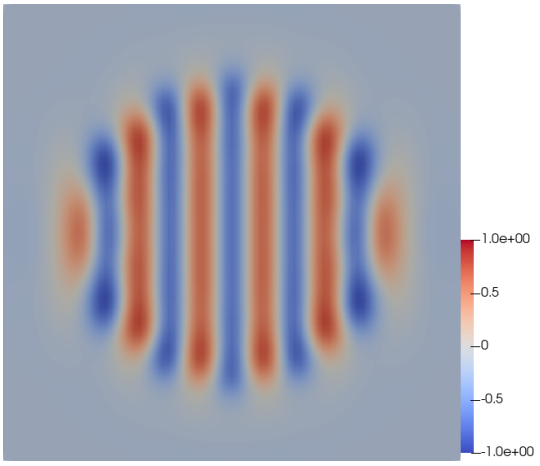

(b) c_2 at $t = 0.001$

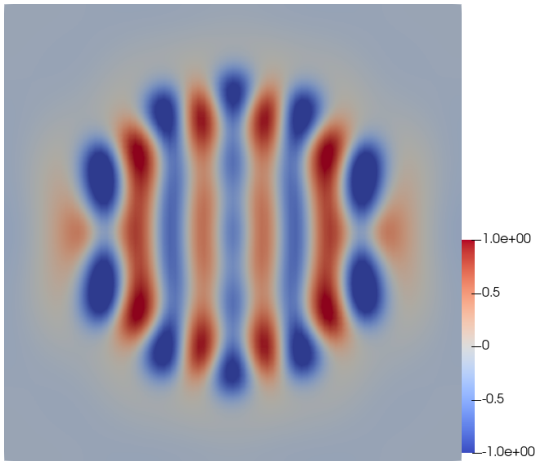

(c) c_2 at $t = 0.003$

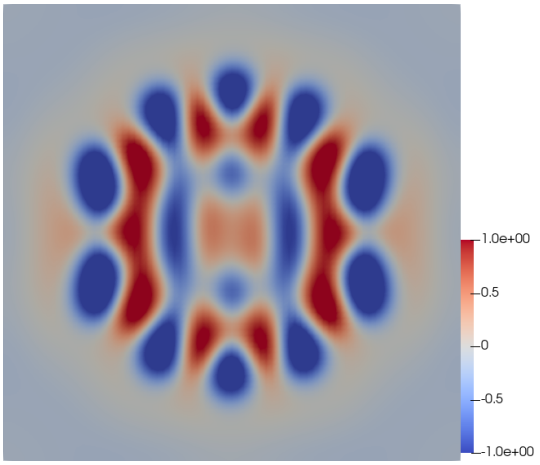

(d) c_2 at $t = 0.005$

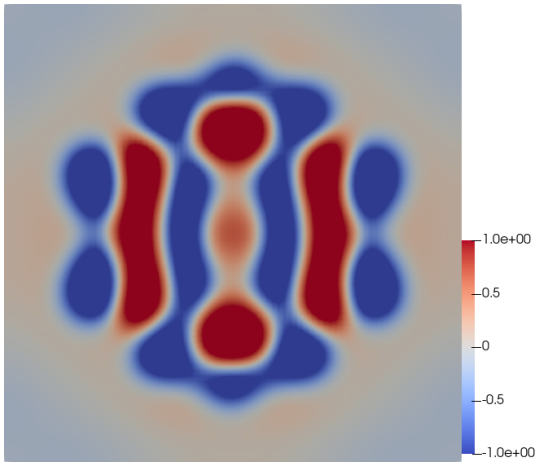

(e) c_2 at $t = 0.01$

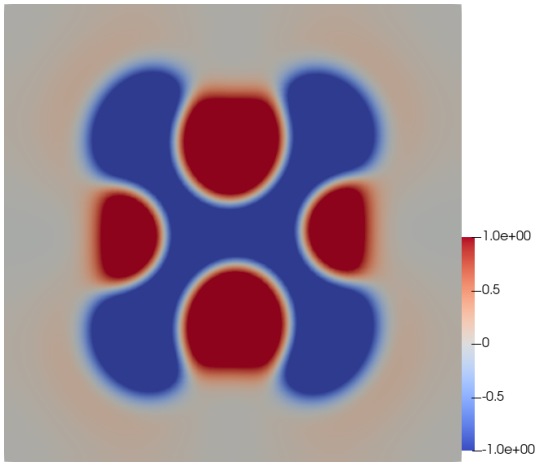

(f) c_2 at $t = 1$

Figure 5.2: Evolution of c_2 field for self-assembly model considering finite viscoelasticity

CHAPTER 6

CONCLUDING REMARKS

In this thesis, the process of self-assembly in deformable bodies was numerically modeled using the finite element method. First, the Cahn-Hilliard equation is investigated. It is solved by using $\mathbf{C}_0$ and $\mathbf{C}_2$ elements separately. Moreover, its variants were studied, such as the Allen-Cahn equation, the Cahn-Hilliard equation with the proliferation and fidelity term, the Cahn-Hilliard-Oono equation, and the sixth-order generalized Cahn-Hilliard equation. Relevant numerical examples were also given for the variants of the Cahn-Hilliard equation. Second, coupling of the Cahn-Hilliard equation with the conservation of linear momentum was examined. In this study, the coupling was done by considering the volumetric deformation and adding an interface stretch term to the storage function. We observed an increase in interface area as a result of the interface stretch term. Furthermore, for the mechanics part, finite elasticity and finite viscoelasticity material behavior were considered. The self-assembly process was modeled by two Cahn-Hilliard equations. One of the Cahn-Hilliard equations was coupled with the conservation of linear momentum equation. Numerous representative numerical examples were presented.

In literature, there are few studies on the coupling of the Cahn-Hilliard equation with mechanics. Those couplings are through volumetric deformation. Here, we also consider an additional stretch term in the storage function, which couples the Cahn-Hilliard equation and mechanics. In literature, the mechanical part is studied as the finite elasticity, but we also studied finite viscoelasticity. To our best knowledge, there are no studies combining the self-assembly process and the mechanical effects at the continuum level. In this respect, this thesis has brought this novelty as well. We observed that the mechanical effects affect the pattern comparing purely chemical and

coupled formulation. Now, we have a tool to model self-assembly considering mechanical effects. We can add more coupling terms to the tool, and it can be calibrated using the experimental data. This tool can be used by a researcher working in the self-assembly area.

6.1 Challenges

The Cahn-Hilliard equation is a highly nonlinear, time-dependent 4th-order partial differential equation. Therefore, to solve it, we should have fine meshes if we use Lagrange finite elements. This increases the time required for simulations. For the model of the self-assembly of the block copolymer, we need to solve at least two Cahn-Hilliard equations together. To decrease cumulative error in the finite element solution, we should have finer meshes and smaller time steps. In addition to this, when we solve two Cahn-Hilliard equations considering the effect of the finite viscoelasticity, we should definitely have finer meshes and smaller time steps. Otherwise, the solution does not converge. This is a time-consuming simulation.

In the modeling of the self-assembly, some of the results that are presented in Chapter 4 are obtained by trial and error since some parameter values are not given in the literature. Furthermore, while coupling self-assembly and mechanics with the terms we added, the coefficient at the beginning of this term was tried to be found by trial and error. Therefore, all the trial error procedures in this study took a lot of time. In this regard, an optimization problem can be written. By optimizing, we can obtain the necessary parameters and initial conditions to obtain a particular pattern.

In addition to these, we do not have the experimental study and data to test and calibrate our model.

6.2 Future Studies

We plan to add different terms such as area stretch with concentration and the curvature of concentration with stretch to the energy storage function in future studies. Those terms couple the deformation fields and the concentration fields as well. Since

we do not have experimental data, perhaps the most important thing is how to determine the coefficient in front of these terms. How do we calibrate the numerical model? Does this coupling explain exactly the underlying physics? These are the questions that need to be answered in the future.

REFERENCES

[1] E. F. Marques and B. F. Silva, "Surfactant self-assembly," *Encyclopedia of Colloid and Interface Science*, p. 1202–1241, 2013.

[2] S. C. Glotzer, "Shape matters," *Nature*, vol. 481, no. 7382, p. 450–452, 2012.

[3] Y. Mai and A. Eisenberg, "Self-assembly of block copolymers," *Chem. Soc. Rev.*, vol. 41, pp. 5969–5985, 2012.

[4] T. Smart, H. Lomas, M. Massignani, M. V. Flores-Merino, L. R. Perez, and G. Battaglia, "Block copolymer nanostructures," *Nano Today*, vol. 3, no. 3, pp. 38–46, 2008.

[5] O. Gang and Y. Zhang, "Shaping phases by phasing shapes," *ACS Nano*, vol. 5, no. 11, p. 8459–8465, 2011.

[6] S. Sacanna, W. T. Irvine, P. M. Chaikin, and D. J. Pine, "Lock and key colloids," *Nature*, vol. 464, no. 7288, p. 575–578, 2010.

[7] P. F. Damasceno, M. Engel, and S. C. Glotzer, "Predictive self-assembly of polyhedra into complex structures," *Science*, vol. 337, no. 6093, pp. 453–457, 2012.

[8] Y. Zhang, F. Lu, D. van der Lelie, and O. Gang, "Continuous phase transformation in nanocube assemblies," *Phys. Rev. Lett.*, vol. 107, p. 135701, Sep 2011.

[9] J. D. Forster, J.-G. Park, M. Mittal, H. Noh, C. F. Schreck, C. S. O'Hern, H. Cao, E. M. Furst, and E. R. Dufresne, "Assembly of optical-scale dumbbells into dense photonic crystals," *ACS Nano*, vol. 5, no. 8, p. 6695–6700, 2011.

[10] T. D. Nguyen, E. Jankowski, and S. C. Glotzer, "Self-assembly and reconfigurability of shape-shifting particles," *ACS Nano*, vol. 5, no. 11, p. 8892–8903, 2011.

[11] L. Rossi, S. Sacanna, W. T. Irvine, P. M. Chaikin, D. J. Pine, and A. P. Philipse,

"Cubic crystals from cubic colloids," *Soft Matter*, vol. 7, no. 9, p. 4139–4142, 2011.

[12] M. R. Jones, R. J. Macfarlane, B. Lee, J. Zhang, K. L. Young, A. J. Senesi, and C. A. Mirkin, "Dna-nanoparticle superlattices formed from anisotropic building blocks," *Nature Materials*, vol. 9, no. 11, p. 913–917, 2010.

[13] M. R. Jones, R. J. Macfarlane, A. E. Prigodich, P. C. Patel, and C. A. Mirkin, "Nanoparticle shape anisotropy dictates the collective behavior of surface-bound ligands," *Journal of the American Chemical Society*, vol. 133, no. 46, p. 18865–18869, 2011.

[14] Y. S. Lee, *Self-assembly and nanotechnology: A force balance approach*. John Wiley & Sons, 2008.

[15] G. M. Whitesides and B. Grzybowski, "Self-assembly at all scales," *Science*, vol. 295, no. 5564, pp. 2418–2421, 2002.

[16] *Surfactant aggregation*. Springer Science+Business Media, LLC, 1992.

[17] P. Alexandridis, *Amphiphilic block copolymers self-assembly and applications*. Elsevier, 2000.

[18] R. Sui, P. A. Charpentier, and R. A. Marriott, "Metal oxide-related dendritic structures: Self-assembly and applications for sensor, catalysis, energy conversion and beyond," *Nanomaterials*, vol. 11, no. 7, 2021.

[19] J. H. Fendler, *Nanoparticles in solids and solutions*. Kluwer Academic Publishers, 1996.

[20] D. T. Bong, T. D. Clark, J. R. Granja, and M. R. Ghadiri, "Self-assembling organic nanotubes," *Angewandte Chemie International Edition*, vol. 40, no. 6, pp. 988–1011, 2001.

[21] R. W. Kelsall, I. W. Hamley, and M. Geoghegan, *Nanoscale science and technology*. John Wiley &; Sons, 2005.

[22] Y. Dahman, *Nanotechnology and functional materials for engineers*. Elsevier, 2017.

[23] M. Grzelczak, J. Vermant, E. M. Furst, and L. M. Liz-Marzán, "Directed self-assembly of nanoparticles," *ACS Nano*, vol. 4, no. 7, pp. 3591–3605, 2010. PMID: 20568710.

[24] Z. Nie, A. Petukhova, and E. Kumacheva, "Properties and emerging applications of self-assembled structures made from inorganic nanoparticles," *Nature Nanotechnology*, vol. 5, no. 1, p. 15–25, 2009.

[25] M. A. Stuart, W. T. Huck, J. Genzer, M. Müller, C. Ober, M. Stamm, G. B. Sukhorukov, I. Szleifer, V. V. Tsukruk, M. Urban, and et al., "Emerging applications of stimuli-responsive polymer materials," *Nature Materials*, vol. 9, no. 2, p. 101–113, 2010.

[26] B. Rybtchinski, "Adaptive supramolecular nanomaterials based on strong noncovalent interactions," *ACS Nano*, vol. 5, no. 9, pp. 6791–6818, 2011. PMID: 21870803.

[27] M. Motornov, S. Minko, K.-J. Eichhorn, M. Nitschke, F. Simon, and M. Stamm, "Reversible tuning of wetting behavior of polymer surface with responsive polymer brushes," *Langmuir*, vol. 19, no. 19, pp. 8077–8085, 2003.

[28] S. J. Jhaveri, M. R. Hynd, N. Dowell-Mesfin, J. N. Turner, W. Shain, and C. K. Ober, "Release of nerve growth factor from hema hydrogel-coated substrates and its effect on the differentiation of neural cells," *Biomacromolecules*, vol. 10, no. 1, pp. 174–183, 2009. PMID: 19061335.

[29] C. L. Bayer and N. A. Peppas, "Advances in recognitive, conductive and responsive delivery systems," *Journal of Controlled Release*, vol. 132, no. 3, pp. 216–221, 2008. Proceedings of the Tenth European Symposium on Controlled Drug Delivery.

[30] A. S. Hoffman, "The origins and evolution of "controlled" drug delivery systems," *Journal of Controlled Release*, vol. 132, no. 3, pp. 153–163, 2008. Proceedings of the Tenth European Symposium on Controlled Drug Delivery.

[31] Z. Liu and P. Calvert, "Multilayer hydrogels as muscle-like actuators," *Advanced Materials*, vol. 12, no. 4, pp. 288–291, 2000.

[32] P. M. Mendes, "Stimuli-responsive surfaces for bio-applications," *Chemical Society Reviews*, vol. 37, p. 2512, Sep 2008.

[33] I. Luzinov, S. Minko, and V. V. Tsukruk, "Responsive brush layers: From tailored gradients to reversibly assembled nanoparticles," *Soft Matter*, vol. 4, p. 714, Feb 2008.

[34] E. L. Thomas, D. M. Anderson, C. S. Henkee, and D. Hoffman, "Periodic area-minimizing surfaces in block copolymers," *Nature*, vol. 334, no. 6183, p. 598–601, 1988.

[35] F. S. Bates, "Polymer-polymer phase behavior," *Science*, vol. 251, no. 4996, pp. 898–905, 1991.

[36] F. S. Bates and G. H. Fredrickson, "Block copolymers—designer soft materials," *Physics Today*, vol. 52, no. 2, pp. 32–38, 1999.

[37] G. Riess, "Micellization of block copolymers," *Progress in Polymer Science*, vol. 28, no. 7, pp. 1107–1170, 2003.

[38] E. Avalos, T. Higuchi, T. Teramoto, H. Yabu, and Y. Nishiura, "Frustrated phases under three-dimensional confinement simulated by a set of coupled Cahn–Hilliard equations," *Soft Matter*, vol. 12, no. 27, p. 5905–5914, 2016.

[39] E. Avalos, T. Teramoto, H. Komiyama, H. Yabu, and Y. Nishiura, "Transformation of block copolymer nanoparticles from ellipsoids with striped lamellae into onionlike spheres and dynamical control via coupled Cahn–Hilliard equations," *ACS Omega*, vol. 3, no. 1, p. 1304–1314, 2018.

[40] C. Miehe, S. Mauthe, and H. Ulmer, "Formulation and numerical exploitation of mixed variational principles for coupled problems of Cahn–Hilliard-type and standard diffusion in elastic solids," *International Journal for Numerical Methods in Engineering*, vol. 99, no. 10, pp. 737–762, 2014.

[41] L. Anand, "A Cahn–Hilliard-type theory for species diffusion coupled with large elastic–plastic deformations," *Journal of the Mechanics and Physics of Solids*, vol. 60, no. 12, pp. 1983–2002, 2012.

[42] A. Logg, K.-A. Mardal, G. N. Wells, *et al.*, *Automated Solution of Differential Equations by the Finite Element Method*. Springer, 2012.

[43] M. Schumann and W. Robinson, *A book about colab: (and related activities)*. Printed Matter, 2015.

[44] U. Ayachit, *The ParaView Guide: A Parallel Visualization Application*. Clifton Park, NY, USA: Kitware, Inc., 2015.

[45] J. W. Cahn and J. E. Hilliard, "Free energy of a nonuniform system. i. interfacial free energy," *The Journal of Chemical Physics*, vol. 28, no. 2, p. 258–267, 1958.

[46] J. W. Cahn, "Free energy of a nonuniform system. ii. thermodynamic basis," *The Journal of Chemical Physics*, vol. 30, no. 5, p. 1121–1124, 1959.

[47] J. W. Cahn and J. E. Hilliard, "Free energy of a nonuniform system. iii. nucleation in a two-component incompressible fluid," *The Journal of Chemical Physics*, vol. 31, no. 3, p. 688–699, 1959.

[48] J. W. Cahn, "On spinodal decomposition," *Acta Metallurgica*, vol. 9, no. 9, pp. 795–801, 1961.

[49] D. Hershey, *Transport analysis*. New York, 1974.

[50] E. Nagy, *Basic equations of the mass transport through a membrane layer*, p. 35–36. Elsevier, 2012.

[51] C. M. Elliott, D. A. French, and F. A. Milner, "A second order splitting method for the cahn-hilliard equation," *Numerische Mathematik*, vol. 54, no. 5, p. 575–590, 1989.

[52] M. Martini and G. E. Sodini, "Numerical methods for a system of coupled cahn-hilliard equations," *Communications in Applied and Industrial Mathematics*, vol. 12, no. 1, p. 1–12, 2021.

[53] D. J. Eyre, "An unconditionally stable one-step scheme for gradient systems," 1997.

[54] F. Guillén-González and G. Tierra, "On linear schemes for a cahn–hilliard diffuse interface model," *Journal of Computational Physics*, vol. 234, pp. 140–171, 2013.

[55] X. Wu, G. J. van Zwieten, and K. G. van der Zee, "Stabilized second-order convex splitting schemes for cahn–hilliard models with application to diffuse-interface tumor-growth models," *International Journal for Numerical Methods in Biomedical Engineering*, vol. 30, no. 2, pp. 180–203, 2014.

[56] o. Sansone, n. H. Diamond, and n. Hille, *Orthogonal functions*. Dover, 1991.

[57] S. Hussain, A. Shah, S. Ayub, and A. Ullah, "An approximate analytical solution of the allen-cahn equation using homotopy perturbation method and homotopy analysis method," *Heliyon*, vol. 5, no. 12, p. e03060, 2019.

[58] A. Giorgini, M. Grasselli, and A. Miranville, "The cahn–hilliard–oono equation with singular potential," *Mathematical Models and Methods in Applied Sciences*, vol. 27, no. 13, p. 2485–2510, 2017.

[59] K. Cheng, C. Wang, and S. M. Wise, "A weakly nonlinear, energy stable scheme for the strongly anisotropic cahn-hilliard equation and its convergence analysis," *Journal of Computational Physics*, vol. 405, p. 109109, 2020.

[60] X. Zhao and N. Duan, "A class of sixth order viscous cahn-hilliard equation with willmore regularization in r3," *Mathematics*, vol. 8, no. 11, p. 1865, 2020.

[61] F. Rathgeber, D. A. Ham, L. Mitchell, M. Lange, F. Luporini, A. T. Mcrae, G.-T. Bercea, G. R. Markall, and P. H. Kelly, "Firedrake," *ACM Transactions on Mathematical Software*, vol. 43, no. 3, p. 1–27, 2017.

[62] R. C. Kirby and L. Mitchell, "Code generation for generally mapped finite elements," *ACM Transactions on Mathematical Software*, vol. 45, no. 4, p. 1–23, 2019.

[63] J. T. Lee, C. Jo, and M. De Volder, "Bicontinuous phase separation of lithium-ion battery electrodes for ultrahigh areal loading," *Proceedings of the National Academy of Sciences*, vol. 117, no. 35, pp. 21155–21161, 2020.

[64] S. Prussin, "Generation and distribution of dislocations by solute diffusion," *Journal of Applied Physics*, vol. 32, p. 1876–1881, Mar 1961.

[65] F. C. LarchÉ and J. W. Cahn, *The Interactions of Composition and Stress in*

Crystalline Solids, pp. 120–146. Berlin, Heidelberg: Springer Berlin Heidelberg, 1999.

[66] F. Yang, "Interaction between diffusion and chemical stresses," *Materials Science and Engineering: A*, vol. 409, no. 1, pp. 153–159, 2005. Micromechanics of Advanced Materials II.

[67] R. W. Ogden, *Elasticity*, p. 222–224. Dover Publications, 1997.

[68] A. Pressley, *Elementary differential geometry*. Springer, 2010.

[69] J. C. Simo and H. T. J. R., *Computational inelasticity*. Springer, 1998.